DEFECTS IN SILICON–GERMANIUM STRAINED EPITAXIAL LAYERS

By

MARK DYNNA

A Thesis

Submitted to the School of Graduate Studies

in Partial Fulfillment of the Requirements

for the Degree

Doctor of Philosophy

McMaster University

DEFECTS IN SILICON–GERMANIUM STRAINED EPITAXIAL LAYERS

DOCTOR OF PHILOSOPHY (1993) McMASTER UNIVERSITY
(Materials Science and Engineering) Hamilton, Ontario

TITLE: Defects in Silicon–Germanium Strained Epitaxial Layers

AUTHOR: Mark Dynna, B.A.Sc. (University of Toronto)
M.A.Sc. (University of Toronto)

SUPERVISOR: Professor G.C. Weatherly

NUMBER OF PAGES: xiii, 168

Abstract

The energies of one and two–dimensional dislocation arrays lying near a free surface are evaluated directly from the stress fields of single dislocations in a half–space. These results are used to obtain expressions giving the equilibrium spacings of a number of different arrays relieving misfit in a strained epitaxial system. Numerical calculations are performed for the case of edge and 60° dislocations relieving strain in a silicon–germanium layer deposited on a silicon substrate. This method is also used to calculate the energies of various low angle grain boundaries in a half–space.

Single–ended dislocation sources are observed using transmission electron microscopy in two short–period Si–Ge superlattices grown on Si(100). Their formation is linked to the development of non–planar layers during the growth of the superlattices. The relaxation of these superlattices takes place at significantly lower temperatures than equivalently strained homogeneous epilayers.

Si–Ge short period superlattices deposited on Si(100) are shown to relax through twinning on {111} planes if the deposited layers become grossly non–planar. Twinning is accompanied by the formation of a diamond hexagonal phase. No 60° $\frac{a}{2}\langle 110\rangle$ dislocations relieving misfit are present in the

strained layer structure.

The nature and origin of a new type of defect in $Si_{1-x}Ge_x/Si$ strained layer structures, the "pagoda" defect, is studied using transmission electron microscopy. The defects are found to propagate in a direction determined by the position of the Si source in unrotated substrates, and to have their origin in the role played by SiC particles (left after cleaning the substrate) during the growth process. Pits that form at the SiC particles are preserved during MBE growth and perturb the strained layers, leading to the formation of pagodas.

Acknowledgements

The author would like to express thanks to his supervisor, Dr. G.C. Weatherly, for his support and encouragement throughout this work.

Thanks are also due to Dr. Z.S. Basinski for helpful discussions.

The author would also like to thank Dr. D.C. Houghton and Dr. T.E. Jackman for providing the material used in this study, John McCaffrey for preparing some of the TEM specimens, and Heather Halabourda for assistance with the word processing.

The financial support of the Ontario Government and McMaster University is gratefully acknowledged.

Table of Contents

List of Tables

List of Figures

CHAPTER 1

Introduction

Silicon–germanium heteroepitaxy is a subject of current interest – the growth of strained layer structures in this lattice–mismatched system by techniques such as molecular beam epitaxy or chemical vapour deposition is believed to hold considerable technological promise. Strain–induced modifications of the bandgap make possible the design of electronic and optoelectronic devices which are unobtainable using unstrained silicon. An important example of an electronic device making use of Si–Ge strained layers is the Si–Ge/Si heterojunction bipolar transistor (Patten *et al.* 1990). Optoelectronic devices include the p–i–n diode (Lang *et al.* 1985) and the $Si_{1-x}Ge_x/Si$ digital optoelectronic switch (Kovacic *et al.* 1991). However, the effective manufacture of such devices requires that the strained layers be essentially free of defects such as dislocations, stacking faults, and twins, and therefore an understanding of the relationship between defect formation and the geometrical structure of the device, the conditions under which it is grown, and its subsequent processing treatments is crucial.

This thesis examines the formation of defects in various Si–Ge strained layer structures deposited on Si(100). Homogeneous epilayers, $Si_{1-x}Ge_x/Si$ superlattices and short–period $(Si_mGe_n)_p$ superlattices grown by

molecular beam epitaxy at the National Research Council in Ottawa were studied using transmission electron microscopy. A variety of defects were found in the as–grown material, including dislocation sources, twins, second phases, and the "pagoda defect". Interfacial perturbations play an important role in generating all of these defects. The evolution of the defect structure on annealing at higher temperatures was examined in as–grown samples containing twins and dislocation sources. Experimental results are discussed in chapters 5, 6, and 7.

In addition to the experimental work, there is a section of theory (chapter 3) concerning the energetics of dislocation arrays in strained epitaxial layers. This is applied to the problem of the critical thickness (the thickness at which it becomes energetically favourable to introduce a dislocation or array of dislocations to the strained layer) and equilibrium dislocation spacing in Si–Ge strained layers deposited on Si(100). It is also shown that the method used in these calculations may easily be adapted to give the energies of various low angle grain boundaries near a free surface, and, as a limiting case, corresponding energies in an infinite crystal.

CHAPTER 2

Review

2.1. The Growth of Heteroepitaxial Films

2.1.1. Systems in which there is Perfect Lattice Matching

A) Initial Stages of Film Deposition

Consider the deposition under near–equilibrium conditions of a thin film of a single atomic species on a substrate. The surface energies which are important in this process are those of the substrate, γ_s, the film, γ_f, (assumed here to be isotropic), and the interface, γ_{in}, where $\gamma_{in} = \gamma_s + \gamma_f - \beta$ and β is the adhesion energy between the substrate and the film. The supersaturation of the system is defined by $\Delta\mu = \mu - \mu_0$, where μ_0 is the chemical potential of the solid film at the growth temperature and pressure, and μ is the chemical potential of the material in the vapour phase. When a volume V_f of the film is deposited on the substrate, the change in the free energy of the system is

$$\Delta G = -\Delta\mu V_f + \gamma_f A_f + \gamma_{in} A_{in} - \gamma_s A_{in}, \qquad (2.1.1)$$

where A_f and A_{in} are the surface area of the film and the area of the interface. There are two possibilities. If the film does not completely wet the substrate, it condenses on the substrate in the shape of a spherical cap with a wetting angle θ given by the following balance of interfacial tensions:

$$\gamma_s = \gamma_{in} + \gamma_f \cos\theta, \tag{2.1.2}$$

so that

$$\cos\theta = \frac{\gamma_s - \gamma_{in}}{\gamma_f}; \quad \cos\theta < 1. \tag{2.1.3}$$

Thus partial wetting occurs when

$$\gamma_s - \gamma_{in} < \gamma_f,$$

that is,

$$\gamma_f + \gamma_{in} - \gamma_s > 0 \tag{2.1.4}$$

or

$$\beta < 2\gamma_f. \tag{2.1.5}$$

Then

$$\Delta G(r) = \{-\tfrac{4}{3}\pi r^3\Delta\mu + 4\pi r^2\gamma_f\}\{(2 + \cos\theta)(1 - \cos\theta)^2/4\}, \qquad (2.1.6)$$

where r is the radius of the truncated sphere. In this case $\Delta\mu$ must be greater than zero in order for the film to grow, and there is an energy barrier which must be overcome before stable nuclei can be formed. The activation energy is

$$\Delta G^* = \frac{16\pi\gamma_f}{3\Delta\mu^2}(2 + \cos\theta)(1 - \cos\theta)^2/4, \qquad (2.1.7)$$

and there is a critical nucleus radius of

$$r^* = \frac{2\gamma_f}{\Delta\mu}. \qquad (2.1.8)$$

Since three–dimensional nuclei are required in order for the film to form, growth proceeds via the formation of islands. This mechanism is known as the Volmer–Weber growth mode (Volmer and Weber 1926). The extent of surface roughness may be minimized by letting $\Delta\mu$ become large so that the height of the islands is reduced and that many nuclei quickly merge together (Bauer and van der Merwe 1986).

If $\beta > 2\gamma_f$, then the film completely wets the substrate, and, ignoring the presence of film ledges,

$$\begin{aligned}\Delta G &= -\Delta\mu V_f + \gamma_f A_f + (\gamma_s + \gamma_f - \beta - \gamma_s)A_f \\ &= -\Delta\mu V_f + (2\gamma_f - \beta)A_f. \end{aligned} \qquad (2.1.9)$$

There is no activation energy barrier which must be overcome in depositing the film, and growth may take place even at undersaturation ($\Delta\mu < 0$). The film goes down as a flat two–dimensional deposit. This sort of growth, which occurs when

$$\gamma_f + \gamma_{in} - \gamma_s < 0 \qquad (2.1.10)$$

is known as the Frank–van der Merwe mode. It is the preferred condition for heteroepitaxial growth. The two inequalities (2.1.4) and (2.1.10) are together known as the Bauer criteria (Bauer 1958), and predict the growth mode of lattice–matched systems in near–equilibrium conditions.

The conditions under which 2D growth is possible may also be expressed in terms of relative bond energies. Letting ϕ_{ff}, ϕ_{ss}, and ϕ_{sf} be the bond energies between atoms in the film, atoms in the substrate, and atoms in the film with atoms in the substrate, respectively, and considering only nearest neighbour interactions gives $\gamma_f = \frac{1}{2}C\phi_{ff}$, $\gamma_s = \frac{1}{2}C\phi_{ss}$, and $\beta = C\phi_{sf}$, where C is a constant. When $\phi_{sf} > \phi_{ff}$, $\beta > 2\gamma_f$, and two–dimensional growth is possible, while if $\phi_{ff} > \phi_{sf}$, island growth takes place.

B) Later Stages of Film Growth

Once the substrate has been completely covered by the film, it is of course no longer necessary to wet the substrate. In addition, the interaction between the deposited atoms and the substrate decreases. In the case of a

film which completely wets the substrate, the change in the free energy of the system on the deposition of the n^{th} monolayer is

$$\Delta G = -\Delta\mu V_f - \beta_n A_f, \qquad (2.1.11)$$

where β_n represents the interaction of the n^{th} monolayer with the substrate. Growth may proceed at appreciable undersaturations for several monolayers, after which the process becomes essentially one of homoepitaxy. In the case of a film which partially wets the substrate, the forces which initially caused the formation of islands are no longer present. In fact, it becomes energetically favourable for the surface to smooth itself. The extent to which this is possible depends on the kinetics of the process.

C) The Growth of Superlattices

If, in a system with perfect lattice matching, a superlattice is to be formed, the alternate deposition of at least two species of atoms is required. When the growth of F on S is followed by the growth of S on F it is impossible to achieve a true state of continuous two–dimensional growth, for if $\gamma_f + \gamma_{in} - \gamma_s < 0$ and F grows smoothly on S, which has a higher surface energy, then $\gamma_s + \gamma_{in} - \gamma_f > 0$ and the growth of S on F proceeds via island formation. If γ_s and γ_f differ strongly then it is impossible to prevent the formation of a very rough layer of S, but if $\gamma_s \cong \gamma_f$ and γ_{in} is small, then the condition of two–dimensional growth may be approached (Bauer and van der Merwe 1986).

2.1.2. Systems in which there is Uniform Lattice Mismatch

A) Initial Stages of Film Deposition

When the material being deposited under near–equilibrium conditions has a different lattice parameter than the substrate, it is placed in a state of strain when it condenses on the substrate. The change in the free energy of the system on the deposition of a volume V_f on the substrate is

$$\begin{aligned}\Delta G &= -\Delta\mu V_f + \gamma_f A_f + \gamma_{in} A_{in} - \gamma_s A_{in} + \tfrac{1}{2}\int_{V_f} \sigma_{ij}\epsilon_{ij} dV_f \\ &= -\Delta\mu V_f + \gamma_f V_f + (\gamma_f - \beta)A_{in} + \tfrac{1}{2}\int_{V_f} \sigma_{ij}\epsilon_{ij} dV_f, \qquad (2.1.12)\end{aligned}$$

where

$$\tfrac{1}{2}\int_{V_f} \sigma_{ij}\epsilon_{ij} dV_f$$

accounts for the elastic strain in the film.

If $\beta < 2\gamma_f$, growth will proceed at once through the formation of islands, as in the case of unstrained systems. However, the degree of surface roughness will be augmented as the system moves to lower its elastic strain energy. Two–dimensional growth under these conditions is impossible. If $\beta > 2\gamma_f$, there is a basic tendency for the film to wet the substrate. For a deposited layer which remains flat, the change in the free energy of the

system (ignoring the presence of film ledges) is given by

$$\Delta G = -\Delta\mu V_f + (2\gamma_f - \beta)A_f + \frac{Ef^2hA_f}{(1-\nu)}, \qquad (2.1.13)$$

where h is the height of the monolayer and f is the lattice mismatch strain. However, some of the strain energy of the system may be relieved through the development of perturbations in the growth surface of the film. If the energy relieved is greater than the increase in the total surface energy of the film and the energy required to move material further away from the substrate, then the basic morphology of the film is no longer two–dimensional. Growth takes place at once in the Volmer–Weber mode, although for different reasons than in the case of unstrained systems. In general this will happen when γ_f and β are small and ϵ is large, although the precise details (even in the case of an isotropic film surface energy) are very difficult to work out because of the complexity of the elasticity problem.

B) Later Stages of Film Growth

After the substrate has been completely covered by the growing film, the further development of the surface morphology of the film is determined by the decreasing interaction of the deposited atoms with the substrate and the driving force for elastic relaxation. In the case of a film which initially only partially wets the substrate, the strain inherent in the system prevents the formation of a smooth interface. In the case of a film which has $\beta > 2\gamma_f$ but immediately develops a rough surface because of elastic strain, the

roughness of the surface will tend to increase as the interaction of the deposited atoms with the substrate provides less of a counterbalance to elastic relaxation. If the film initially forms a smooth deposit on the substrate, a transition to island growth will take place when the interaction of the deposited material with the substrate falls below a critical value. This type of growth is known as the Stranski–Krastonov mode (Stranski and Krastonov 1938), and is the characteristic mode of growth in many lattice mismatched systems.

2.1.3. Si–Ge/Si(100) Heteroepitaxy

A) The Growth of Si on Si(100)

It has been established that the Si(100) surface takes on a 2×1 reconstruction in which pairs of surface atoms, each atom having two dangling bonds, form dimers in order to lower their energy. Surface atoms are shifted from bulk lattice positions over a distance of approximately 0.45 Å in the direction of the surface dimer (Tromp, Smeenk, and Saris 1981). This deviation from bulk lattice positions drops off rapidly on moving into the solid – the displacement of atoms in the layer next to the surface is less than 0.2 Å. There is also a slight inward relaxation of the surface of 0.08 ± 0.03 Å. As a result of reconstruction, the surface crystallography of Si(100) has a two–fold rather than a four–fold rotational symmetry element. Pairs of atoms (dimers) are lined up in rows as shown schematically in fig. 2.1. In general a physical surface is broken into domains, each of which has one of the two possible orientations of dimer rows. Domain boundaries

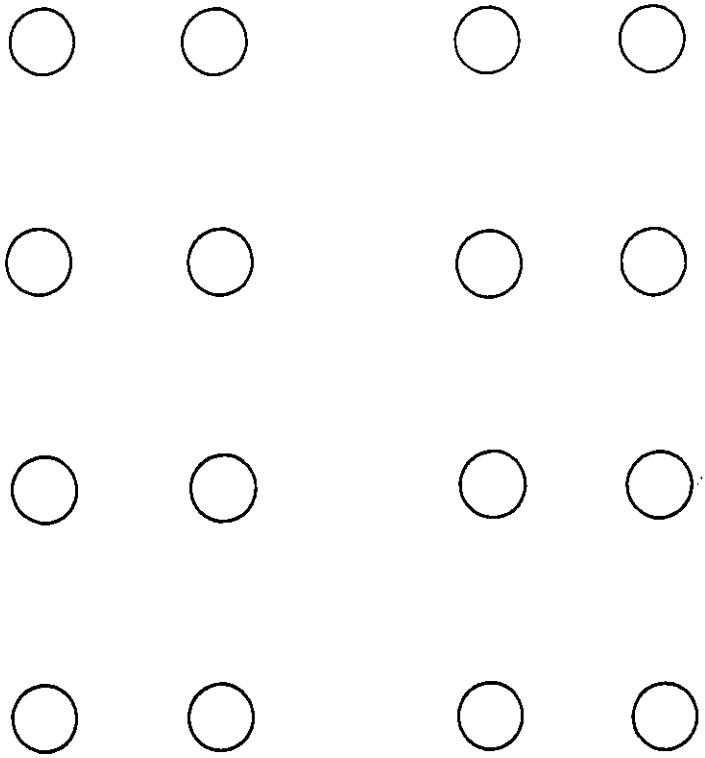

Figure 2.1: Schematic representation of the reconstructed Si(100) surface.

separate regions having orthogonal dimer rows. These features are important in the epitaxy of Si on Si(100). Mo *et al.* (1989) have shown that at temperatures between 300 and 500 K, the lateral accommodation of Si adatoms is orders of magnitude greater at the ends of the dimer rows than at the sides. Monatomic terrace steps which correspond to the ends of dimer rows are good sinks for adatoms, while terrace steps which correspond to the sides of dimer rows are poor sinks. The net result is that the shape of deposited islands of Si is anisotropic.

B) The Growth of Single Layers of Ge on Si(100)

The growth of pure Ge on Si(100) involves a 4% lattice mismatch, and therefore two–dimensional growth places the germanium in a highly strained state. As discussed in the previous section, equilibrium interfacial thermodynamics indicates that there will be a tendency toward island formation once the deposit becomes sufficiently thick. It has been found that for pure Ge deposited on Si(100), a transition from two–dimensional growth to island formation takes place when the film is 3–4 monolayers thick (Mo *et al.* 1990; Williams *et al.* 1991). Scanning tunneling microscopy (Mo *et al.* 1991) has shown that at submonolayer coverages, terrace steps which correspond to the ends of dimer rows are good sinks for Ge adatoms, while terrace steps which correspond to the sides of dimer rows are poor sinks. Furthermore, the surface diffusion of Ge on Si(100) is 1,000 times faster along substrate dimer rows than perpendicular to them. Scanning tunneling microscopy has also shown that the transition from two–dimensional to island growth at 775 K follows a kinetic pathway which involves the formation of a

nonequilibrium "intermediate phase". Rather than immediately forming large clusters of Ge atoms 250 Å high bounded by {113} planes (the final equilibrium state), deposited Ge first forms small clusters 20–50 Å high and 1000 Å long bounded by {105} planes. These are more easily nucleated at this temperature and serve as a starting point for the formation of the large clusters. However, growth at 850 K results in the formation of large clusters only. Thus the details of the transition from two–dimensional to three–dimensional growth are more complicated than those given by a simple equilibrium treatment.

It is possible, through the use of surfactants, to modify the thickness at which the onset of islanding takes place. Surfactants effectively modify the parameter β_n, which is a measure of the attraction between the n^{th} layer of deposited atoms and the substrate. LeGoues, Copel, and Tromp (1990) have used the preliminary deposition of a monolayer of arsenic on the substrate surface in order to increase β_n and therefore the thickness at which islanding begins to occur. It was found that the transition to island growth took place after the deposition of 10 monolayers of Ge rather than 3 monolayers in the case of unmodified surfaces.

C) The Growth of Si–Ge Superlattices on Si(100)

Short period superlattices having a structure $(Si_mGe_n)_p$, where m and n denote the number of monolayers of silicon and germanium in a single period of the superlattice and p denotes the number of periods have been grown by molecular beam epitaxy on Si(100) and studied by

Baribeau *et al.* (1991). Their structural properties were examined by Raman scattering spectroscopy, glancing incidence X–ray reflection, Rutherford backscattering, and extended X–ray absorption fine structure analysis. It was found the Ge_n films with $n \leq 5$ were two–dimensional in nature and showed no sign of strain relaxation. However, some interfacial mixing of Si and Ge atoms was present in these films. The character of superlattices with thicker Ge layers was markedly different – Ge clustering and strain relaxation were observed when $n = 12$. In general the results appear to indicate that Ge layer thicknesses may be greater in superlattices than in single Ge layers before there is a transition to three–dimensional growth.

2.2. Dislocations in Strained Layers

2.2.1. Energetics

A) Epilayer Self Energy

If a block of material M unit cells long having a lattice parameter a_0 and height h is biaxially strained and joined to a second block of material M units cells long having a lattice parameter a_1 and height Nh as in fig. 2.2, the resulting composite system is in a state of self–stress. A partition of strain between the two blocks will take place in such a way that the elastic energy of the system is minimized. If any buckling of the two blocks is ignored (buckling is negligible when $N>>1$), then except for regions close to

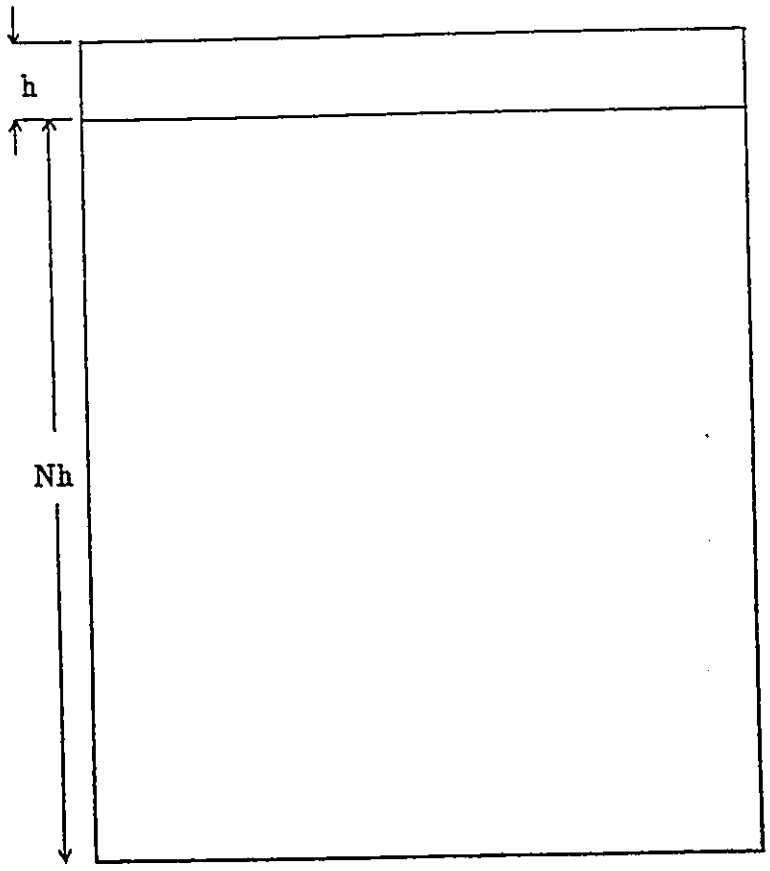

Figure 2.2: Internally stressed system formed by joining two materials having different lattice parameters.

the edges, each block is in a state of biaxial strain. For biaxial strain, Hooke's law gives

$$e = \frac{1}{E}(\sigma - \nu\sigma), \tag{2.2.1}$$

where e is the magnitude of the biaxial strain, σ is the magnitude of the biaxial stress, E is Young's modulus, and ν is Poisson's ratio. Since $E = 2\mu(1 + \nu)$, where μ is the shear modulus,

$$\sigma = \frac{2\mu(1 + \nu)e}{(1 - \nu)} . \tag{2.2.2}$$

The relative displacement of the two blocks is $u = M(a_1 - a_0)$; the total integrated strain in the system must be equal to this displacement. The magnitude of the strain in the material having the lattice parameter a_1 is given by $\epsilon = \frac{a_1' - a_1}{a_1} \cong \frac{a_1' - a_1}{a_0}$. Therefore the elastic energy per unit area of the system is

$$E_{el} = \frac{2\mu(1 + \nu)(f - \epsilon)^2 h}{(1 - \nu)} + \frac{2\mu(1 + \nu)\epsilon^2 Nh}{(1 - \nu)} , \tag{2.2.3}$$

where $f = \frac{a_1 - a_0}{a_0}$. Equating the partial derivative of E_{el} with respect to ϵ with zero gives a minimum in the energy at

$$\epsilon = \frac{f}{N + 1} . \tag{2.2.4}$$

In the limit $N \to \infty$, $\epsilon = 0$, and all of the strain is confined to a finite layer sitting on a semi–infinite base.

It is essentially this condition which describes strained epitaxial layers deposited on a substrate of much greater thickness. Except for a small relaxed region near the edge of the sample, the epitaxial layer is in a state of biaxial strain, while the substrate is strain–free. The strained layer has an energy per unit area of

$$E_{epi} = \frac{2\mu(1 + \nu)f^2 h}{(1 - \nu)} , \qquad (2.2.5)$$

where h is the height of the epilayer and $f = \frac{a_{sub} - a_{epi}}{a_{epi}}$, with a_{epi} and a_{sub} being the lattice parameters of the epilayer and substrate respectively.

Silicon–germanium alloys form a continuous solid solution, and obey Vegard's law (Dismukes, Ekstrom, and Paff 1964). If they are deposited on a silicon substrate, they are placed in a state of biaxial compression. The lattice parameter of silicon at 25°C is $a_{Si} = 5.4309$ Å, while that of germanium is $a_{Ge} = 5.6577$ Å at 25°C (Pearson 1967). Then $f(x) = 0.040x$, where x is the fraction of Ge in the alloy. Taking $\mu = 68.1$ GPa and $\nu = 0.218$ for Si (Hirth and Lothe 1982) gives

$$E_{epi} = (3.39 \times 10^8)x^2 h, \qquad (2.2.6)$$

where h is in meters and E_{epi} is in J/m^2.

B) Dislocation Self Energy

A common approximation (Houghton *et al.* 1990) used to represent the energy of a dislocation in a half–space is

$$U_{disl} = \frac{\mu b^2(1 - \nu\cos^2\beta)}{4\pi(1 - \nu)}\ln(\frac{\alpha h}{b}), \qquad (2.2.7)$$

where U_{disl} is the energy per unit length of the dislocation, β is the angle that the Burgers vector makes with the dislocation, h is the distance from the dislocation to the free surface, and α is the core parameter of the dislocation. The energy is taken to arise from a strained cylinder of radius h centered about the dislocation core. In work relating to Si–Ge strained layer structures, α is often taken to be equal to 4 (Houghton *et al.* 1990).

An exact expression for the energy of a dislocation near a free surface has recently been obtained (Freund 1990). In the notation used in this thesis,

$$U_{disl} = \frac{\mu b^2}{4\pi(1 - \nu)}[(1 - \nu\cos^2\beta)\ln(\frac{2h}{r_0})$$

$$- \sin^2\beta(\tfrac{1}{2}\cos(\pi - 2\varphi) + \frac{1 - 2\nu}{4(1 - \nu)})], \qquad (2.2.8)$$

where φ is the angle between the slip plane of the dislocation and the free surface. The work done by the tractions on the surface of the core as the dislocation is formed is accounted for by the term $\frac{\mu b^2 \sin^2\beta(1-2\nu)}{16\pi(1-\nu)^2}$; the other terms are due to the work done by the tractions on the sides of a vertical

cut used to form the dislocation. In this analysis the core radius is assumed to be vanishingly small, and contributions to the dislocation energy from the non–linear elastic material which forms the core are ignored.

The core structures and energies of various types of dislocations in Si, Ge, and diamond have been evaluated (Nandedkar and Narayan 1990) using various interatomic potentials. In the case of Si, the core energy of a 60° dislocation with a Burgers vector of the type $\frac{a}{2}\langle 110\rangle$ as calculated using the Stillinger–Weber potential is 0.95 eV $Å^{-1}$, while a 90° dislocation having the same type of Burgers vector has a core energy of 0.49 eV $Å^{-1}$. In both cases the core cut–off radius was determined to be approximately 5 Å. The difference between the two energies is primarily due to the fact that the 60° dislocation has a dangling bond in its core structure, while the core of the 90° dislocation is free of dangling bonds. These core energies and cut–off radii may be used in conjunction with equation (2.2.8) in order to arrive at the self energy of a dislocation in a half–space (neglecting the energy of any surface step associated with the dislocation). It is then possible to determine the value of the core parameter α by writing the expression for the energy of a dislocation near a free surface in the form of equation (2.2.7). This value has been the subject of some debate, with estimates for a 60° $\frac{a}{2}\langle 110\rangle$ dislocation ranging from 0.6 (Perovic and Houghton 1992) to 2.0 (Hull and Bean 1989) to 4.0 (Houghton *et al.* 1990). In this thesis, the value of the core parameter is determined using an expression for the self energy of a dislocation in a half–space which ignores the work done by the core tractions as the dislocation is formed. The result is compared with that obtained when core tractions are taken into account.

C) The Critical Thickness and Dislocation Energetics

Once a strained epitaxial layer becomes sufficiently thick, there is a tendency for the relief of biaxial strain to occur via the introduction of misfit dislocations to the substrate/epilayer interface. The thickness at which it becomes energetically favourable for this to happen is known as the critical thickness; when the epilayer is less than this thickness it resists the introduction of misfit dislocations. A number of theories of the critical thickness and the energetics of dislocation arrays in strained layers have been put forward; these are reviewed in what follows.

i) The Theory of Matthews and Blakeslee

Matthews and Blakeslee (1974) developed an expression for the critical thickness by analyzing the behaviour of a single dislocation in a strained epilayer. Their argument runs as follows: the force due to the internal stress in an unrelaxed epilayer on a dislocation running from the substrate/epilayer interface to the free surface is $\sigma\cos\varphi\cos\lambda\frac{h}{\sin\varphi}$, where σ is the magnitude of the biaxial stress (this is equivalent to the sum of a uniaxial stress and a hydrostatic stress), φ is the angle between the slip plane normal and the normal to the free surface, and λ is the angle between the Burgers vector of the dislocation and the normal to the free surface. This force is opposed by the line tension of the dislocation. The net force acting on the dislocation is given by

$$F = \tau_{eff} b \frac{h}{\sin\varphi} = \frac{\sigma\cos\varphi\cos\lambda bh}{\sin\varphi}$$

$$- \frac{\mu b^2}{4\pi(1-\nu)}(1 - \nu\cos^2\beta)\ln(\frac{\alpha h}{b}), \qquad (2.2.9)$$

so that the effective resolved shear stress acting on the dislocation is

$$\tau_{eff} = \frac{2\mu(1+\nu)f\cos\varphi\cos\lambda}{(1-\nu)}$$

$$- \frac{\mu b\sin\varphi}{4\pi h(1-\nu)}(1 - \nu\cos^2\beta)\ln(\frac{\alpha h}{b}). \qquad (2.2.10)$$

The critical thickness h_c corresponds to $\tau_{eff} = 0$:

$$h_c = \frac{b\sin\varphi}{8\pi(1+\nu)f\cos\varphi\cos\lambda}(1 - \nu\cos^2\beta)\ln(\frac{\alpha h_c}{b}). \qquad (2.2.11)$$

ii) Matthews' Energy Balance

An energy balance on the epilayer as a whole has been used by Matthews (1975) as an alternate means of deriving the critical thickness. If an orthogonal grid of dislocations is introduced at the substrate/epilayer interface, the total elastic energy of the system per unit area in approximately given by

$$E = \frac{2\mu(1+\nu)\epsilon^2 h}{(1-\nu)} + \frac{\mu b^2(1-\nu\cos^2\beta)}{2\pi(1-\nu)d}\ln(\frac{\alpha h}{b}), \qquad (2.2.12)$$

where ϵ is the value of the net biaxial strain in the epilayer. The contribution to this energy from the dislocations in the epilayer has not been

well understood. Matthews (1975) described the dislocations as "noninteracting", implying that only the self energy of the dislocations is included in the total energy. This is incorrect; a term which represents a portion of the dislocation–dislocation interaction energy is included in the above equation. It will be shown later that if the dislocations are truly noninteracting, then when h is greater than the critical thickness, an infinite number of dislocations can be introduced to the epilayer while lowering the total energy of the system. Now since

$$\epsilon = f - \frac{b\sin\beta\cos\varphi}{d}, \tag{2.2.13}$$

$$E = \frac{2\mu(1+\nu)\epsilon^2 h}{(1-\nu)} + \frac{\mu b(f-\epsilon)(1-\nu\cos^2\beta)}{2\pi(1-\nu)\sin\beta\cos\varphi}\ln\left(\frac{\alpha h}{b}\right). \tag{2.2.14}$$

For a given thickness h, a minimum in the elastic energy of the system as a function of ϵ is obtained by setting $\frac{dE}{d\epsilon} = 0$. The value of ϵ at which the energy of the system is minimized is

$$\epsilon = \frac{b(1-\nu\cos^2\beta)}{8\pi h(1+\nu)\sin\beta\cos\varphi}\ln\left(\frac{\alpha h}{b}\right). \tag{2.2.15}$$

As the spacing of the dislocations becomes infinite (the condition for the critical thickness), $\epsilon \to f$, and

$$h_c = \frac{b(1-\nu\cos^2\beta)}{8\pi f(1+\nu)\sin\beta\cos\varphi}\ln\left(\frac{\alpha h_c}{b}\right). \tag{2.2.16}$$

The preceding analysis applies to the case of a homogeneous uncapped epilayer. Houghton *et al.* (1990) have extended the treatment to include superlattices and capped epilayers. The result for the critical thickness takes the same form as above, but f is replaced by f_{avg}, where f_{avg} is the average misfit of the epilayer.

iii) Analysis of Dislocation Interactions

Willis *et al.* (1990) have developed a method for determining the elastic energy of a periodic array of misfit dislocations in a strained epitaxial layer with dislocation–dislocation interactions fully accounted for. The one–dimensional array made up of mixed dislocations shown in fig. 2.3 served as the basis of their analysis. An orthogonal grid of dislocations generated by these arrays lying at right angles to each other was taken to represent the relief of biaxial misfit in real systems. In those cases in which the geometry of the system required that the mixed dislocations include a screw component, the two arrays were aligned such that the screw components formed a twist boundary. This is an important point; as will be discussed later such an array is unlikely to be found in practice, and other arrays serve as better descriptions of the dislocations which are actually introduced in relief of biaxial strain in epitaxial layers.

The method used by Willis *et al.* (1990) splits the strain field of the array of orthogonal dislocations into two components: a uniform field corresponding to the average strain of the array and a field fluctuating about

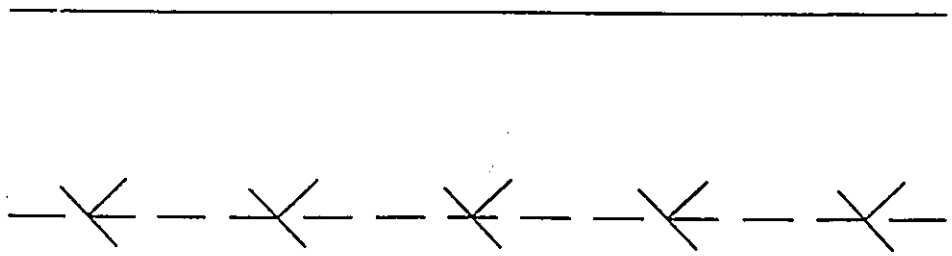

Figure 2.3: One–dimensional array of mixed dislocations having a similar orientation lying parallel to the free surface in a semi–infinite solid.

an average value of zero representing the periodically varying strain of the array. Neither the screw components (which form a twist boundary) nor the edge components with their Burgers vectors perpendicular to the free surface (which form a dislocation wall) have long–range stress fields and they therefore do not contribute to the average strain of the array – the only component which does so is that which relieves strain in the epilayer. All three components, however, have an associated fluctuating strain field. The energy of this field was determined using Fourier series and added to the energy of the uniform field in order to arrive at the total elastic energy of the dislocation array.

A major result (Jain *et al.* 1992) of the full treatment of the energy of the dislocation array under discussion is that the critical thickness for Si(100) takes on a value which is different from those previously determined (e.g. Matthews 1975). At the critical thickness, a finite number of dislocations are present in the epilayer, that is, the nature of the dislocation–dislocation interactions is such that the energy of the system is minimized at a finite dislocation spacing. This new value is referred to by Jain *et al.* as the "correct" critical thickness, although, as has been mentioned, this array is most unlikely to be found in practice. Localized forces acting on dislocations in the array shown in fig 2.3 were also determined; these too will vary in different types of arrays relieving misfit in an epilayer.

More recently an alternative method for evaluating dislocation interactions in arrays near a free surface based on the summation of

dislocation–pair interactions has been adopted by Atkinson and Jain (1992) (for arrays of edge dislocations) and by Jain *et al.* (1993) (for arrays of dislocations having a non–uniform spacing). A similar approach has been carried out independently in this thesis and applied to both the array of dislocations considered by Willis *et al.* (1990) and to an array of dislocations in which components not relieving misfit strain alternate in sign along the length of the array.

2.2.2. The Nucleation of Dislocations in $Si_{1-x}Ge_x$/Si Strained Layer Structures

A) Perfect Dislocations

If an $Si_{1-x}Ge_x$/Si strained layer structure is grown above its critical thickness, it becomes energetically favourable to introduce misfit dislocations to the substrate/epilayer interface. Among the possible sources for dislocations are

1) The homogeneous nucleation of half–loops (either whole or partial) at the free surface of the epilayer.

2) The homogeneous nucleation of half–loops at the substrate/epilayer interface.

3) The heterogeneous nucleation of complete loops at a growth defect in the bulk of the epilayer.

4) The extension of threading dislocations introduced during growth.

5) The nucleation of half–loops at defects at the edges of the sample or at the free surface.

6) The multiplication of dislocations by cross–slip or through sources such as the Hagen–Strunk source (Hagen and Strunk 1978) or the diamond defect (Eaglesham *et al.* 1989).

Other dislocations sources such as the nucleation of dislocations at the edge of islands on the free surface (Matthews 1966) or nucleation at the base of cracks in the epilayer (Matthews 1971) are also possible.

The homogeneous nucleation of a dislocation half–loop at the free surface is energetically more favourable than the homogeneous nucleation of a complete loop at the substrate/epilayer interface (Hirth and Lothe 1982). The energy of formation of a perfect half–loop on a plane inclined at an angle φ with respect to the growth surface is the sum of the elastic energy of the loop and the surface energy of the step associated with the loop, minus a term arising from the strain in the epilayer relieved by the presence of the loop. The elastic energy of the half–loop is approximately (Marée *et al.* 1987)

$$E_{loop} = \frac{\pi r}{2}\left(\frac{\mu b^2}{4\pi} + \frac{\mu b^2}{4\pi(1-\nu)}\right)\ln\left(\frac{\alpha r}{b}\right)$$

$$= \mu b^2 r \frac{(1-\nu/2)}{4(1-\nu)}\ln\left(\frac{\alpha r}{b}\right), \qquad (2.2.17)$$

while the surface energy of the associated step is (Marée *et al.* 1987)

$$E_{step} = 2rb\sin\beta\gamma_s, \tag{2.2.18}$$

where γ_s is the surface energy per unit area. The elastic energy in the epilayer released by the half–loop is

$$E_{el} = \frac{\pi r^2}{2} b\sigma\cos\lambda\cos\varphi. \tag{2.2.19}$$

As r increases from zero, the half–loop energy increases for small r, reaches a maximum value of E_c when $\frac{dE}{dr} = 0$, and then decreases as r increases. The energy is at a maximum of

$$E_{hlc} = r_c\left[\frac{\mu b^2(1 - \nu/2)}{8(1 - \nu)}(-1 + \ln(\frac{\alpha r_c}{b}))\right] \tag{2.2.20}$$

(Marée *et al.* 1987) at a radius of

$$r_c = \frac{1}{\pi b\sigma\cos\lambda\cos\varphi}\left[\frac{\mu b^2(1 - \nu/2)}{4(1 - \nu)}\cdot(1 + \ln(\frac{\alpha r_c}{b}))\right] \tag{2.2.21}$$

Assuming that activated complexes are in equilibrium with the defect–free state, the nucleation rate is given by $N = fC_0\exp(\frac{-E_c}{kT})$ nuclei $m^{-3}s^{-1}$, where f is a complex function depending of the vibration frequency of atoms in the

lattice, the activation energy for diffusion, and the length of the critical nucleus. Note that since E_{hlc} varies as b^3, there is a strong tendency for the loop to decompose into two partials bounding a stacking fault. If a partial dislocation with an associated stacking fault having energy γ_{sf} is nucleated, the critical radius becomes

$$r_c = \frac{1}{\pi(b\sigma\cos\lambda\cos\varphi - \gamma_{sf})}\left[\frac{\mu b^2(1 - \nu/2)}{4(1 - \nu)}\cdot(1 + \ln(\frac{\alpha r_c}{b}))\right], \qquad (2.2.22)$$

because of the extra term $E_{fault} = \frac{\pi r^2}{2}\gamma_{sf}$ which is added to the half–loop energy.

The expressions for the elastic energy of the half–loop may vary – it is possible, for instance, to use the formula of Bacon and Crocker (1965) or Nabarro's formula (Nabarro 1967), but in any case activation energy calculations indicate that homogeneous nucleation of half–loops is unlikely at misfits of less than 2% if the standard core parameter $\alpha = 4$ for diamond cubic structures is used. Hull and Bean (1989) have argued that the atomic scale motion of Ge and/or Si atoms should lower the core energy energy so that a value of $\alpha = 2$ is more appropriate. In addition, the potential clustering of Ge atoms (Hull and Bean 1989) could lower the activation energy barrier by creating localized stresses favourable for nucleation near the free surface. Their calculations predict that homogeneous nucleation is

unfeasible only when the germanium concentration in the epilayer is less than approximately 20%, which corresponds to a misfit strain of 0.8%.

Since the homogeneous nucleation of dislocations requires large activation energies, it is to be expected that most misfit dislocations which are generated in silicon–germanium strained layer structures arise from heterogeneous sources. A number of heterogeneous sources have been identified. It has been shown (Perovic *et al.* 1990) that local stress concentrations at surface irregularities can nucleate dislocations. A regenerative source consisting of a prismatic loop with Burgers vector $\frac{a}{6}\langle 114\rangle$ surrounding an intrinsic fault on a $\{111\}$ plane and known as the diamond defect has been observed in a series of Si–Ge alloys grown on Si(100) (Eaglesham *et al.* 1989). However, this source has not been commonly observed. A more frequently reported heterogeneous source is a particulate imperfection in the deposit. An example of this is the preferential nucleation of dislocations at SiC particles (Perovic *et al.* 1989); this, however, usually takes place during the growth of the strained layer. The extension during annealing of threading dislocations having their origin in the substrate has been observed in systems based on GaAs (Matthews and Blakeslee 1974), but the quality of Si substrates now available is such that they are virtually dislocation–free, and so this source of misfit dislocations is not observed in Si–Ge epitaxy.

B) Partial Dislocations and Sequences of Partials

The relief of strain via the nucleation of partial dislocations in

strained epitaxial layers requires a careful consideration of the geometry of the system. An examination of the stacking of {111} planes in a diamond cubic structure with a [100] growth direction reveals that an epilayer in tension (e.g. Si on Ge) may be relieved by a 90° $\frac{a}{6}\langle 211\rangle$ dislocation. An epilayer in compression (e.g. Ge on Si) cannot be relieved in this way – such a displacement leads to the formation of a high–energy fault (Marée *et al.* 1987). If a partial of the type $\frac{a}{6}\langle 211\rangle$ relieves an epilayer in compression, it must have $\beta = 30°$.

As has been seen, theory predicts that when a perfect dislocation loop is nucleated at a free surface, it is energetically favourable for one of the partials of which it is composed to be nucleated separately. When the epilayer is in compression, the 30° partial must be nucleated first; this is followed by a 90° partial which tends to be driven toward the first (Marée *et al.* 1987). In this case the two partials are bound together. However, the first partial nucleated in an epilayer under biaxial tension has $\beta = 90°$. It may well expand on its own, for the energy of a single 90° partial half–loop is lower than that of a complete extended one (Marée *et al.* 1987). These considerations lead to the expectation that partial dislocations are more likely to be observed in epilayers under biaxial tension than under biaxial compression. This is in fact what has been observed – relaxation by 90° degree partials and microtwins arising from the successive glide of 90° dislocations on adjacent {111} planes have been observed in tensile Si–Ge strained layer structures (Wegscheider *et al.* 1990), while relaxation in compressive Si–Ge strained layer structures has been observed to occur

through 60° $\frac{a}{2}\langle 110\rangle$ dislocations, or, at larger misfits, 90° Lomer dislocations (Kvam *et al.* 1987). There has been one report of stacking faults and partial dislocations found in a layer of Ge grown on Si(100) (LeGoues, Copel and Tromp 1990), but these formed only in relief of highly localized stresses in the vicinity of growth defects.

2.2.3. Propagation and Multiplication of Dislocations

A) Dislocation Velocity

A knowledge of the velocity of dislocations is important in predicting the relaxation rates of strained layer structures during annealing treatments. The velocity of dislocations driven by the internal stress field of Si–Ge strained layers is similar to that observed in pure Si under external driving forces. In the latter case (Alexander 1986), it has been found that the velocity for the thermally activated glide of dislocations at low strains follows

$$V = V_0\left(\frac{\tau}{\tau_0}\right)^m \exp\left(\frac{-Q}{kT}\right), \qquad (2.2.23)$$

where V is the dislocation velocity, V_0 is a material constant, $\tau_0 = 1$ kg/mm^2, m is an empirical constant with $1 \leq m \leq 2$, Q is the activation energy, k is Boltzmann's constant, and T is the temperature in degrees Kelvin. The form of the above equation may be explained using the Hirth and Lothe double kink theory (Hirth and Lothe 1982). In the case of

dislocation propagation in Si–Ge strained layers, Houghton (1990) has shown that in a low misfit dislocation regime

$$V = V_0\left(\frac{\tau_{eff}}{\mu}\right)^m \exp\left(\frac{-Q}{kT}\right), \qquad (2.2.24)$$

where V_0 is a material constant and τ_{eff} is given by the difference between the driving force on the threading arm of the dislocation due to the biaxial strain in the epilayer and the resistance to propagation offered by the line tension of the misfit dislocation lain down as the threading arm propagates. The value of the stress exponent m was found to be 2.0 ± 0.1, while that of Q was found to be 2.25 ± 0.05 eV for 60° $\frac{a}{2}\langle 110\rangle$ dislocations.

B) Multiplication

In addition to depending on the rate of dislocation nucleation and propagation, the relaxation kinetics of strained epitaxial layers is dependent on the extent to which dislocation multiplication takes place. A mechanism for the multiplication of dislocations was proposed by Hagen and Strunk (1978) in which orthogonal 60° dislocations react to form two threading segments generating fresh misfit dislocations. However, this mechanism is not generally accepted and it is now believed that cross–slip (Tuppen *et al.* 1990; Capano 1992) serves as the predominant mechanism through which dislocations can multiply. Capano (1992) has suggested that there is a minimum layer thickness which is necessary to accommodate the cross–slip

process required for dislocation multiplication. Once this thickness is exceeded, the rate of epilayer relaxation may be significantly enhanced.

C) Relaxation Kinetics

A knowledge of the rates of dislocation nucleation, propagation, and multiplication permits, in principle, the overall rate of strain relaxation in an epilayer to be determined. Although a number of efforts have been made to develop a unified law for the rate of epilayer relaxation, none have proven to be entirely satisfactory. Dodson and Tsao (1987) assumed that the rate of increase of misfit dislocations was given by

$$\frac{d\rho}{dt} = \rho V K \tau_{eff}, \qquad (2.2.25)$$

where ρ is the number of misfit dislocations, V is the dislocation velocity, τ_{eff} is the effective stress acting on the dislocations, and K is an empirical constant. The integration of equation (2.2.25) gives an expression for strain relaxation as a function of time. Nix *et al.* (1990) took

$$\frac{d\rho}{dt} = \rho V K, \qquad (2.2.26)$$

where K is again an empirical constant. Neither of the above approaches took into account the effect of dislocation–dislocation interactions. Jain *et al.* (1992) considered modifications of these approaches with dislocation interactions included, but were unable to obtain a model which matched all available experimental data. A different approach to the problem of relaxation kinetics

has been taken by Houghton (1991). Taking only dislocation nucleation and propagation into account, he derived an expression for relaxation kinetics in an epilayer which applies only to the initial stages of strain relaxation. The rate of relaxation was found to be very sensitive to the value of effective stress active in the epilayer.

2.3. Electron Microscopy

The theory of electron diffraction and imaging as applied to the transmission electron microscopy of crystalline defects, largely developed in the late 1950's and early 1960's, is now well established (Hirsch *et al.* 1977). What follows is a brief review of those parts of the theory which are relevant to the TEM work performed in this thesis.

A) Kinematical Diffraction

Many of the effects found in electron diffraction patterns can be explained in terms of the kinematical theory of diffraction, which considers only single electron scattering events. Some of the basic results of this theory follow. In an infinite crystal the difference between the incident and diffracted wavevectors must be equal to a reciprocal lattice vector (Cowley 1984). This condition may be represented geometrically by the Ewald sphere construction (Cowley 1984). For a given crystal orientation relative to the incident electron beam a distinct diffraction pattern is produced. In the case of diffraction from thin crystals a broader distribution of diffracted intensity in space is allowed;

in general this distribution is given by the Fourier transform of the crystal shape (Hirsch *et al.* 1977). When a crystal contains small regions of a second phase, the broadening of diffraction spots giving rise to streaking effects is common.

If a thin crystal is heavily twinned, both matrix reflections and extra spots corresponding to the presence of twins appear at certain crystal orientations. The relationship between the matrix and twin reflections has been described by Hirsch *et al.* (1977). They give expressions which may be used to index twin reflections in terms of matrix indices and to obtain twinning zone axes lying parallel to the matrix zone axis. Twinning reflections appearing in the same diffraction pattern as matrix reflections do not necessarily lie in the zero order Laue zone, occupying instead a layer of reciprocal space very close to that zone. For twins which are very thin and form platelets embedded in the matrix, the diffracted intensity distribution associated with a twinning reflection takes the form of a rod lying normal to the broad face of the platelet. When many of these twins are present in a crystal, the electron diffraction patterns are marked by twinning reflections which are extended into streaks.

B) The Two–Beam Dynamical Theory of Imaging

It has been found that the theory of electron imaging based on single scattering events (kinematical theory) is valid only under special conditions. In general it is necessary to consider multiple scattering events in a theory of

imaging in order to account for many of the features found in electron images. Theories which take into account multiple scattering events are known as dynamical theories. The simplest of these is the two–beam theory, which provides an adequate framework for many electron microscopy investigations of crystalline defects.

The two–beam theory may be formulated in terms of either wave optics or wave mechanics (Hirsch *et al.* 1977). An important finding of the theory is that the wavefunction inside the crystal is described by two Bloch waves, one of which is much more strongly scattered than the other. This strong scattering of one of the Bloch waves is known as anomalous absorption, and is responsible for some of the important contrast effects found in images of defects such as dislocations and stacking faults.

The equations describing the incident and diffracted amplitudes at a point in the x–y plane (z is parallel to the electron beam) in the wave–optical formulation of the two–beam theory are (Hirsch *et al.* 1977)

$$\frac{d\phi_0}{dz} = -\frac{\pi}{\xi_0'}\phi_0 + \pi\left(\frac{i}{\xi_g} - \frac{1}{\xi_g'}\right)\phi_g$$

$$\frac{d\phi_g}{dz} = \pi\left(\frac{i}{\xi_g} - \frac{1}{\xi_g'}\right)\phi_0 + \left(-\frac{\pi}{\xi_0'} + 2\pi i(s + \beta_g')\right)\phi_g, \quad (2.3.1)$$

where ϕ_0 and ϕ_g are the amplitudes of the incident and diffracted beams respectively, ξ_g is the extinction distance associated with the diffracted beam, ξ_0' and ξ_g' are terms which account for anomalous absorption, s measures the

deviation from the Bragg angle, and $\beta'_g = g \cdot \frac{dR}{dz}$,where g is the reciprocal lattice vector used to form the image and R is the displacement field of the crystalline defect. These expressions (known as the Howie–Whelan equations) make use of the "column approximation" in which the diffraction events in a small column of material parallel to the z–axis are taken to be independent of the events in adjacent columns. The conditions under which the column approximation is valid have been examined by Howie and Basinski (1968).

An important application of the two–beam theory is to the study of dislocations. A simulated image may be obtained by inserting the displacement field of the dislocation in an infinite elastic medium into the Howie–Whelan equations and integrating numerically (Howie and Whelan 1962). When the dislocation is very close to a free surface, the displacement field must be modified in order to satisfy the zero–traction condition at the surface (Head 1953). If the dislocation is in an isotropic elastic medium, then there are conditions under which it is invisible if it is purely edge or screw in character. Mixed dislocations, however, are always visible in the two–beam case.

Another application of the theory is to the analysis of the contrast generated by small coherent misfitting particles of a second phase. By using the displacement field of a coherent misfitting particle in the numerical integration of the Howie–Whelan equations, Ashby and Brown (1963) have shown that when a small coherent particle is less than half an extinction distance from the foil surface a strong asymmetrical image results. When the

region near the particle is imaged at the Bragg condition using the diffracted beam, a black/white asymmetry is present, the sense of which depends on whether the misfit is of the "vacancy" or "interstitial" type and on the direction of g. In the case of "interstitial" misfit, the contrast of a dark field image on a positive print is such that g points from white to black. This result is reversed for misfit of the "vacancy" type.

CHAPTER 3

Dislocation Energetics in a Half–Space

3.1 The Energetics of Dislocation Arrays in Strained Epitaxial Layers

3.1.1. General Method

Two one–dimensional arrays of dislocations of spacing d at the interface between a substrate and a strained epilayer of thickness h are examined. Together the substrate and epilayer make up a semi–infinite, elastically isotropic medium having a single set of elastic constants μ and ν in which the epilayer is subjected to a uniform mismatch strain $e_{ij}^{epi} = f\delta_{ij}$, where

$$f = \frac{a_{sub} - a_{epi}}{a_{epi}} , \qquad (3.1.1)$$

and a_{sub} and a_{epi} are the lattice parameters of the (cubic) substrate and epilayer respectively.

The following arrays are considered:

(i) An array of mixed dislocations characterized by two angles β and

φ, where β is the angle between the Burgers vector of the dislocation and the dislocation line, and φ is the angle that the slip plane makes with the free surface. All dislocations have an identical orientation.

(ii) An array of mixed dislocations characterized by β and φ in which those components of the Burgers vector not relieving misfit strain alternate in sign along the length of the array. These two types of array together with the coordinate system used to describe their elastic fields are illustrated in fig. 3.1.

The total elastic energy per unit area of the system as a whole is evaluated for both arrays. This energy is given by

$$E_{total} = E_{epi} + E_{disl}$$

$$+ E_{int,disl/epi} + E_{int,disl/disl,} \qquad (3.1.2)$$

where $E_{epi} = \frac{2\mu(1+\nu)f^2h}{(1-\nu)}$ is the energy per unit area of the epilayer, E_{disl} is the energy per unit area of the dislocation array, neglecting interactions between dislocations, $E_{int,disl/epi}$ is the interaction energy per unit area between the dislocation array and the epilayer, and $E_{int,disl/disl}$ is the interaction energy per unit area between the dislocations which make up the array. Each of the components of the total energy is examined separately. The equilibrium dislocation spacing at a given lattice mismatch and epilayer thickness is obtained by determining that value of d which minimizes the

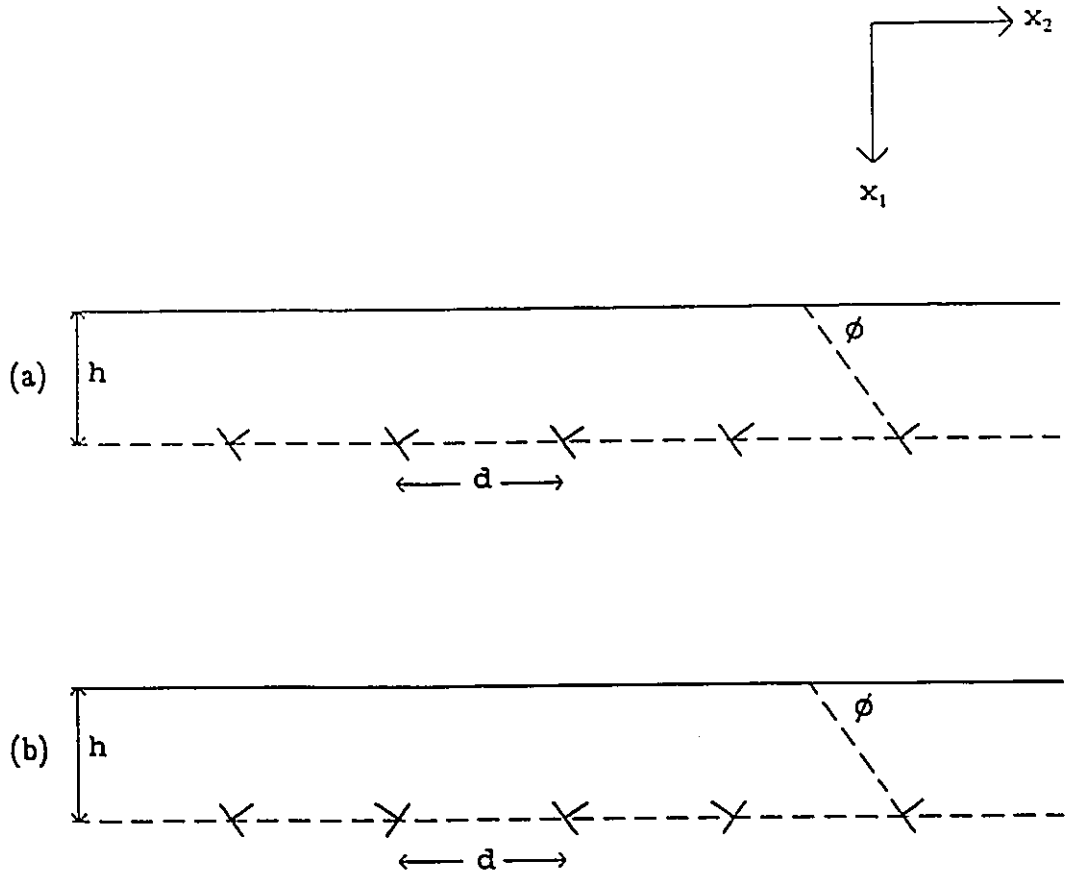

Figure 3.1: One–dimensional arrays of mixed dislocations having (a) similar and (b) alternating orientations lying parallel to the free surface in a semi–infinite solid.

total energy of the system. Surface steps associated with an edge dislocation lying on a slip plane which is not parallel to the free surface are ignored. Such steps have a surface energy as well as their own elastic fields, but these terms do not make an appreciable contribution to the total energy of the system, and their omission does not alter any of the basic results obtained in the analysis.

Corresponding two–dimensional arrays of dislocations are also studied. Each array is an orthogonal grid of dislocations, so that an additional term representing the interaction between the two orthogonal sets of dislocations must be included in the expression for the total energy per unit area, giving

$$E_{total} = E_{epi} + E_{disl} + E_{int,disl/epi}$$

$$+ E_{int,disl/disl} + E'_{int,disl/disl,} \qquad (3.1.3)$$

where $E'_{int,disl/disl}$ is the interaction energy per unit area between the orthogonal dislocations. The equilibrium spacing of the two–dimensional arrays is then given by minimizing the total energy of the system.

3.1.2. Dislocation Self Energy

The energy of a dislocation a distance h from a free surface may be calculated through the appropriate integrations of stresses in a manner similar to the case of a dislocation in an infinite crystal. An edge dislocation having

a Burgers vector b parallel to the free surface and of a sign which would relieve an epilayer in tension has the following stress field (Head 1953):

$$\sigma_{11} = \frac{\mu b}{2\pi(1-\nu)}\left[\frac{(x_1-h)((x_1-h)^2-x_2^2)}{((x_1-h)^2+x_2^2)^2} - \frac{(x_1+h)((x_1+h)^2-x_2^2)}{((x_1+h)^2+x_2^2)^2}\right.$$

$$\left. + 2h\,\frac{(3x_1+h)(x_1+h)^3 - 6x_1(x_1+h)x_2^2 - x_2^4}{((x_1+h)^2+x_2^2)^3}\right]$$

$$\sigma_{22} = \frac{\mu b}{2\pi(1-\nu)}\left[\frac{(x_1-h)((x_1-h)^2+3x_2^2)}{((x_1-h)^2+x_2^2)^2} - \frac{(x_1+h)((x_1+h)^2+3x_2^2)}{((x_1+h)^2+x_2^2)^2}\right.$$

$$\left. - 2h\,\frac{(x_1-h)(x_1+h)^3 - 6x_1(x_1+h)x_2^2 + x_2^4}{((x_1+h)^2+x_2^2)^3}\right]$$

$$\sigma_{12} = \frac{\mu b}{2\pi(1-\nu)}\left[\frac{x_2((x_1-h)^2-x_2^2)}{((x_1-h)^2+x_2^2)^2} - \frac{x_2((x_1+h)^2-x_2^2)}{((x_1+h)^2+x_2^2)^2}\right.$$

$$\left. + 4hx_1x_2\,\frac{3(x_1+h)^2 - x_2^2}{((x_1+h)^2+x_2^2)^3}\right]. \qquad (3.1.4)$$

If an edge dislocation has a Burgers vector b perpendicular to the free surface, then its stress field is (Head 1953):

$$\sigma_{11} = \frac{\mu b}{2\pi(1-\nu)}\left[-\frac{x_2(3(x_1-h)^2+x_2^2)}{((x_1-h)^2+x_2^2)^2} + \frac{x_2(3(x_1+h)^2+x_2^2)}{((x_1+h)^2+x_2^2)^2}\right.$$

$$\left. + 4hx_1x_2\,\frac{3((x_1+h)^2-x_2^2)}{((x_1+h)^2+x_2^2)^3}\right]$$

$$\sigma_{22} = \frac{\mu b}{2\pi(1-\nu)}\left[\frac{x_2((x_1-h)^2-x_2^2)}{((x_1-h)^2+x_2^2)^2} - \frac{x_2((x_1+h)^2-x_2^2)}{((x_1+h)^2+x_2^2)^2}\right.$$

$$\left. + 4hx_2\frac{(2h-x_1)(x_1+h)^2 + (3x_1+2h)x_2^2}{((x_1+h)^2+x_2^2)^3}\right]$$

$$\sigma_{12} = \frac{\mu b}{2\pi(1-\nu)}\left[\frac{(x_1-h)((x_1-h)^2-x_2^2)}{((x_1-h)^2+x_2^2)^2} - \frac{(x_1+h)((x_1+h)^2-x_2^2)}{((x_1+h)^2+x_2^2)^2}\right.$$

$$\left. +2h\,\frac{(h-x_1)(x_1+h)^3 + 6x_1(x_1+h)x_2^2 - x_2^4}{((x_1+h)^2+x_2^2)^3}\right]. \qquad (3.1.5)$$

The stress field of a screw dislocation near a free surface is given by a simple image construction (Hirth and Lothe 1982):

$$\sigma_{13} = -\frac{\mu b}{2\pi}\left[\frac{x_2}{(x_1-h)^2+x_2^2} - \frac{x_2}{(x_1+h)^2+x_2^2}\right]$$

$$\sigma_{23} = \frac{\mu b}{2\pi}\left[\frac{x_1}{(x_1-h)^2+x_2^2} - \frac{x_1}{(x_1+h)^2+x_2^2}\right]. \qquad (3.1.6)$$

The energy per unit length (ignoring the work done by tractions on the core surface as the dislocation is formed) of the three dislocations can then be determined by the appropriate integration. For an edge dislocation with b parallel to the free surface

$$U_{disl} = \frac{\mu b^2}{4\pi(1-\nu)}\left[\int_{r_0}^{\infty}\frac{1}{x_2}dx_2 + \int_{r_0}^{\infty}\frac{4h^2x_2 - x_2^3}{(x_2^2+4h^2)^2}dx_2 - \int_{r_0}^{\infty}\frac{48h^4x_2 - 4h^2x_2^3}{(x_2^2+4h^2)^3}dx_2\right] + U_{core}$$

$$= \frac{\mu b^2}{4\pi(1-\nu)}\left[\left[\ln(x_2)\right]_{r_0}^{\infty} - \left[\tfrac{1}{2}\ln(x_2^2+4h^2)\right]_{r_0}^{\infty}\right.$$

$$\left. + \left[\frac{-6h^2}{(x_2^2+4h^2)} + \frac{16h^4}{(x_2^2+4h^2)^2}\right]_{r_0}^{\infty}\right] + U_{core}$$

$$= \frac{\mu b^2}{4\pi(1-\nu)}\left[\tfrac{1}{2}\ln\left(\frac{r_0^2+4h^2}{r_0^2}\right) + \frac{6h^2}{(r_0^2+4h^2)}\right.$$

$$\left. - \frac{16h^4}{(r_0^2+4h^2)^2}\right] + U_{core}, \quad h>r_0. \qquad (3.1.7)$$

When $r_0<<h$,

$$U_{disl} = \frac{\mu b^2}{4\pi(1-\nu)}\left[\ln\left(\frac{2h}{r_0}\right) + \tfrac{1}{2}\right] + U_{core}. \qquad (3.1.8)$$

Further details concerning the above integration may be found in the appendix. For an edge dislocation with **b** perpendicular to the free surface,

$$U_{disl} = \frac{\mu b^2}{4\pi(1-\nu)}\left[\int_{r_0+h}^{\infty}\frac{1}{x_1-h}dx_1 - \int_{r_0+h}^{\infty}\frac{1}{x_1+h}dx_1 + \int_{r_0+h}^{\infty}\frac{2h(h-x_1)}{(x_1+h)^3}dx_1\right] + U_{core}$$

$$= \frac{\mu b^2}{4\pi(1-\nu)}\left[\left[\ln(x_1-h)\right]_{r_0+h}^{\infty} - \left[\ln(x_1+h)\right]_{r_0+h}^{\infty}\right.$$

$$\left. + \left[\frac{hx_1-h^2}{(x_1+h)^2} + \frac{h}{(x_1+h)}\right]_{r_0+h}^{\infty}\right] + U_{core}$$

$$= \frac{\mu b^2}{4\pi(1-\nu)}\left[\ln\left(\frac{r_0+2h}{r_0}\right) - \frac{r_0 h}{(r_0+2h)^2} - \frac{h}{(r_0+2h)}\right] + U_{core}, \quad h>r_0. \tag{3.1.9}$$

When $r_0<<h$,

$$U_{disl} = \frac{\mu b^2}{4\pi(1-\nu)}\left[\ln\left(\frac{2h}{r_0}\right) - \tfrac{1}{2}\right] + U_{core}. \tag{3.1.10}$$

For a screw dislocation in a half-space,

$$U_{disl} = \frac{\mu b^2}{4\pi}\left[\int_{r_0}^{\infty}\frac{1}{x_2}dx_2 - \int_{0}^{\infty}\frac{x_2}{x_2^2+4h^2}dx_2\right] + U_{core}$$

$$= \frac{\mu b^2}{4\pi}\ln\left(\frac{2h}{r_0}\right) + U_{core}, \quad h>r_0. \tag{3.1.11}$$

In these expressions, U_{core} is the energy per unit length of the dislocation core and r_0 is the core radius.

A dislocation having edge components $b\sin\beta\cos\varphi$ parallel to the free surface and $b\sin\beta\sin\varphi$ perpendicular to the free surface as well as a screw component $b\cos\beta$ has an energy given by the sum of the energies of its component dislocations and the interactions between them. It is obvious from the sense of the displacements that the screw component does not interact

with either edge component. The interaction between the edge components is most easily calculated by forming the dislocation of Burgers vector $b\sin\beta\sin\varphi$ in the presence of the dislocation having its Burgers vector parallel to the free surface. Since there is no shear stress at $x_2 = 0$ opposing the formation of the dislocation with Burgers vector $b\sin\beta\sin\varphi$, there is no interaction between the two dislocations, and the energy of the mixed dislocation is

$$U_{disl} = \frac{\mu b^2(1-\nu\cos^2\beta)}{4\pi(1-\nu)} \ln\left(\frac{2h}{r_0}\right)$$

$$+ \frac{\mu b^2 \sin^2\beta}{4\pi(1-\nu)}\left(\tfrac{1}{2}\cos^2\varphi - \tfrac{1}{2}\sin^2\varphi\right) + U_{core}, \quad h>r_0. \qquad (3.1.12)$$

This result is similar to that obtained by Freund (1990), but in the present case the work done by the tractions on the surface of the dislocation core as the dislocation is formed are ignored, and unlike Freund's treatment (1990), the energy of the non–linear elastic material which makes up the core is included. If the latter term is not taken into account, then the dislocation energy per unit length in the present treatment is greater than that of the work of Freund (1990) and Jain *et al.* (1992) by the amount $\frac{\mu b^2 \sin^2\beta(1-2\nu)}{16\pi(1-\nu)^2}$. Equation (3.1.12) may be written in the form

$$U_{disl} = \frac{\mu b^2(1-\nu\cos^2\beta)}{4\pi(1-\nu)} \ln\left(\frac{\alpha h}{b}\right), \quad h>r_0, \qquad (3.1.13)$$

provided that

$$\alpha = \frac{2b}{r_0} \exp\left[\frac{\mu b^2 \sin^2\beta(\frac{1}{2}\cos^2\varphi - \frac{1}{2}\sin^2\varphi)+4\pi(1-\nu)U_{core}}{\mu b^2(1-\nu\cos^2\beta)}\right]. \qquad (3.1.14)$$

If the work done by surface tractions on the core of the dislocation is included in the expression for the self energy of the dislocation, then

$$\alpha = \frac{2b}{r_0} \exp\left[\frac{\mu b^2 \sin^2\beta\left[\frac{1}{2}(\cos^2\varphi - \sin^2\varphi) - \frac{1-2\nu}{4(1-\nu)}\right] + 4\pi(1-\nu)U_{core}}{\mu b^2(1-\nu\cos^2\beta)}\right]. \qquad (3.1.15)$$

Dividing equation (3.1.12) by d gives the energy per unit area of an array of dislocations of spacing d in which interactions between dislocations are neglected. Thus

$$E_{disl} = \frac{1}{d}\left[\frac{\mu b^2(1-\nu\cos^2\beta)}{4\pi(1-\nu)} \ln(\frac{2h}{r_0}) + \frac{\mu b^2 \sin^2\beta}{4\pi(1-\nu)} (\frac{1}{2}\cos^2\varphi - \frac{1}{2}\sin^2\varphi)+U_{core}\right], \quad h>r_0. \qquad (3.1.16)$$

3.1.3. Interaction Between Dislocation and Epilayer – The Critical Thickness

A system made up of a single dislocation at the interface between a substrate and a strained epitaxial layer has an elastic energy given by the sum of the self energy of the epilayer, the self energy of the dislocation, and the interaction energy between the dislocation and the epilayer. For a dislocation lying parallel to the x_3 axis at the base of a homogeneous uncapped epilayer, the interaction energy per unit length of dislocation is

$$U_{int,disl/epi} = \int_0^h \int_{-\infty}^{+\infty} \sigma_{22}^{epi}\, e_{22}^{disl}\, dx_2 dx_1, \qquad (3.1.17)$$

where σ_{22}^{epi} is taken from the self stress tensor of the epilayer and e_{22}^{disl} is obtained from the strain tensor of the dislocation. Now

$$e_{22}^{disl} = \frac{1}{2\pi(1+\nu)}\left[(1-\nu^2)\sigma_{22}^{disl} - (\nu+\nu^2)\sigma_{11}^{disl}\right], \qquad (3.1.18)$$

and since σ_{22}^{epi} is a constant, we have, using the stress fields described previously,

$$U_{int,disl/epi} = \frac{\sigma_{22}^{epi} b \sin\beta\cos\varphi}{4\pi} \int_0^h \int_{-\infty}^{\infty} \left[\frac{(x_1-h)((x_1-h)^2+3x_2^2)}{((x_1-h)^2+x_2^2)^2} \right.$$

$$\left. - \frac{(x_1+h)((x_1+h)^2+3x_2^2)}{((x_1+h)^2+x_2^2)^2} - 2h\, \frac{(x_1-h)(x_1+h)^3 - 6x_1(x_1+h)x_2^2 + x_2^4}{((x_1+h)^2+x_2^2)^3} \right] dx_2 dx_1$$

$$- \frac{\sigma_{22}^{epi} \nu b \sin\beta\cos\varphi}{4\pi(1-\nu)} \int_0^h \int_{-\infty}^{\infty} \left[\frac{(x_1-h)((x_1-h)^2-x_2^2)}{((x_1-h)^2+x_2^2)^2} - \frac{(x_1+h)((x_1+h)^2-x_2^2)}{((x_1+h)^2+x_2^2)^2} \right.$$

$$\left. + 2h\, \frac{(3x_1+h)(x_1+h)^3 - 6x_1(x_1+h)x_2^2 - x_2^4}{((x_1+h)^2+x_2^2)^3} \right] dx_2 dx_1$$

$$+ \frac{\sigma_{22}^{epi} b \sin\beta\sin\varphi}{4\pi} \int_0^h \int_{-\infty}^{\infty} \left[\frac{x_2((x_1-h)^2-x_2^2)}{((x_1-h)^2+x_2^2)^2} - \frac{x_2((x_1+h)^2-x_2^2)}{((x_1+h)^2+x_2^2)^2} \right.$$

$$+ 4hx_2 \frac{(2h-x_1)(x_1+h)^2 + (3x_1+2h)x_2^2}{((x_1+h)^2+x_2^2)^3}\Bigg] dx_2 dx_1$$

$$- \frac{\sigma_{22}^{epi}\nu b\sin\beta\sin\varphi}{4\pi(1-\nu)} \int_0^h \int_{-\infty}^{\infty} \Bigg[- \frac{x_2(3(x_1-h)^2+x_2^2)}{((x_1-h)^2+x_2^2)^2} + \frac{x_2(3(x_1+h)^2+x_2^2)}{((x_1+h)^2+x_2^2)^2}$$

$$+ 4hx_1x_2 \frac{3((x_1+h)^2-x_2^2)}{((x_1+h)^2+x_2^2)^3}\Bigg] dx_2 dx_1. \qquad (3.1.19)$$

Because the last two integrands are odd functions of x_2, those integrals vanish. As shown in the appendix, the integral of each term in the second integrand is also equal to zero, while the third term in the first integrand contributes nothing to that integral. Then

$$U_{int,disl/epi} = \frac{\sigma_{22}^{epi} b\sin\beta\cos\varphi}{4\pi}(-4\pi h)$$

$$= \frac{-2\mu(1+\nu)fhb\sin\beta\cos\varphi}{(1-\nu)}. \qquad (3.1.20)$$

This result may also be obtained by calculating the work done on moving a dislocation from the free surface into place at the substrate/epilayer interface.

The magnitude of the interaction energy per unit area between an array of dislocations of spacing d and a strained epilayer is

$$E_{int,disl/epi} = \frac{2\mu(1+\nu)|f|hb\sin\beta\cos\varphi}{(1-\nu)d}. \qquad (3.1.21)$$

If the dislocations relieve strain in the epilayer, then the interaction energy is negative. If the epilayer is capped, or if it consists of multiple strained layers, then the magnitude of the interaction energy per unit area is found by replacing $|f|$ by $|f_{avg}|$, where f_{avg} is the average value of the misfit strain in the epilayer.

It is energetically favourable to place a dislocation at the substrate/epilayer interface when the decrease in the elastic energy of the system resulting from the interaction between the dislocation and the epilayer exceeds the self energy of the dislocation. The critical thickness h_c above which it becomes favourable to introduce a single dislocation to the substrate/epilayer interface is then given by

$$\frac{2\mu(1+\nu)|f|h_c b\sin\beta\cos\varphi}{(1-\nu)} = \frac{\mu b^2(1-\nu\cos^2\beta)}{4\pi(1-\nu)} \ln\left(\frac{\alpha h_c}{b}\right),$$

or

$$h_c = \frac{b(1-\nu\cos^2\beta)}{8\pi(1-\nu)|f|\sin\beta\cos\varphi} \ln\left(\frac{\alpha h_c}{b}\right), \qquad (3.1.22)$$

where α is defined in equation (3.1.14). Equation (3.1.22) is the classical result of Matthews (1975).

3.1.4. Analysis of One–Dimensional Dislocation Arrays

In order to fully describe the contribution of an array of dislocations of spacing d to the overall elastic energy of a strained epitaxial system, it is

necessary to determine the interaction energy between the dislocations that make up the array. Both of the arrays described in section 3.1.2 are considered. The method used to calculate the interaction energy is indicated and the results used to find the equilibrium dislocation spacing of a one–dimensional array in a strained layer.

A) Mixed Dislocations of Similar Orientation

Consider an array of N dislocations occupying a length L as shown in fig. 3.2, where L is large. Then edge effects are minor, and, to an excellent approximation, the interaction energy per unit length is given by

$$U_{int,disl/disl} = (N-1)U_d + (N-2)U_{2d} + (N-3)U_{3d}\cdots, \qquad (3.1.23)$$

where U_d, U_{2d} , U_{3d} , etc. are the interaction energies between a pair of dislocations of the same sign separated by distances d, 2d, 3d, and so on. The interaction energy per unit area as $L \to \infty$ is

$$E_{int,disl/disl} = \lim_{N\to\infty} \frac{1}{d}\left[\frac{(N-1)}{N}U_d + \frac{(N-2)}{N}U_{2d} + \frac{(N-3)}{N}U_{3d} + \ldots\right]$$

$$= \frac{1}{d}\sum_{n=1}^{\infty} U_{nd}, \qquad (3.1.24)$$

for the coefficient of each U_{nd} can be made arbitrarily close to unity for sufficiently large N.

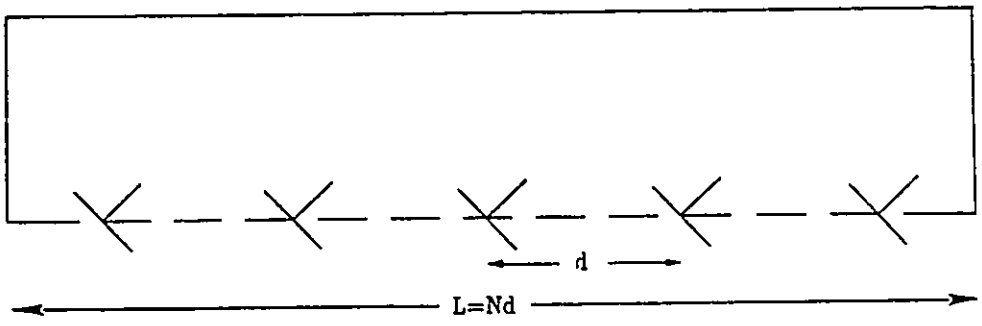

Figure 3.2: N dislocations of spacing d in a finite epilayer. L = Nd.

The interaction energy per unit length of dislocation between two edge dislocations of the same sign having their Burgers vector parallel to the free surface is given by

$$U_d = \frac{\mu b^2}{2\pi(1-\nu)}\int_d^\infty \left[\frac{1}{x_2} + \frac{4h^2x_2 - x_2^3}{(x_2^2+4h^2)^2} - \frac{48h^4x_2 - 4h^2x_2^3}{(x_2^2+4h^2)^3} \right] dx_2$$

$$= \frac{\mu b^2}{4\pi(1-\nu)} \left[\ln\left(\frac{d^2+4h^2}{d^2}\right) + \frac{12h^2d^2+16h^4}{(d^2+4h^2)^2} \right], \quad d>2r_0. \qquad (3.1.25)$$

In the case of two edge dislocations of the same sign having their Burgers vectors perpendicular to the free surface the pair interaction energy per unit length is given by

$$U_d = \frac{\mu b^2}{2\pi(1-\nu)}\int_h^\infty \left[\frac{(x_1-h)^3 - (x_1-h)d^2}{((x_1-h)^2+d^2)^2} - \frac{(x_1+h)^3 - (x_1+h)d^2}{((x_1+h)^2+d^2)^2} \right.$$

$$\left. + \frac{2h((h-x_1)(x_1+h)^3 + (6x_1^2+6hx_1)d^2 - d^4)}{((x_1+h)^2+d^2)^3} \right] dx_1$$

$$= \frac{\mu b^2}{4\pi(1-\nu)} \left[\ln\left(\frac{d^2+4h^2}{d^2}\right) - \frac{4h^2d^2+48h^4}{(d^2+4h^2)^2} \right], \quad d>2r_0. \qquad (3.1.26)$$

Further details concerning the above integration may be found in the appendix. In the case of two screw dislocations of the same sign, the interaction energy per unit length is given by

$$U_d = \frac{\mu b^2}{2\pi}\left[\int_d^\infty \frac{1}{x_2}dx_2 - \int_d^\infty \frac{x_2}{(x_2^2+4h^2)}dx_2\right]$$

$$= \frac{\mu b^2}{4\pi}\ln\left(\frac{d^2+4h^2}{d^2}\right), \quad d>2r_0. \tag{3.1.27}$$

Now screw components do not interact with edge components, and the symmetry of the array indicates that there is no net interaction between edge components of different types. Therefore these types of interactions do not need to be considered. Then for an array of mixed dislocations of similar orientation we have

$$E_{int,disl/disl} = \frac{\mu b^2(1-\nu\cos^2\beta)}{4\pi(1-\nu)d}\ln\left[\prod_{n=1}^{\infty}\left(1+\frac{4h^2}{n^2d^2}\right)\right]$$

$$+ \frac{\mu b^2\sin^2\beta\cos^2\varphi}{4\pi(1-\nu)d}\sum_{n=1}^{\infty}\frac{12n^2d^2h^2+16h^4}{(n^2d^2+4h^2)^2}$$

$$- \frac{\mu b^2\sin^2\beta\sin^2\varphi}{4\pi(1-\nu)d}\sum_{n=1}^{\infty}\frac{4n^2d^2h^2+48h^4}{(n^2d^2+4h^2)^2}, \tag{3.1.28}$$

or, making use of the series and products compiled by Hansen (1975),

$$E_{int,disl/disl} = \frac{\mu b^2(1-\nu\cos^2\beta)}{4\pi(1-\nu)d}\ln\left[\frac{d}{2\pi h}\sinh\left(\frac{2\pi h}{d}\right)\right]$$

$$+ \frac{\mu b^2\sin^2\beta\cos^2\varphi}{4\pi(1-\nu)d}\left[\frac{2\pi h}{d}\coth\left(\frac{2\pi h}{d}\right) - \frac{2\pi^2h^2}{d^2}\operatorname{csch}^2\left(\frac{2\pi h}{d}\right) - \frac{1}{2}\right]$$

$$- \frac{\mu b^2 \sin^2\beta \sin^2\varphi}{4\pi(1-\nu)d} \left[\frac{2\pi h}{d} \coth\left(\frac{2\pi h}{d}\right) + \frac{2\pi^2 h^2}{d^2} \operatorname{csch}^2\left(\frac{2\pi h}{d}\right) - \tfrac{3}{2} \right], \quad d > 2r_0. \tag{3.1.29}$$

This result is equivalent to that obtained by Willis *et al.* (1990), although the form of the equation is different. The total elastic energy per unit area of the system is

$$E_{total} = \frac{2\mu(1+\nu)f^2 h}{(1-\nu)} + \frac{1}{d}\left[\frac{\mu b^2 (1-\nu\cos^2\beta)}{4\pi(1-\nu)} \ln\left(\frac{2h}{r_0}\right) + \frac{\mu b^2 \sin^2\beta(\cos^2\varphi - \sin^2\varphi)}{8\pi(1-\nu)} + U_{core} \right]$$

$$- \frac{2\mu(1+\nu)|f|hb\sin\beta\cos\varphi}{(1-\nu)d} + \frac{\mu b^2(1-\nu\cos^2\beta)}{4\pi(1-\nu)d} \ln\left[\frac{d}{2\pi h} \sinh\left(\frac{2\pi h}{d}\right) \right]$$

$$+ \frac{\mu b^2 \sin^2\beta\cos^2\varphi}{4\pi(1-\nu)d} \left[\frac{2\pi h}{d} \coth\left(\frac{2\pi h}{d}\right) - \frac{2\pi^2 h}{d^2} \operatorname{csch}^2\left(\frac{2\pi h}{d}\right) - \tfrac{1}{2} \right]$$

$$- \frac{\mu b^2 \sin^2\beta \sin^2\varphi}{4\pi(1-\nu)d} \left[\frac{2\pi h}{d} \coth\left(\frac{2\pi h}{d}\right) + \frac{2\pi^2 h^2}{d^2} \operatorname{csch}^2\left(\frac{2\pi h}{d}\right) - \tfrac{3}{2} \right], \quad h > r_0,\ d > 2r_0. \tag{3.1.30}$$

The equilibrium spacing of this array is found by setting the partial derivative of E_{total} with respect to d equal to zero and solving for d. In the limit $h \to \infty$, we have

$$d = \frac{((1-\nu)\cos^2\beta+2\sin^2\beta\cos^2\varphi)b}{2(1+\nu)|f|\sin\beta\cos\varphi}. \qquad (3.1.31)$$

When $\beta = \frac{\pi}{2}$, $d = \frac{b\cos\varphi}{(1+\nu)|f|}$, while if $\beta = 0$, the spacing of the dislocations is infinite. If the epilayer is in a state of plane strain rather than biaxial strain (this would arise from a lattice mismatch of f along the x_2 direction and zero along the x_3 direction), then an array of mixed dislocations of similar orientation relieving this strain has, in the limit $h \to \infty$, a spacing of

$$d = \frac{((1-\nu)\cos^2\beta+2\sin^2\beta\cos^2\varphi)b}{2|f|\sin\beta\cos\varphi}. \qquad (3.1.32)$$

If the epilayer is capped, or if it consists of multiple strained layers, then the total energy and the dislocation spacings may be found by replacing f by f_{avg}.

B) Mixed Dislocations of Alternating Orientation

The energy arising from interactions between dislocations in a one–dimensional array in which those components not relieving misfit strain (i.e. screw and edge with Burgers vector perpendicular to the free surface) alternate in sign along the length of the array is best calculated by considering those components separately from the component relieving misfit strain. For the latter we have from previous results

$$E_{int,disl/disl} = \frac{\mu b^2\sin^2\beta\cos^2\varphi}{4\pi(1-\nu)d}\left[\ln\left(\prod_{n=1}^{\infty}\left(1+\frac{4h^2}{n^2d^2}\right)\right) + \frac{12n^2d^2h^2+16h^4}{(n^2d^2+4h^2)^2}\right]$$

$$= \frac{\mu b^2 \sin^2\beta\cos^2\varphi}{4\pi(1-\nu)d}\left[\ln\left(\frac{d}{2\pi h}\sinh\left(\frac{2\pi h}{d}\right)\right) + \frac{2\pi h}{d}\coth\left(\frac{2\pi h}{d}\right)\right.$$

$$\left. - \frac{2\pi^2 h^2}{d^2}\operatorname{csch}^2\left(\frac{2\pi h}{d}\right) - \tfrac{1}{2}\right], \quad d>2r_0 \ . \qquad (3.1.33)$$

For those components not relieving misfit strain we have, proceeding as before,

$$U_{int,disl/disl} = -(N-1)U_d + (N-2)U_{2d}$$

$$- (N-3)U_{3d} + (N-4)U_{4d} - \ldots \qquad (3.1.34)$$

as the interaction energy per unit length of dislocation in an array of N dislocations occupying a length L. The interaction energy per unit area between these components as $L \to \infty$ is

$$E_{int,disl/disl} = \frac{1}{d}\left[\sum_{n=0}^{\infty} -U_{(2n+1)d} + \sum_{n=1}^{\infty} U_{2nd}\right]. \qquad (3.1.35)$$

As was the case for mixed dislocations of similar orientation, it is not necessary to consider interactions between screws and edges or between edges of different types in the array. Then the energy per unit area arising from interactions between those components in the array which do not relieve misfit strain is

$$E_{int,disl/disl} = \frac{\mu b^2 \sin^2\beta \sin^2\varphi}{4\pi(1-\nu)d}\left[\ln\left(\prod_{n=1}^{\infty}\left(1+\frac{h^2}{n^2d^2}\right)\right) - \ln\left(\prod_{n=0}^{\infty}\left(1+\frac{4h^2}{(2n+1)^2d^2}\right)\right)\right]$$

$$+ \frac{\mu b^2 \cos^2\beta}{4\pi d}\left[\ln\left(\prod_{n=1}^{\infty}\left(1+\frac{h^2}{n^2d^2}\right)\right) - \ln\left(\prod_{n=0}^{\infty}\left(1+\frac{4h^2}{(2n+1)^2d^2}\right)\right)\right]$$

$$+ \frac{\mu b^2 \sin^2\beta \sin^2\varphi}{4\pi(1-\nu)d}\left[\sum_{n=0}^{\infty}\frac{4(2n+1)^2d^2h^2+48h^4}{((2n+1)^2d^2+4h^2)^2}\right.$$

$$\left. - \sum_{n=1}^{\infty}\frac{4n^2(2d)^2h^2+48h^4}{(n^2(2d)^2+4h^2)^2}\right], \quad d>2r_0, \qquad (3.1.36)$$

or in closed form (Hansen, 1975),

$$E_{int,disl/disl} = \frac{\mu b^2 \sin^2\beta \sin^2\varphi}{4\pi(1-\nu)d}\left[\ln\left(\frac{d}{\pi h}\sinh\left(\frac{\pi h}{d}\right)\right) - \ln\left(\cosh\left(\frac{\pi h}{d}\right)\right)\right]$$

$$+ \frac{\mu b^2 \cos^2\beta}{4\pi d}\left[\ln\left(\frac{d}{\pi h}\sinh\left(\frac{\pi h}{d}\right)\right) - \ln\left(\cosh\left(\frac{\pi h}{d}\right)\right)\right]$$

$$- \frac{\mu b^2 \sin^2\beta \sin^2\varphi}{4\pi(1-\nu)d}\left[\frac{\pi h}{4d^2}\left(d\coth\left(\frac{\pi h}{d}\right) - \pi h\operatorname{csch}^2\left(\frac{\pi h}{d}\right)\right)\right.$$

$$\left. + \frac{3\pi h}{4d^2}\left(d\coth\left(\frac{\pi h}{d}\right) + \pi h\operatorname{csch}^2\left(\frac{\pi d}{d}\right)\right) - \tfrac{3}{2}\right]$$

$$+ \frac{\mu b^2 \sin^2\beta \sin^2\varphi}{4\pi(1-\nu)d}\left[\frac{\pi h}{4d^2}\left(d\tanh\left(\frac{\pi h}{d}\right) + \pi h\operatorname{sech}^2\left(\frac{\pi h}{d}\right)\right)\right.$$

$$+ \frac{3\pi h}{4d^2}\left(d\tanh\left(\frac{\pi h}{d}\right) - \pi h \operatorname{sech}^2\left(\frac{\pi h}{d}\right)\right)\Bigg], \quad d>2r_0. \tag{3.1.37}$$

The total energy per unit area arising from interactions between dislocations in the array is given by the sum of equations (3.1.33) and (3.1.37):

$$E_{int,disl/disl} = \frac{\mu b^2 \sin^2\beta\cos^2\varphi}{4\pi(1-\nu)d}\Bigg[\ln\left(\frac{d}{2\pi h}\sinh\left(\frac{2\pi h}{d}\right)\right) + \frac{2\pi h}{d}\coth\left(\frac{2\pi h}{d}\right) - \frac{2\pi^2 h^2}{d^2}\operatorname{csch}^2\left(\frac{2\pi h}{d}\right) - \tfrac{1}{2}\Bigg]$$

$$+ \frac{\mu b^2 \sin^2\beta\sin^2\varphi}{4\pi(1-\nu)d}\Bigg[\ln\left(\frac{d}{\pi h}\tanh\left(\frac{\pi h}{d}\right)\right) + \frac{\pi h}{d}\left(\tanh\left(\frac{\pi h}{d}\right) - \coth\left(\frac{\pi h}{d}\right)\right) - \frac{\pi^2 h^2}{2d^2}\left(\operatorname{sech}^2\left(\frac{\pi h}{d}\right) + \operatorname{csch}^2\left(\frac{\pi h}{d}\right)\right) + \tfrac{3}{2}\Bigg]$$

$$+ \frac{\mu b^2 \cos^2\beta}{4\pi d}\ln\left(\frac{d}{\pi h}\tanh\left(\frac{\pi h}{d}\right)\right), \quad h>r_0,\ d>2r_0. \tag{3.1.38}$$

Adding this expression to $E_{epi} + E_{disl} + E_{int,disl/epi}$ gives the total elastic energy per unit area. It is possible to determine the equilibrium spacing of the array as before. As $h \to \infty$, we have

$$\lim_{h\to\infty} d = \frac{b\sin\beta\cos\varphi}{(1+\nu)|1|}. \tag{3.1.39}$$

In the case of an epilayer which is in plane strain, we have for this array

$$\lim_{h\to\infty} d = \frac{b\sin\beta\cos\varphi}{|f|}. \qquad (3.1.40)$$

3.1.5. Two–Dimensional Arrays

A) Interaction Between Orthogonal Dislocations

In analyzing arrays consisting of two orthogonal sets of dislocations relieving biaxial strain in an epilayer, it becomes necessary to consider the energy arising from interactions between dislocations at right angles to each other. This may be achieved by examining each component of the Burgers vector separately.

An edge dislocation at $x_1 = h$ lying parallel to the x_3 axis on a slip plane which is at an angle φ relative to the free surface has $\sigma_{13} = \sigma_{31} = \sigma_{23} = \sigma_{32} = 0$. There is therefore no interaction between it and an edge dislocation with its Burgers vector perpendicular to the free surface, lying parallel to the x_2 axis, brought into place at $x_1 = h$. Similarly, there is no interaction between the edge dislocation lying parallel to the x_3 axis and a screw dislocation lying parallel to the x_2 axis brought to $x_1 = h$. Thus there are no contributions from interactions among these components to $E'_{int,disl/disl}$.

An array A of identical screw dislocations of spacing d lying parallel to the x_3 axis interacts with an array B of identical screw dislocations lying parallel to the x_2 axis through the terms e_{23} and e_{32}, which, as pointed out by Willis *et al.* (1990), may be thought of as the sum of an average strain and a periodically fluctuating strain having a mean value of zero. The fluctuating strains of array A have no net interaction with the strain field of array B, and vice versa. Thus the only interaction between the arrays arises from the average strain of each array. Now array A imparts an average shear strain of magnitude $|e_{23_{avg}}| = |e_{32_{avg}}| = \frac{b}{2d}$ to the thin epilayer. If the array B is of opposite sign, a pure twist boundary is formed; the net value of $e_{23_{avg}}$ in the epilayer is then zero. Since for each array considered on its own we have a strain energy density due to $e_{23_{avg}}$ of $2\mu e^2_{23_{avg}} = \frac{\mu b^2}{2d^2}$, the interaction energy per unit area of the orthogonal arrays of screw dislocations is $-\frac{\mu b^2 h}{d^2}$. Therefore the interaction energy per unit area between such arrays is

$$E'_{int,disl/disl} = \pm \frac{\mu b^2 h}{d^2}, \qquad (3.1.41)$$

depending on the relative signs of the arrays. If the sign of the screw dislocations alternates along the length of each array, there is no interaction between the two arrays of dislocations.

In the case of two orthogonal arrays of edge dislocations with their Burgers vectors parallel to the free surface, we have

$$E'_{int,disl/disl} = \lim_{L\to\infty} \frac{1}{L^2}\int_V \sigma^A_{ij}\, e^B_{ij} dv, \qquad (3.1.42)$$

where L is measured along the x_1, x_2 and x_3 axes. σ^A_{ij} are the stresses associated with the array of dislocations lying parallel to the x_2 axis, and e^B_{ij} are the strains associated with the array of dislocations lying parallel to the x_3 axis. Since $e^B_{33} = 0$, $\sigma^A_{12} = \sigma^A_{21} = 0$, $e^B_{13} = e^B_{31} = 0$, $\sigma^A_{23} = \sigma^A_{32} = 0$,

$$E'_{int,disl/disl} = \lim_{L\to\infty}\left[\frac{1}{L^2}\int_V \sigma^A_{11} e^B_{11} dv + \frac{1}{L^2}\int_V \sigma^A_{22} e^B_{22} dv\right]$$

$$= \lim_{L\to\infty}\left[L\overline{\sigma^A_{11} e^B_{11}} + \frac{1}{L^2}\int_V \sigma^A_{22} e^B_{22} dv\right],$$

where $\overline{\sigma^A_{11} e^B_{11}}$ is the average value of $\sigma^A_{11} e^B_{11}$ in the epilayer. Therefore

$$E'_{int,disl/disl} = \lim_{L\to\infty} \frac{1}{L^2}\int_V \sigma^A_{22} e^B_{22} dv, \qquad (3.1.43)$$

because the average value of σ^A_{11} is $\overline{\sigma^A_{11}} = 0$ (this is shown in the appendix). Then

$$E'_{int,disl/disl} = \lim_{L\to\infty}\left[\frac{h}{L^2}\int_{-\frac{L}{2}}^{\frac{L}{2}}\int_{-\frac{L}{2}}^{\frac{L}{2}} \sigma^A_{22} e^B_{22} dx_2 dx_3\right], \qquad (3.1.44)$$

for the integration of e^B_{22} over the x_2x_3 plane yields a result which is a constant for $0 < x_1 < h$ and zero for $x_1 > h$. Thus

$$E'_{int,disl/disl} = \lim_{L\to\infty}\left[\frac{h}{L^2}\int_{-\frac{L}{2}}^{\frac{L}{2}}\int_{-\frac{L}{2}}^{\frac{L}{2}}\nu(\sigma_{11}^{A}+\sigma_{33}^{B})e_{22}^{B}dx_2dx_3\right]$$

$$= h\cdot\overline{\nu(\sigma_{11}^{A}+\sigma_{33}^{A})e_{22}^{B}}$$

$$= h\cdot\frac{2\mu\nu}{(1-\nu)}\overline{e_{33}^{A}e_{22}^{B}}$$

$$= \frac{2\mu\nu b^2 h}{(1-\nu)d^2} \qquad (3.1.45)$$

is the interaction energy per unit area between orthogonal sets of edge dislocations with their Burgers vectors parallel to the free surface.

B) Mixed Dislocations of Similar Orientation

Orthogonal arrays of mixed dislocations of similar orientation relieving biaxial strain in an epilayer give rise to a total elastic energy per unit area of

$$E_{total} = \frac{2\mu(1+\nu)f^2h}{(1-\nu)} + \frac{2}{d}\left[\frac{\mu b^2(1-\nu\cos^2\beta)}{4\pi(1-\nu)}\ln\left(\frac{2h}{r_0}\right)\right.$$

$$\left. + \frac{\mu b^2\sin^2\beta(\cos^2\varphi - \sin^2\varphi)}{8\pi(1-\nu)} + U_{core}\right]$$

$$- \frac{4\mu(1+\nu)|f|hb\sin\beta\cos\varphi}{(1-\nu)d} + \frac{\mu b^2(1-\nu\cos^2\beta)}{2\pi(1-\nu)d}\ln\left[\frac{d}{2\pi h}\sinh\left(\frac{2\pi h}{d}\right)\right]$$

$$+ \frac{\mu b^2\sin^2\beta\cos^2\varphi}{2\pi(1-\nu)d}\left[\frac{2\pi h}{d}\coth\left(\frac{2\pi h}{d}\right) - \frac{2\pi^2h^2}{d^2}\operatorname{csch}^2\left(\frac{2\pi h}{d}\right) - \frac{1}{2}\right]$$

$$- \frac{\mu b^2\sin^2\beta\sin^2\varphi}{2\pi(1-\nu)d}\left[\frac{2\pi h}{d}\coth\left(\frac{2\pi h}{d}\right) + \frac{2\pi^2h^2}{d^2}\operatorname{csch}^2\left(\frac{2\pi h}{d}\right) - \frac{3}{2}\right]$$

$$+ \frac{2\mu\nu hb^2\sin^2\beta\cos^2\varphi}{(1-\nu)d^2} \pm \frac{\mu hb^2\cos^2\beta}{d^2}, \quad h>r_0,\ d>2r_0, \tag{3.1.46}$$

with the sign of the last term depending on the relative signs of the orthogonal screw dislocations. The equilibrium spacing in the limit $h \to \infty$ is

$$\lim_{h\to\infty} d = \frac{((1-\nu)\cos^2\beta+(1+\nu)\sin^2\beta\cos^2\varphi)b}{(1+\nu)|f|\sin\beta\cos\varphi} \tag{3.1.47}$$

for orthogonal screw components which have a positive interaction energy, and

$$\lim_{h\to\infty} d = \frac{b\sin\beta\cos\varphi}{|f|} \tag{3.1.48}$$

for orthogonal screw components which have a negative interaction energy. When $\beta = \frac{\pi}{2}$, in both cases $\lim_{h\to\infty} d = \frac{b\cos\varphi}{|f|}$.

C) Mixed Dislocations of Alternating Orientation

In the case of misfit strain in the epilayer being relieved by mixed dislocations whose components which do not relieve misfit strain alternate along the length of the array, the total elastic energy per unit area is

$$E_{total} = \frac{2\mu(1+\nu)f^2h}{(1-\nu)} + \frac{2}{d}\left[\frac{\mu b^2(1-\nu\cos^2\beta)}{4\pi(1-\nu)}\ln\left(\frac{2h}{r_0}\right) + \frac{\mu b^2\sin^2\beta(\cos^2\varphi - \sin^2\varphi)}{8\pi(1-\nu)} + U_{core}\right]$$

$$- \frac{4\mu(1+\nu)|f|hb\sin\beta\cos\varphi}{(1-\nu)d}$$

$$+ \frac{\mu b^2\sin^2\beta\cos^2\varphi}{2\pi(1-\nu)d}\left[\ln\left(\frac{d}{2\pi h}\sinh\left(\frac{2\pi h}{d}\right)\right) + \frac{2\pi h}{d}\coth\left(\frac{2\pi h}{d}\right) - \frac{2\pi^2h^2}{d^2}\operatorname{csch}^2\left(\frac{2\pi h}{d}\right) - \frac{1}{2}\right]$$

$$+ \frac{\mu b^2\sin^2\beta\sin^2\varphi}{2\pi(1-\nu)d}\left[\ln\left(\frac{d}{\pi h}\tanh\left(\frac{\pi h}{d}\right)\right) + \frac{\pi h}{d}\left(\tanh\left(\frac{\pi h}{d}\right) - \coth\left(\frac{\pi h}{d}\right)\right) - \frac{\pi^2h^2}{2d^2}\left(\operatorname{sech}^2\left(\frac{\pi h}{d}\right) + \operatorname{csch}^2\left(\frac{\pi h}{d}\right)\right) + \frac{3}{2}\right]$$

$$+ \frac{\mu b^2\cos^2\beta}{2\pi d}\ln\left(\frac{d}{\pi h}\tanh\left(\frac{\pi h}{d}\right)\right) + \frac{2\mu\nu hb^2\sin^2\beta\cos^2\varphi}{(1-\nu)d^2}, \quad h>r_0,\ d>2r_0. \qquad (3.1.49)$$

Solving for the equilibrium dislocation spacing in the limit $h \to \infty$ as before, gives

$$\lim_{h\to\infty} d = \frac{b\sin\beta\cos\varphi}{|f|} . \qquad (3.1.50)$$

3.1.6 Computations for Silicon–Germanium Strained Layers Grown on Si(100)

A) Critical Thickness

Values of the critical thickness for 60° and edge dislocations in $Si_{1-x}Ge_x$ grown on Si may be obtained through equation (3.1.14) on the insertion of the appropriate parameters. This is the thickness at which it becomes energetically favourable to introduce a single dislocation to the substrate/epilayer interface. As Jain *et al.* (1992) have observed, the critical thickness depends on the type of array of dislocations present relieving strain in the epilayer; this point will be returned to shortly. In the calculation of the critical thickness, the magnitudes of the core energy and the cut–off radius are key quantities. Nandedkar and Narayan (1987, 1990) have studied the core structures of several types of dislocations in silicon and germanium using four different interatomic potentials. Here use is made of their core energies for the 90° $\frac{a}{2}$[110] dislocation (0.49 eV $Å^{-1}$) and the 60° $\frac{a}{2}$[110] dislocation (0.95 eV $Å^{-1}$) in silicon as calculated using the Stillinger–Weber potential. The core energies are not greatly changed if the dislocation sits at an Si–Ge interface (Nandedkar and Narayan, 1989). In both cases the cutoff radius is 5 Å. Since Vegard's law holds in Si–Ge alloys (Dismukes, Ekstrom and Paff 1964) the value of f is related to the amount of germanium in the epilayer through $f = 4.0\times10^{-2}x$, where x represents the fraction of germanium in the layer. Then setting $\mu = 6.81\times10^{10} N/m^2$ and $\nu = 0.218$ (Hirth and

Lothe 1982), and with $\beta = 90°$, $\varphi = 0°$ for the edge dislocation and $\beta = 60°$, $\varphi = 54.736°$ for the mixed dislocation, the results shown in fig. 3.3 are obtained. In this figure the solid curve represents the critical thickness for 90° (Lomer) dislocations, while the dashed curve corresponds to 60° mixed dislocations. The 60° dislocations have a core parameter of $\alpha = 6.49$ ($\alpha = 5.62$ if equation (3.1.15) is used) and a critical thickness of 385 Å at a composition of 10% Ge, as compared with a core parameter of $\alpha = 5.46$ ($\alpha = 4.56$ if equation (3.1.15) is used) and a critical thickness of 173 Å at 10% Ge in the case of 90° dislocations. Because of uncertainties in the value of the core energy and cut–off radius, the values of the critical thickness given here are not truly accurate to 1 Å. The calculation to the nearest angstrom is merely intended to illustrate relative changes in the critical thickness with variations in the core energy and Ge concentration. If the value of the core energy of the 90° dislocations is doubled, so that it assumes a non–physical value of 0.98 $eV\text{Å}^{-1}$, a core parameter of $\alpha = 11.77$ and a critical thickness of 202 Å at a 10% Ge concentration are obtained. This change in the critical thickness is only 17% of the actual value of 173 Å for 90° dislocations. It is therefore clear that the critical thickness is not a sensitive function of the core energy.

B) Equilibrium Dislocation Spacing

The method used in this thesis to arrive at the equilibrium spacing of a given array of dislocations relies on the calculation of interaction energies between the various sources of internal stress present in the strained layer system. If the interaction energy between a dislocation and the epilayer

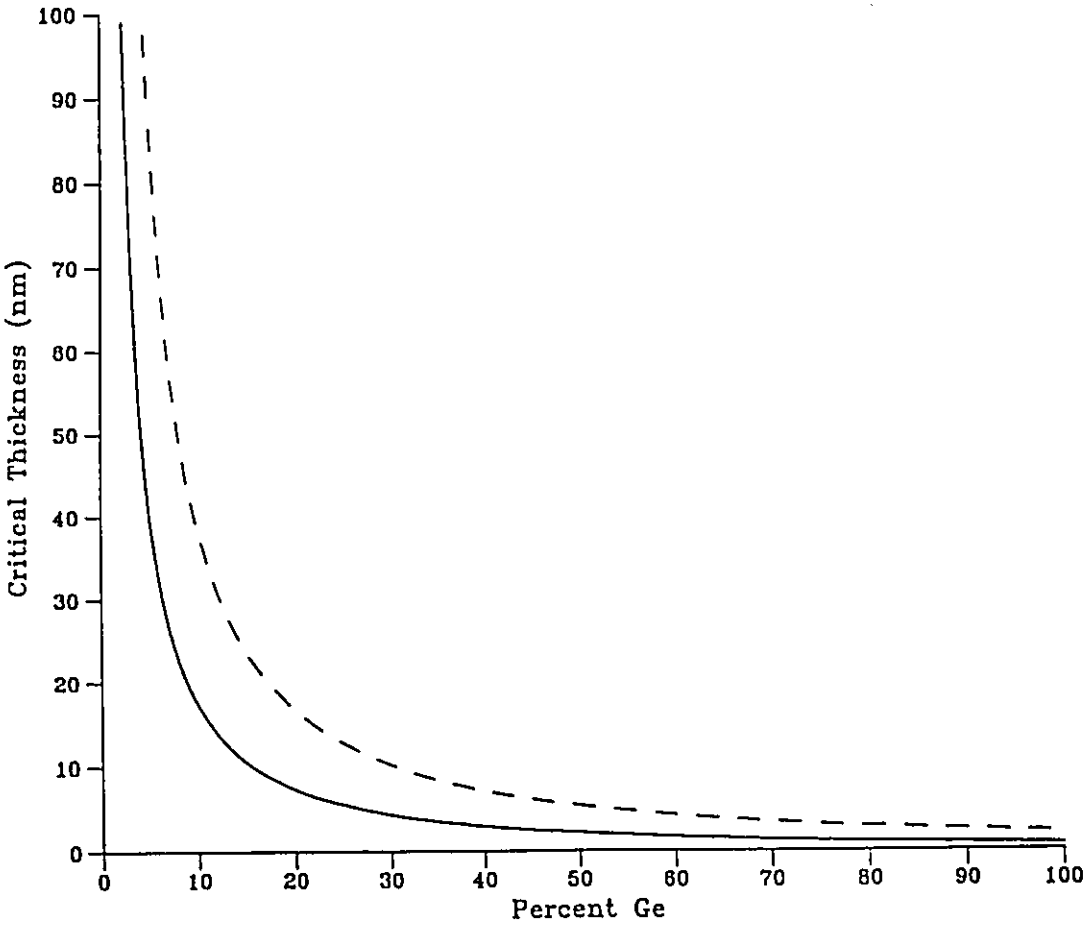

Figure 3.3: Critical thickness vs. percent Ge for 90° dislocations (solid curve) and 60° dislocations (dashed curve) in the case of Si–Ge deposited on Si(100).

exceeds the self energy of the dislocation, it becomes energetically favourable to introduce dislocations to the substrate/epilayer interface. The equilibrium spacing is determined by the form of the energy arising from interactions between the dislocations which make up the array. A knowledge of the nature of this interaction energy is essential, for without this term the elastic energy of the system continually decreases on the introduction of dislocations at thicknesses exceeding the critical thickness. Matthews (1975) was able to arrive at an equilibrium dislocation spacing through the creation of a term which plays the role of an effective interaction energy, although it has not generally been recognized as such. This is the quantity $\frac{2\mu(1+\nu)b^2h}{(1-\nu)d^2}$ associated with the elastic strain in the film. It stands separately from the self energy of the dislocations, and is not dissimilar from the terms in the present treatment arising from orthogonal dislocations making up a two–dimensional array.

Computed results for the spacing of 90° (Lomer) dislocations in an $Si_{0.9}Ge_{0.1}$ layer deposited on a Si(100) substrate are represented by the solid curve shown in fig. 3.4. Since there are no surface steps associated with these dislocations, the exactness of this solution (within the context of isotropic elasticity) is determined by the extent to which the value of the core energy is accurate. Also shown in fig. 3.4 is a dashed curve which corresponds to Matthew's approximate solution (1975). It is remarkable how closely the two curves match – the critical thickness for Matthew's approximation is 146 Å, while that of the present calculation is 173 Å.

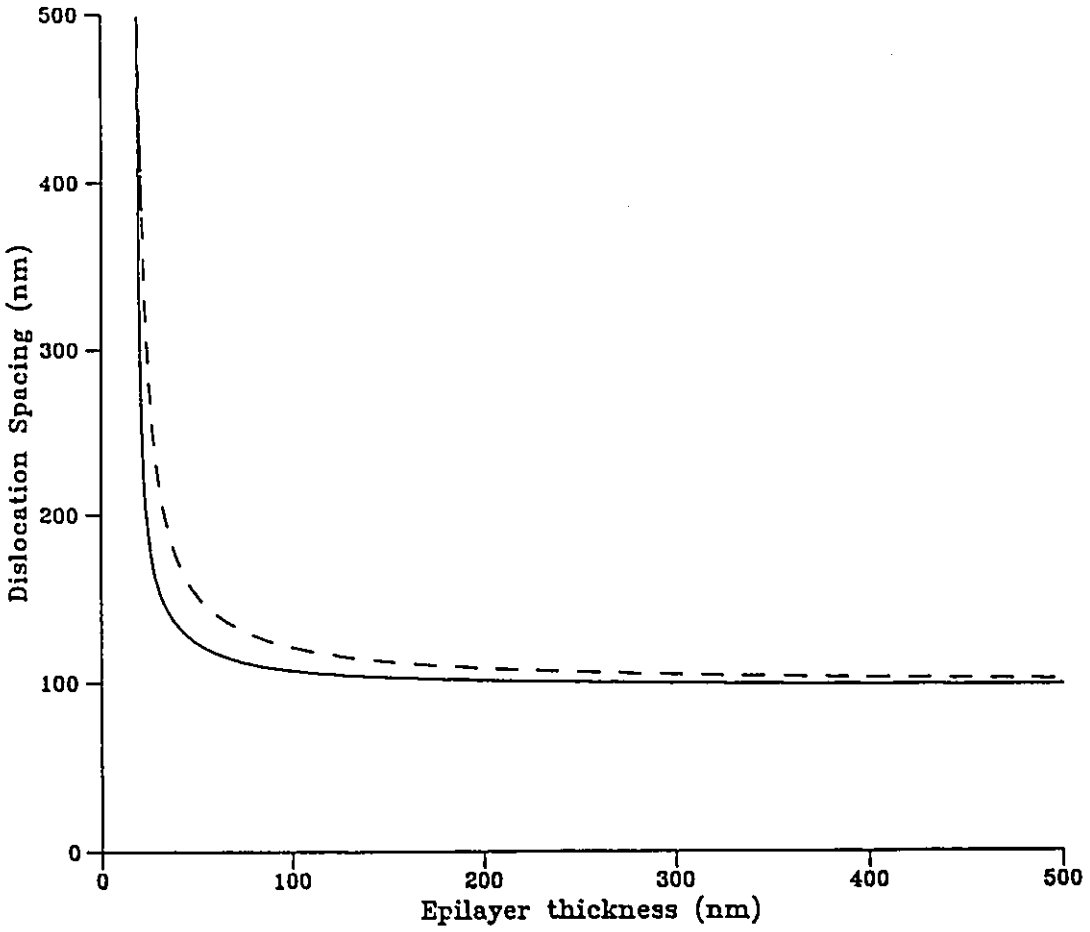

Figure 3.4: Dislocation spacing vs. epilayer thickness for 90° dislocations relieving strain in $Si_{0.9}Ge_{0.1}$ deposited on Si(100). The solid curve corresponds to the present work, while the dashed curve represents Matthew's approximation.

The results of computations carried out for 60° dislocations lying on {111} planes in an $Si_{0.9}Ge_{0.1}$ layer deposited on a Si(100) substrate are shown in fig. 3.5. There are three cases to distinguish: 60° dislocations of similar orientation whose orthogonal screw components give rise to a negative interaction energy (the lower solid curve), 60° dislocations of alternating orientation (the dashed curve), and 60° dislocations of similar orientation whose orthogonal screw components give rise to a positive interaction energy (the upper solid curve). It is interesting to compare the behaviour of the array of dislocations of similar orientation whose orthogonal screw components form a twist boundary with that of the array of dislocations of alternating orientation in the vicinity of the critical thickness associated with a single 60° dislocation. This cannot be seen in the graph shown in fig. 3.5, but may be seen in table 3.1, in which the dislocation spacing of the two arrays is shown at points just greater than the critical thickness. It may be seen that the spacing of the array of alternating dislocations becomes very large as the thickness approaches the critical thickness, while the array of similar dislocations does not become widely spaced. This is consistent with the findings of Jain *et al.* (1992) for this array – at its critical thickness, a finite number of dislocations are present in the epilayer. However, the critical thickness of the array of 60° dislocations of alternating orientation is apparently identical to that of a single 60° dislocation.

Both the dislocations of alternating orientation and the dislocations of similar orientation whose orthogonal screw components give rise to a negative

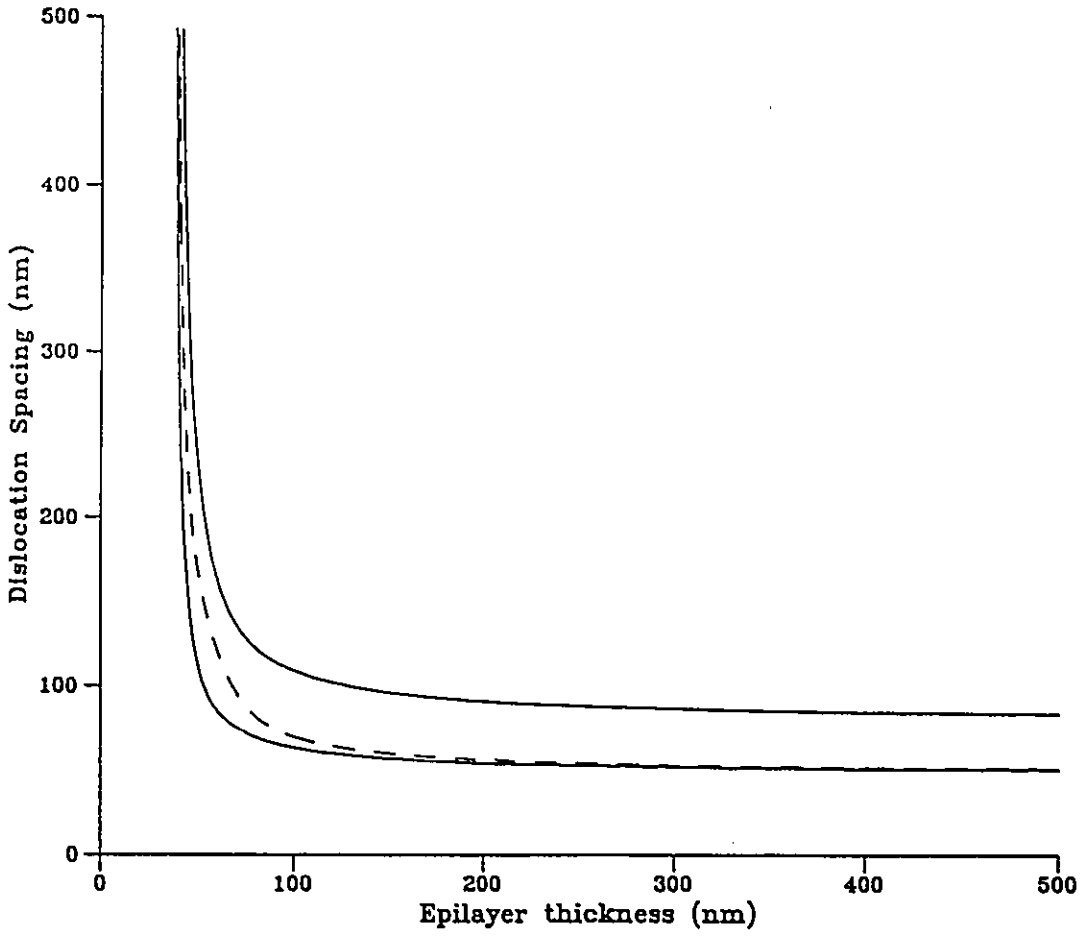

Figure 3.5: Dislocation spacing vs. epilayer thickness for 60° dislocations relieving strain in $Si_{0.9}Ge_{0.1}$ deposited on Si(100). Lower solid curve: dislocations of similar orientation whose screw components give rise to a negative interaction energy. Dashed curve: dislocations of alternating orientation. Upper solid curve: dislocations of similar orientation whose screw components give rise to a positive interaction energy.

Epilayer Thickness (nm)	Dislocation Spacing	
	Similar (nm)	Alternating (nm)
38.40091	818.987	8.783×10^{7}
38.40092	818.965	2.702×10^{7}
38.40093	818.943	1.596×10^{7}
38.40094	818.921	1.133×10^{7}
38.40095	818.898	8.780×10^{6}
38.40096	818.875	7.167×10^{6}
38.40097	818.854	6.055×10^{6}
38.40098	818.831	5.242×10^{6}
38.40099	818.809	4.621×10^{6}

Table 3.1: Equilibrium spacing of two–dimensional arrays of mixed dislocations in the vicinity of the critical thickness.

interaction energy approach the same spacing of $\frac{b}{2|f|}$ as h becomes large, but in the latter case the convergence is more rapid. The fact that orthogonal screw components can form a low energy twist boundary outweighs the greater dislocation–dislocation interaction energy associated with a one–dimensional array of dislocations of similar orientation. This may also be seen in a plot of the energies of these arrays. Figure 3.6 shows the energies (at equilibrium spacing) of an array of 60° dislocations having a similar orientation whose orthogonal screw components form a twist boundary (the solid curve) and of an array of 60° dislocations of alternating orientation (the dashed curve). It is clear that the array of alternating dislocations has the greater energy at all thicknesses.

The formation of a twist boundary requires the cooperative nucleation of a large number of dislocations, while an array much more like the set of dislocations of alternating orientation is produced by a random nucleation of dislocations. At 10% Ge, the equilibrium spacing at large thicknesses for the case of 60° dislocations whose screw components form a twist boundary corresponds to a lattice rotation of 0.23 degrees. This is difficult to detect by means of transmission electron microscopy, but could be observed using X–ray diffraction experiments. It is probable, however, that actual nucleation events are random, so that the spacing in a physical sample would closely approximate that given by the dashed curve in fig. 3.5, provided that kinetic barriers could be surmounted and equilibrium attained. In addition, the equilibrium critical thickness in a physical sample is likely to be that associated with a single 60° dislocation rather than the critical thickness

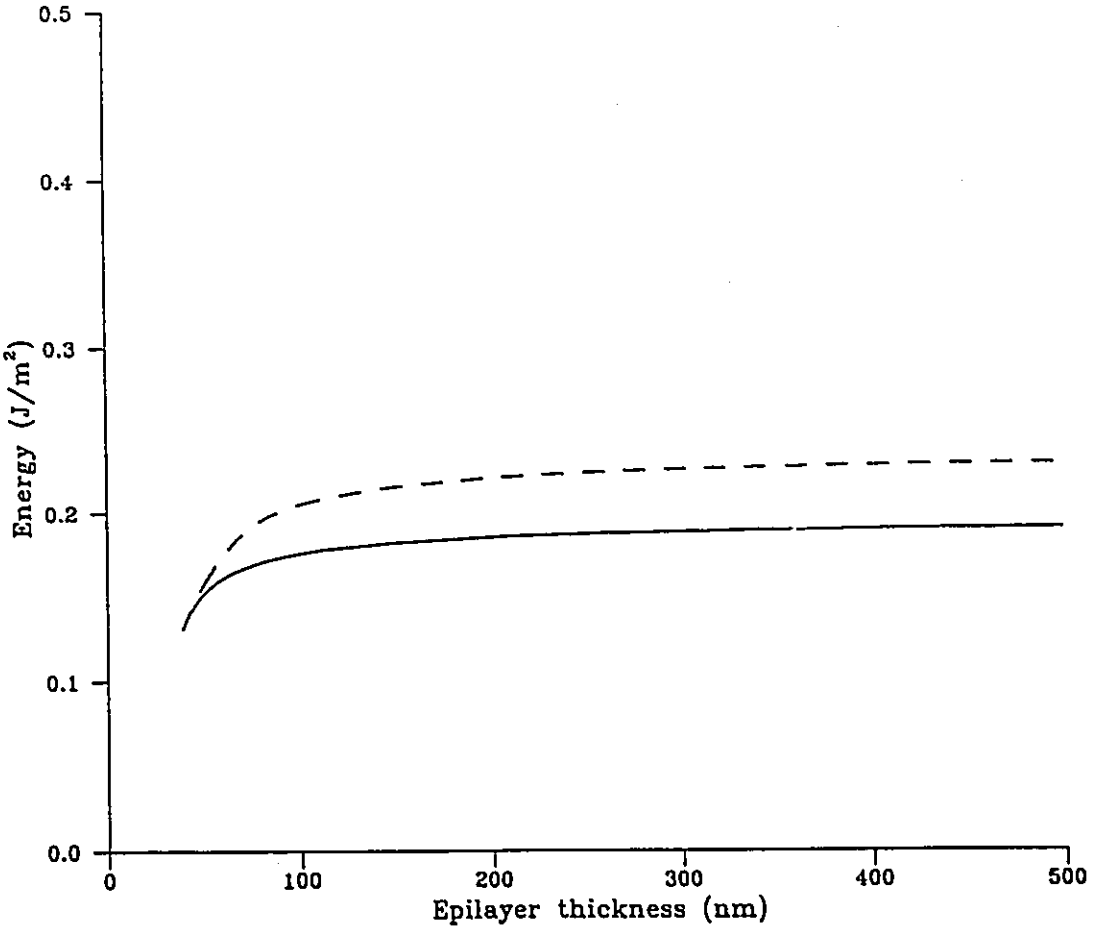

Figure 3.6: Energy at equilibrium spacing vs. epilayer thickness in $Si_{0.9}Ge_{0.1}$ deposited on Si(100) for 60° dislocations of similar orientation whose screw components give rise to a negative interaction energy (solid curve) and 60° dislocations of alternating orientation (dashed curve).

determined by Jain *et al.* (1992). However, since the difference between the two values of the critical thickness is so small, it could never be detected in practice.

3.2. Energies of Low Angle Grain Boundaries in a Half–Space

3.2.1. The Energy of an Array of Edge Dipoles

It is possible to use the method of section 3.1 in order to determine the energies of various types of low angle grain boundaries lying parallel to the free surface in a semi–infinite solid. Very often these boundaries are made up of dislocations which have one or more components alternating in sign along the length of the boundary, and it is therefore necessary to obtain expressions for the energies of one–dimensional planar array of dislocation dipoles. The energies of two of these arrays (screw and edge with Burgers vector perpendicular to the free surface) have been given in section 3.1.4 (they may be obtained from equation (3.1.37) plus the self energy of the dislocations in the array). Here an expression for the energy per unit area of an array of edge dipoles having their Burgers vectors parallel to the free surface is developed which may be used in calculating the energies of low angle grain boundaries in a half–space. Following the method of section 3.1.4, this energy may be written as

$$E = \frac{1}{d}\left[\frac{\mu b^2}{4\pi(1-\nu)}\ln\left(\left(\frac{2h}{r_0}\right) + \tfrac{1}{2}\right) + U_{core}\right]$$

$$+\frac{\mu b^2}{4\pi(1-\nu)d}\left[\ln\left[\prod_{n=1}^{\infty}\left(1+\frac{4h^2}{n^2d^2}\right)\right]+\sum_{n=1}^{\infty}\frac{12(2n)^2d^2h^2}{((2n)^2d^2+4h^2)^2}+\sum_{n=1}^{\infty}\frac{16h^4}{((2n)^2d^2+4h^2)^2}\right]$$

$$-\frac{\mu b^2}{4\pi(1-\nu)d}\left[\ln\left[\prod_{n=0}^{\infty}\left(1+\frac{4h^2}{(2n+1)^2d^2}\right)\right]+\sum_{n=0}^{\infty}\frac{12(2n+1)^2d^2h^2}{((2n+1)^2d^2+4h^2)^2}\right.$$

$$\left.+\sum_{n=0}^{\infty}\frac{16h^4}{((2n+1)^2d^2+4h^2)^2}\right], \qquad (3.2.1)$$

or, in closed form, (Hansen 1975)

$$E=\frac{1}{d}\left[\frac{\mu b^2}{4\pi(1-\nu)}\ln\left(\left(\frac{2h}{r_0}\right)+\tfrac{1}{2}\right)+U_{core}\right]$$

$$+\frac{\mu b^2}{4\pi(1-\nu)d}\left[\ln\left(\frac{d}{\pi h}\tanh\left(\frac{\pi h}{d}\right)\right)+\frac{\pi h}{d}\left(\coth\left(\frac{\pi h}{d}\right)-\tanh\left(\frac{\pi h}{d}\right)\right)\right.$$

$$\left.-\frac{\pi^2h^2}{2d^2}\left(\operatorname{sech}^2\left(\frac{\pi h}{d}\right)+\operatorname{csch}^2\left(\frac{\pi h}{d}\right)-\tfrac{1}{2}\right)\right], \quad h>r_0,\ d>2r_0. \qquad (3.2.2)$$

3.2.2. Tilt Boundary Energies

Consider the array of edge dislocations shown in fig. 3.7. Making use of the results of section 3.1.4 and the previous section, its energy may be written as

$$E=\frac{1}{d}\left[\frac{\mu b^2}{4\pi(1-\nu)}\ln\left(\frac{2h}{r_0}\right)+\frac{\mu b^2\sin^2\beta(\cos^2\varphi-\sin^2\varphi)}{8\pi(1-\nu)}+U_{core}\right]$$

Figure 3.7: Array of edge dislocations forming a tilt boundary lying parallel to the free surface in a semi–infinite solid.

$$+ \frac{\mu b^2 \sin^2\varphi}{4\pi(1-\nu)d}\left[\ln\left(\frac{d}{2\pi h}\sinh\left(\frac{2\pi h}{d}\right)\right) - \frac{2\pi h}{d}\coth\left(\frac{2\pi h}{d}\right) - \frac{2\pi^2 h^2}{d^2}\operatorname{csch}^2\left(\frac{2\pi h}{d}\right) + \tfrac{3}{2}\right]$$

$$+ \frac{\mu b^2 \cos^2\varphi}{4\pi(1-\nu)d}\left[\ln\left(\frac{d}{\pi h}\tanh\left(\frac{\pi h}{d}\right)\right) + \frac{\pi h}{d}\left(\coth\left(\frac{\pi h}{d}\right) - \tanh\left(\frac{\pi h}{d}\right)\right)\right.$$

$$\left. - \frac{\pi^2 h^2}{2d^2}\left(\operatorname{sech}^2\left(\frac{\pi h}{d}\right) + \operatorname{csch}^2\left(\frac{\pi h}{d}\right) - \tfrac{1}{2}\right)\right], \quad h>r_0,\ d>2r_0. \qquad (3.2.3)$$

In the limit $h \to \infty$, the energy becomes

$$E = \frac{\mu b^2 \sin^2\varphi}{4\pi(1-\nu)d}\left[\ln\left(\frac{d}{2\pi r_0}\right) + 1\right]$$

$$+ \frac{\mu b^2 \cos^2\varphi}{4\pi(1-\nu)d}\ln\left(\frac{2d}{\pi r_0}\right) + \frac{U_{core}}{d}, \quad h>r_0,\ d>2r_0. \qquad (3.2.4)$$

When φ is close to 90°, $\cos^2\varphi \cong 0$ and $\sin^2\varphi \cong 1$, giving

$$E = \frac{\mu b^2}{4\pi(1-\nu)d}\left[\ln\left(\frac{d}{2\pi r_0}\right) + 1\right] + \frac{U_{core}}{d}, \quad h>r_0,\ d>2r_0, \qquad (3.2.5)$$

which is a form of the Read–Shockley equation (Read and Shockley 1950).

There are geometrical restrictions imposed by a crystal lattice on a tilt boundary lying parallel to a free surface. In effect φ and d are not independent variables. Consider a simple cubic lattice with a surface normal of (100), a dislocation line direction of [001], and a Burgers vector of a[010]. If θ is the angle of misorientation between the two crystals, then

$\frac{\theta}{2} = \frac{\pi}{2} - \varphi$. Lattice geometry requires that

$$\frac{b}{2d} = \sin\frac{\theta}{2} = \sin(\frac{\pi}{2} - \varphi) = \cos\varphi, \qquad (3.2.6)$$

and therefore that

$$\cos^2\varphi = \frac{b^2}{4d^2}\ ; \quad \sin^2\varphi = 1 - \frac{b^2}{4d^2}\ . \qquad (3.2.7)$$

In the case of the fcc/diamond cubic lattice, if the surface normal is (100) before the formation of the boundary, a tilt boundary can be constructed from 60° $\frac{a}{2}\langle 110\rangle$ dislocations (assumed here to be undissociated) in which edge components having their Burgers vectors parallel to the free surface and screw components alternating in sign along the length of the array as shown in fig. 3.8. Lattice geometry requires that for an angular misorientation of θ between the two crystals

$$\theta = \frac{b\sin\varphi_0}{d}\ ; \quad \varphi = \varphi_0 \pm \frac{\theta}{2}\ , \qquad (3.2.8)$$

where φ is the angle that the slip plane of the dislocations makes with the free surface before the boundary is formed and φ is the corresponding angle after the boundary is formed. For small θ, $\varphi \cong \varphi_0$, and the energy per unit area of the boundary may be written as

$$E = \frac{1}{d}\left[\frac{\mu b^2(1-\nu\cos^2\beta)}{4\pi(1-\nu)}\ln(\frac{2h}{r_0}) + \frac{\mu b^2\sin^2\beta(\cos^2\varphi - \sin^2\varphi)}{8\pi(1-\nu)} + U_{core}\right]$$

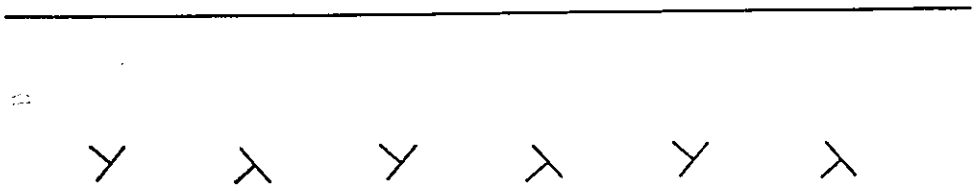

Figure 3.8: Illustration of a tilt boundary in a semi–infinite fcc/diamond cubic lattice; surface normal = (100).

$$+ \frac{\mu b^2 \sin^2\beta \sin^2\varphi}{4\pi(1-\nu)d}\left[\ln\left(\frac{d}{2\pi h}\sinh\left(\frac{2\pi h}{d}\right)\right) - \frac{2\pi h}{d}\coth\left(\frac{2\pi h}{d}\right) - \frac{2\pi^2 h^2}{d^2}\operatorname{csch}^2\left(\frac{2\pi h}{d}\right) + \tfrac{3}{2}\right]$$

$$+ \frac{\mu b^2 \sin^2\beta \cos^2\varphi}{4\pi(1-\nu)d}\left[\ln\left(\frac{d}{\pi h}\tanh\left(\frac{\pi h}{d}\right)\right) + \frac{\pi h}{d}\left(\coth\left(\frac{\pi h}{d}\right) - \tanh\left(\frac{\pi h}{d}\right)\right)\right.$$

$$\left. - \frac{\pi^2 h^2}{2d^2}\left(\operatorname{sech}^2\left(\frac{\pi h}{d}\right) + \operatorname{csch}^2\left(\frac{\pi h}{d}\right) - \tfrac{1}{2}\right)\right]$$

$$+ \frac{\mu b^2 \cos^2\beta}{4\pi d}\ln\left(\frac{d}{\pi h}\tanh\left(\frac{\pi h}{d}\right)\right), \quad h>r_0,\ d>2r_0. \tag{3.2.9}$$

In the limit $h \to \infty$, the energy per unit area becomes

$$E = \frac{\mu b^2 \sin^2\beta \sin^2\varphi}{4\pi(1-\nu)d}\left[\ln\left(\frac{d}{2\pi r_0}\right) + 1\right] + \frac{\mu b^2 \sin^2\beta \cos^2\varphi}{4\pi(1-\nu)d}\ln\left(\frac{2d}{\pi r_0}\right)$$

$$+ \frac{\mu b^2 \cos^2\beta}{4\pi d}\ln\left(\frac{2d}{\pi r_0}\right) + \frac{U_{core}}{d}, \quad h>r_0,\ d>2r_0. \tag{3.2.10}$$

Note that in this limit (which gives the energy of the boundary in an infinite crystal), the energy associated with the alternating components varies as $\ln(\frac{2d}{\pi r_0})$ rather than $\ln(\frac{d}{2\pi r_0})$. Read and Shockley (1950) obtained this result when analyzing an array of alternating screw dislocations, but not the corresponding result for an array of edge dislocations.

If in an fcc or diamond cubic material the surface normal is $(11\bar{2})$, the (111) planes are perpendicular to the surface and the energy per unit area of the tilt boundary (taking $\sin^2\varphi \cong 1$) is

$$E = \frac{1}{d}\left[\frac{\mu b^2(1-\nu\cos^2\beta)}{4\pi(1-\nu)}\ln(\frac{2h}{r_0}) + \frac{\mu b^2\sin^2\beta}{8\pi(1-\nu)} + U_{core}\right]$$

$$+ \frac{\mu b^2\sin^2\beta}{4\pi(1-\nu)d}\left[\ln(\frac{d}{2\pi h}\sinh(\frac{2\pi h}{d})) - \frac{2\pi h}{d}\coth(\frac{2\pi h}{d}) - \frac{2\pi^2 h^2}{d^2}\operatorname{csch}^2(\frac{2\pi h}{d}) + \frac{3}{2}\right]$$

$$+ \frac{\mu b^2\cos^2\beta}{4\pi d}\ln(\frac{d}{\pi h}\tanh(\frac{\pi h}{d})), \quad h>r_0,\ d>2r_0. \tag{3.2.11}$$

In the limit $h \to \infty$, the energy becomes

$$E = \frac{\mu b^2\sin^2\beta}{4\pi(1-\nu)d}\left[\ln(\frac{d}{2\pi r_0}) + 1\right] + \frac{\mu b^2\cos^2\beta}{4\pi d}\ln(\frac{2d}{\pi r_0})$$

$$+ \frac{U_{core}}{d}, \quad h>r_0,\ d>2r_0. \tag{3.2.12}$$

3.2.3 Twist Boundary Energies

The summation of dislocation–pair energies may also be used to give the energies of twist boundaries lying parallel to the free surface. Two cases are given here. For a simple cubic lattice with a surface normal of (100) and a Burgers vector of the type a⟨100⟩,

$$E = \frac{2}{d}\left[\frac{\mu b^2}{4\pi}\ln(\frac{2h}{r_0}) + U_{core}\right]$$

$$+ \frac{\mu b^2}{2\pi d}\left[\ln(\frac{d}{2\pi h}\sinh(\frac{2\pi h}{d}))\right] - \frac{\mu b^2 h}{d^2}, \quad h>r_0,\ d>2r_0 \tag{3.2.13}$$

For an fcc or diamond cubic lattice with a surface normal of (100), a twist boundary lying parallel to the free surface made up of undissociated $\frac{a}{2}\langle 110\rangle$ dislocations has edge components in a parallel set of dislocations alternating in sign. The energy of the boundary per unit area is

$$E = \frac{2}{d}\left[\frac{\mu b^2(1-\nu\cos^2\beta)}{4\pi(1-\nu)}\ln(\frac{2h}{r_0}) + \frac{\mu b^2\sin^2\beta(\cos^2\varphi - \sin^2\varphi)}{8\pi(1-\nu)} + U_{core}\right]$$

$$+ \frac{\mu b^2\sin^2\beta\sin^2\varphi}{2\pi(1-\nu)d}\left[\ln(\frac{d}{\pi h}\tanh(\frac{\pi h}{d})) + \frac{\pi h}{d}(\tanh(\frac{\pi h}{d}) - \coth(\frac{\pi h}{d}))\right.$$

$$\left. - \frac{\pi^2 h^2}{2d^2}(\operatorname{sech}^2(\frac{\pi h}{d}) + \operatorname{csch}^2(\frac{\pi h}{d})) + \tfrac{3}{2}\right]$$

$$+ \frac{\mu b^2\sin^2\beta\cos^2\varphi}{2\pi(1-\nu)d}\left[\ln(\frac{d}{\pi h}\tanh(\frac{\pi h}{d})) + \frac{\pi h}{d}(\coth(\frac{\pi h}{d}) - \tanh(\frac{\pi h}{d}))\right.$$

$$\left. - \frac{\pi^2 h^2}{2d^2}(\operatorname{sech}^2(\frac{\pi h}{d}) + \operatorname{csch}^2(\frac{\pi h}{d}) - \tfrac{1}{2})\right]$$

$$+ \frac{\mu b^2\cos^2\beta}{2\pi d}\ln(\frac{d}{2\pi h}\sinh(\frac{2\pi h}{d})) - \frac{\mu b^2\cos^2\beta}{d^2}, \quad h>r_0,\ d>2r_0. \tag{3.2.14}$$

In the limit $h \to \infty$,

$$E = \frac{\mu b^2\sin^2\beta}{2\pi(1-\nu)d}\left[\ln(\frac{2d}{\pi r_0}) + \sin^2\varphi\right]$$

$$+ \frac{\mu b^2\cos^2\beta}{2\pi d}\ln(\frac{d}{2\pi r_0}) + \frac{2U_{core}}{d}, \quad h>r_0,\ d>2r_0. \tag{3.2.15}$$

CHAPTER 4

Experimental Procedure

Silicon–germanium strained layers were deposited on 100 mm Czochralski–grown Si(100) substrates using a Vacuum Generators V80 MBE system at NRC in Ottawa. The substrates were given an ozone exposure in an *ex situ* reactor for approximately 45 minutes in order to remove hydrocarbon contamination immediately before introduction to the vacuum system. Oxide removal was carried out in the MBE system by heating the wafers to 900°C in a silicon flux.

Two short period superlattices were grown at a substrate temperature of 400°C. The first was a 48–period structure in which 2 monolayers of Ge alternated with 6.6 monolayers of Si ($(Si_{6.6}Ge_{2.0})_{48}$), while the second was a 24–period structure in which 3.7 monolayers of Ge alternated with 9.3 monolayers of Si ($(Si_{9.3}Ge_{3.7})_{24}$). The data concerning the layer thicknesses given here were obtained using double crystal X–ray diffraction. Both superlattices were grown on a thick buffer layer and were capped with a 50 Å layer of Si. In addition, two homogeneous epilayers were grown at a substrate temperature of 525°C. One had the composition $Si_{0.8}Ge_{0.2}$ and was 1000 Å thick, while the other had the composition $Si_{0.7}Ge_{0.3}$ and was 500 Å thick. Once grown, the wafers were removed from the MBE chamber and sectioned

for annealing in a Heatpulse 410 rapid thermal annealer. The short period superlattices were annealed for 20 seconds at 450 and 500°C, and the homogeneous epilayers for 20 seconds at 600°C. Cross–sectional specimens with [110] foil normals and plan view specimens were prepared by mechanical thinning followed by Ar ion milling. These were examined in a Philips CM 12 operating at 120 kV. The results of the microscopy (showing the behaviour of dislocation sources in these specimens) may be found in chapter 5.

An 8–period strained layer superlattice consisting of 7.0 monolayers of Ge alternating with 17.5 monolayers of Si ($(Si_{17.5}Ge_{7.0})_8$) and capped with a 50 Å layer of Si was also grown at a substrate temperature of 400°C. Again, the layer thicknesses were obtained using double crystal X–ray diffraction measurements. After growth had been completed, the wafer was removed from the MBE chamber and sectioned for annealing. Four rapid thermal annealing treatments were performed in a Heatpulse 410 rapid thermal annealer: 20 s at 700°C, 200 s at 700°C, 2000 s at 700°C, and 300 s at 800°C. Cross–sectional specimens with [110] foil normals and plan view specimens were prepared by mechanical thinning followed by Ar ion milling, and were examined in a Philips CM 12 at 120 kV in order to determine the means by which the relaxation of the superlattice took place. The results (showing relaxation occurring exclusively via twin formation) are presented in chapter 6.

Two $Si_{1-x}Ge_x/Si$ strained layer superlattices, one a 20–period structure of Si layers 900 Å thick alternating with $Si_{0.76}Ge_{0.24}$ layers 500 Å thick, and the other a 20–period structure of Si layers 500 Å thick alternating with $Si_{0.65}Ge_{0.35}$ layers 100 Å thick, were grown at a substrate temperature

between 400 and 500°C at a rate of approximately 5 $Å s^{-1}$. Cross–sectional samples having [110] foil normals were prepared using the method previously described, and were again examined in a Philips CM 12 at 120 kV. The results of these experiments may be found in chapter 7, which deals with pagoda defects.

CHAPTER 5

Dislocation Sources in Si–Ge Strained Layer Structures

The production of electronic devices based on strained layer structures requires that the presence of misfit dislocations in the epilayer be kept to a minimum, if not altogether eliminated, and there has therefore been a large amount of research into the mechanisms by which the nucleation of such dislocations takes place. The essential finding has been that while homogeneous nucleation is an improbable occurrence (Matthews, Blakeslee, and Mader 1976), a variety of heterogeneous nucleation sources are possible and have been observed. These include the heterogeneous nucleation of half–loops at the free surface of the epilayer (Perovic, Weatherly and Houghton 1990), the nucleation of half–loops at defects at the edges of the sample (De Cooman and Carter 1989), the extension of threading dislocations introduced during growth (Matthews and Blakeslee 1974), the nucleation of loops at defects in the epilayer (Perovic *et al.* 1989), and the nucleation of loops at a regenerative internal source (Eaglesham *et al.* 1989). Here a new type of dislocation source in Si–Ge strained layer structures is reported. It is shown that the relaxation behaviour of short period superlattices is different from homogeneous epilayers of the same average Ge concentration, and that the relief of strain in these superlattices can take place at relatively low temperatures.

Two short period superlattices ($(Si_{9.3}Ge_{3.7})_{24}$ and $(Si_{6.6}Ge_{2.0})_{48}$) and two homogeneous epilayers (1000 Å of $Si_{0.8}Ge_{0.2}$ and 500 Å of $Si_{0.7}Ge_{0.3}$) having approximately the same effective stress acting on misfit dislocations as the superlattices were prepared for examination as described in the experimental procedure. The critical thicknesses of the strained layer structures as calculated from equation (3.1.22) using $\alpha = 6.49$ are: $(Si_{9.3}Ge_{3.7})_{24}$, 121 Å; $(Si_{6.6}Ge_{2.0})_{48}$, 158 Å; $Si_{0.8}Ge_{0.2}$, 167 Å; and $Si_{0.7}Ge_{0.3}$, 102 Å. Baribeau *et al.* (1991) have studied the as–grown structures of the two superlattices examined here along with four other superlattices using glancing incidence X–ray reflection, Raman scattering spectroscopy and EXAFS.

Cross–sectional micrographs of the two superlattices in the as–grown state are shown in fig. 5.1. The layers in the $(Si_{9.3}Ge_{3.7})_{24}$ superlattice are distinctly less planar than the layers in the $(Si_{6.6}Ge_{2.0})_{48}$ superlattice; this is due to the tendency toward the formation of islands in layers which are 3–4 monolayers of Ge in thickness grown on Si(100) (Mo *et al.* 1990; Williams *et al.* 1991). Transmission electron microscopy did not reveal any dislocations in either of these superlattices in the as–grown state. However, annealed material examined using transmission electron microscopy showed the presence of misfit dislocations which had clear points of origin. The $(Si_{9.3}Ge_{3.7})_{24}$ superlattice was the more unstable of the two; after annealing for 20 s at 500°C a well defined dislocation network (seen in fig. 5.2) had already developed in which dislocation sources were difficult to spot. However, as shown in figs. 5.3 and 5.4, annealing for 20 s at 450°C revealed clear dislocation sources in this material. It may be seen from fig. 5.3 that there

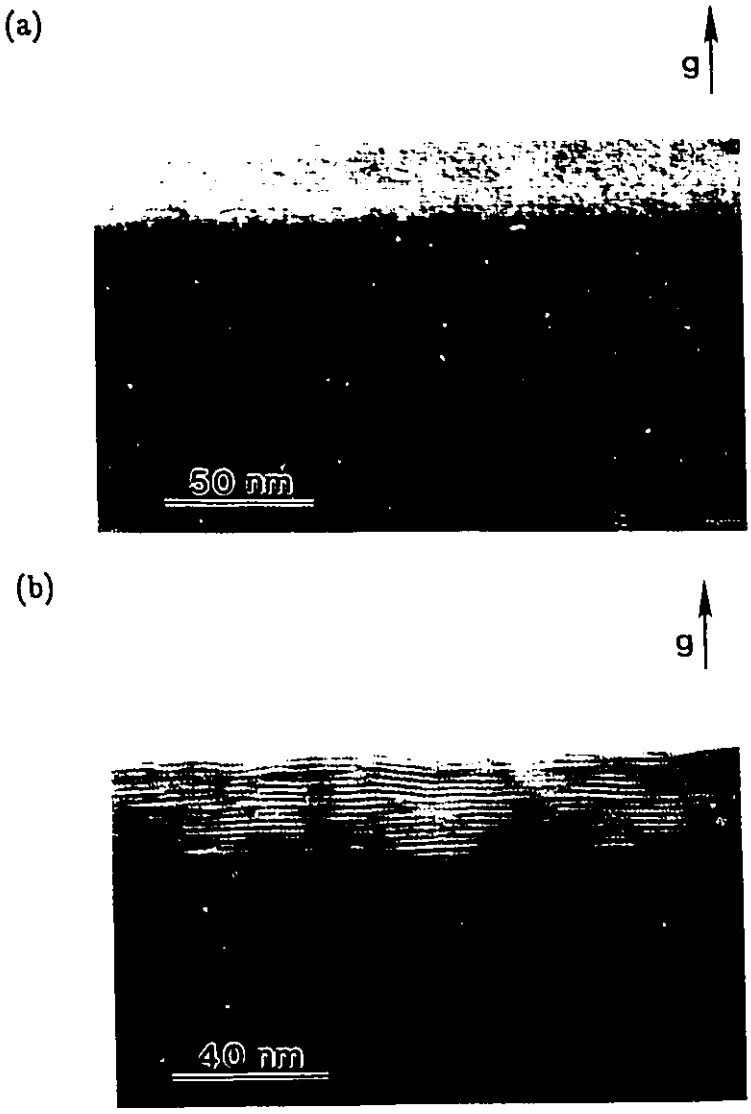

Figure 5.1: Cross–sectional micrographs of as–grown $(Si_mGe_n)_p$ superlattices: (a) $(Si_{6.6}Ge_{2.0})_{48}$, (b) $(Si_{9.3}Ge_{3.7})_{24}$. g = 400.

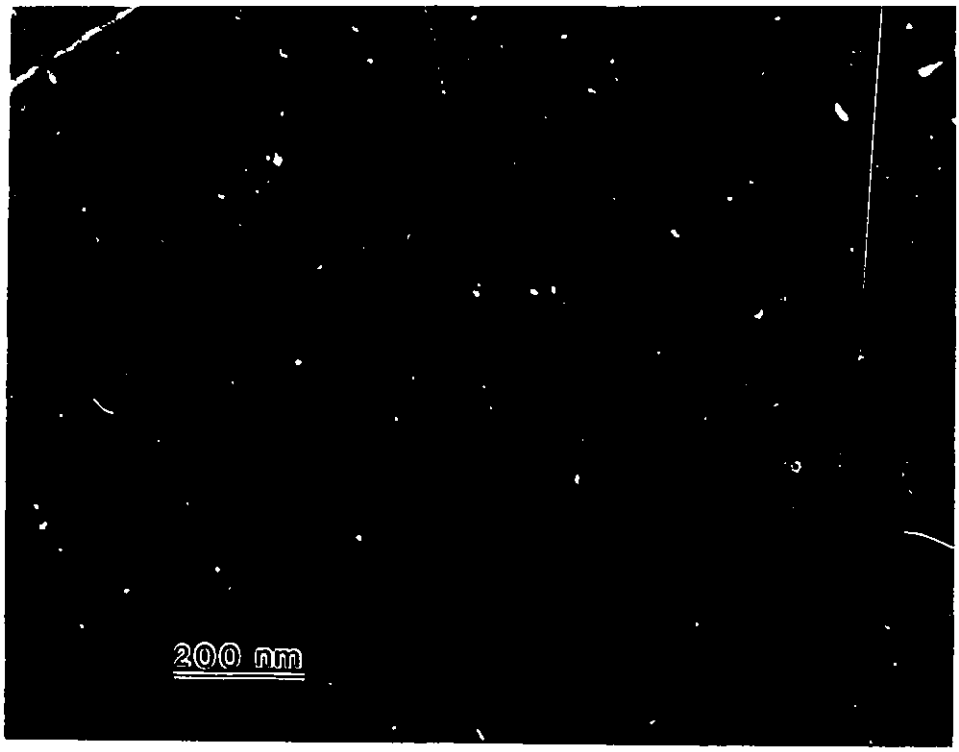

Figure 5.2: Plan view micrograph of dislocation network in $(Si_{9.3}Ge_{3.7})_{24}$ superlattice formed on annealing for 20 s at 500° C. Foil buckling causes the image of the network to have a varying intensity. g = 022 dark field.

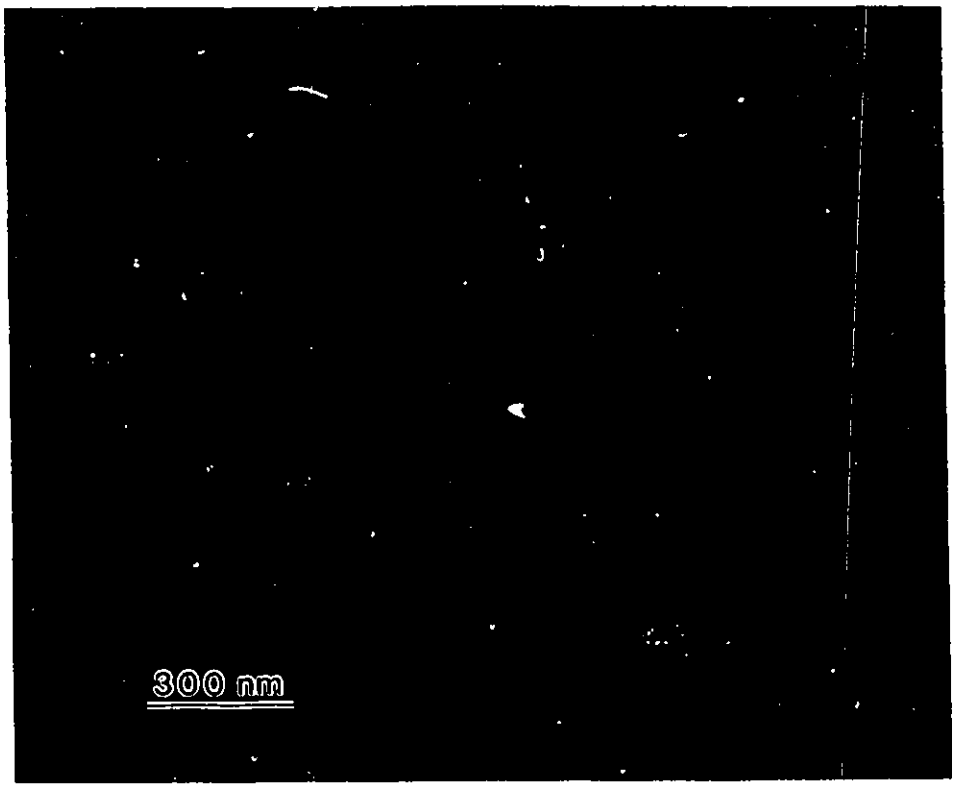

Figure 5.3: Plan view micrograph of dislocation source in $(Si_{9.3}Ge_{3.7})_{24}$ superlattice annealed 20 s at 450° C. g = 022 dark field, s>>0.

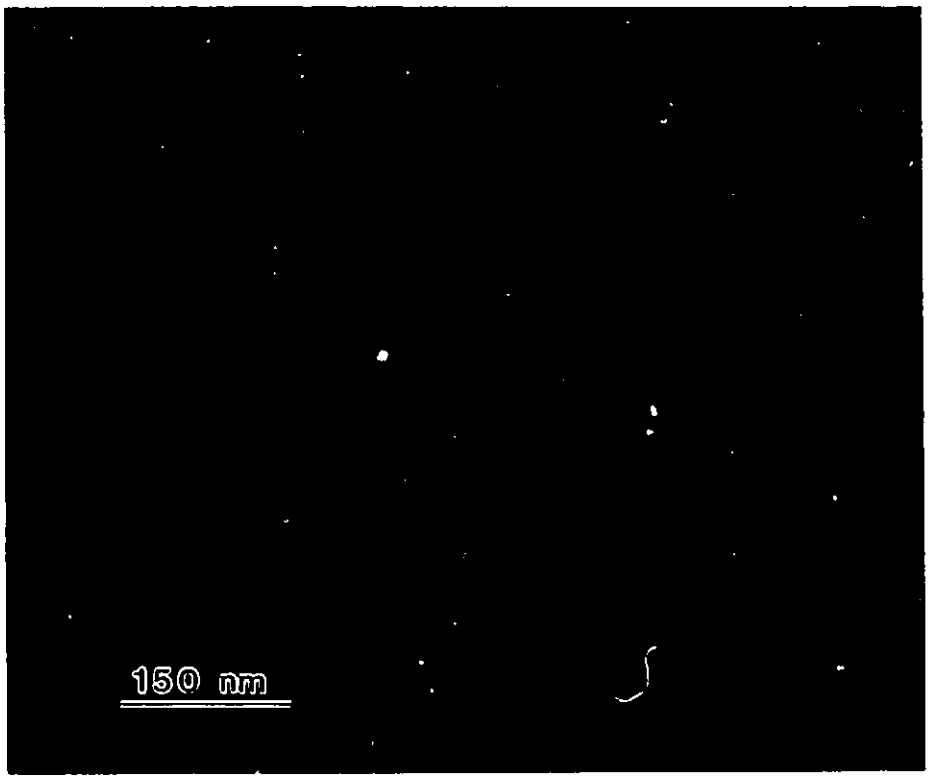

Figure 5.4: Plan view micrograph of dislocation source in $(Si_{9.3}Ge_{3.7})_{24}$ superlattice annealed 20 s at 450° C. g = 022 dark field, s>>0.

are numerous points of localized strain in the superlattice. These were also present in the as–grown material. One of these points of stress concentration has emitted a 60° $\frac{a}{2}\langle 110\rangle$ dislocation whose entire length is visible in the micrograph. The length of this dislocation is approximately 1.2 μm, which is 2–3 orders of magnitude greater than the length predicted for a 20 s anneal at 450°C by equation (2.2.24), -- the "semi–empirical" equation of Houghton (1990) for the dislocation velocity as a function of the effective stress. Another source is shown at a higher magnification in fig. 5.4. In both figures, a dislocation segment extends directly up from the source to the surface; this threading arm is pinned at the source. Another threading arm glides away from the source and leaves behind a 60° dislocation which relieves misfit in the epilayer.

Relaxation in the $(Si_{6.6}Ge_{2.0})_{48}$ superlattice took place at a higher temperature than the $(Si_{9.3}Ge_{3.7})_{24}$ superlattice. There were no dislocations visible in a plan view sample which had been annealed for 20 s at 450°C, although after annealing for 20 s at 500°C some dislocation sources become active. This may be seen in fig. 5.5, in which two of a number of potential sources have emitted 60° $\frac{a}{2}\langle 110\rangle$ dislocations. More of these sources are shown in fig. 5.6 as imaged in dark field using g = 022. There is a bend contour running across the micrograph; those sources lying in its path have $s \cong 0$ and exhibit the clear white/black asymmetry associated with a small misfitting coherent particle (Ashby and Brown 1963). The sense of this asymmetry indicates that these defects behave as localized points of expansion. A view of an activated source is shown in figs. 5.7 and 5.8, while that of an inactive source is shown in figs. 5.9 and 5.10. Some of the sources appear to be

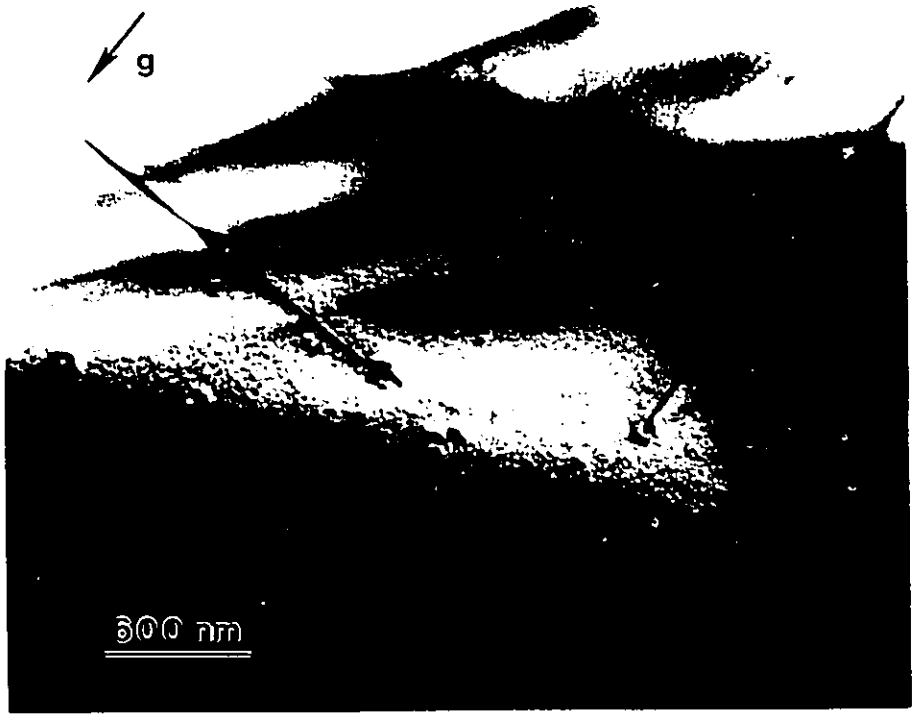

Figure 5.5: Dislocation sources in $(Si_{6.6}Ge_{2.0})_{48}$ superlattice annealed 20 s at 500° C. $\mathbf{g} = 022$.

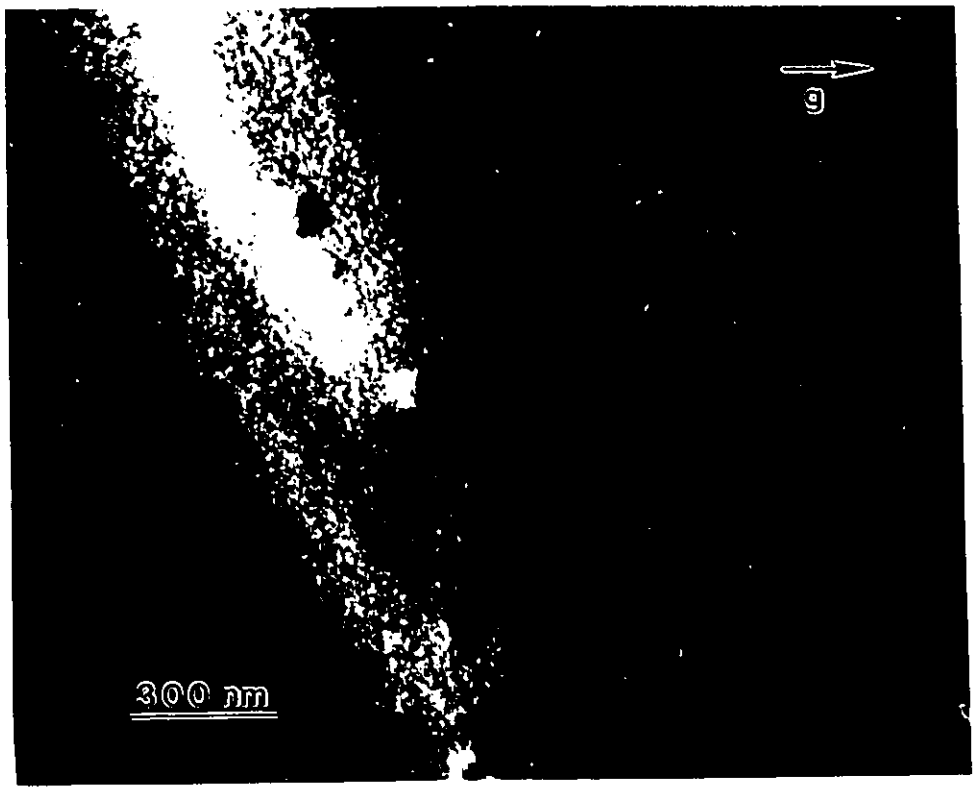

Figure 5.6: Dislocation sources in $(Si_{6.6}Ge_{2.0})_{48}$ superlattice annealed 20 s at 500° C. **g** = 022 dark field.

Figure 5.7: Plan view micrograph of activated dislocation source in $(Si_{6.6}Ge_{2.0})_{48}$ superlattice annealed 20 s at 500° C. g = 022 bright field.

Figure 5.8: Plan view micrograph of activated dislocation source in $(Si_{6.6}Ge_{2.0})_{48}$ superlattice annealed 20 s at 500° C. g = 022 dark field, s>>0.

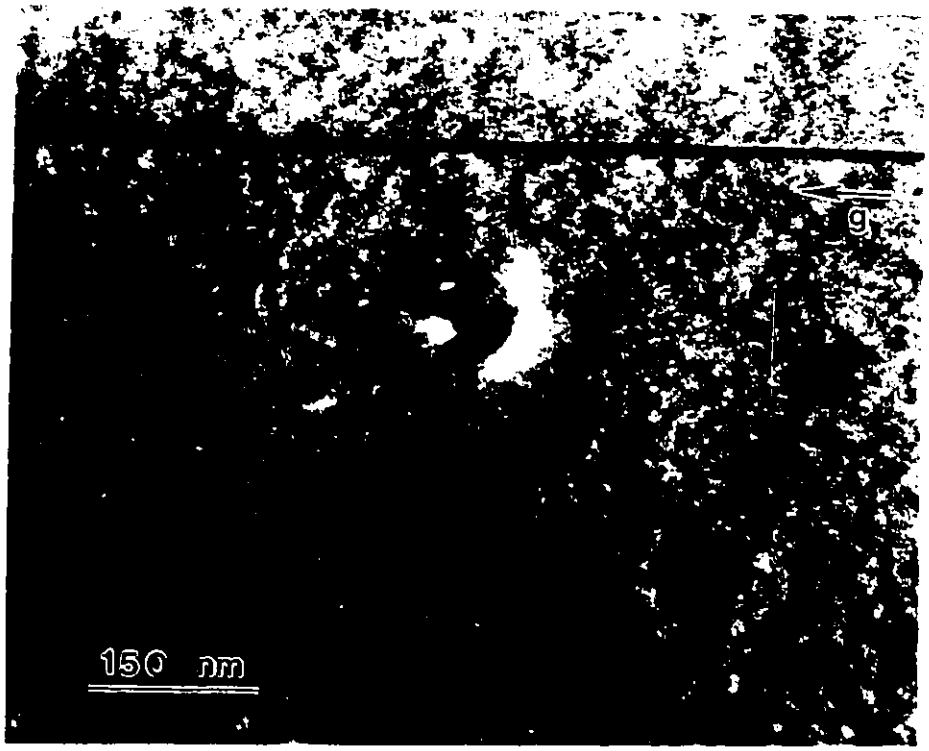

Figure 5.9: Plan view micrograph of an inactive dislocation source in $(Si_{6.6}Ge_{2.0})_{48}$ superlattice annealed 20 s at 500° C. A 60° dislocation relieving misfit is visible above the inactive source. g = 022 bright field.

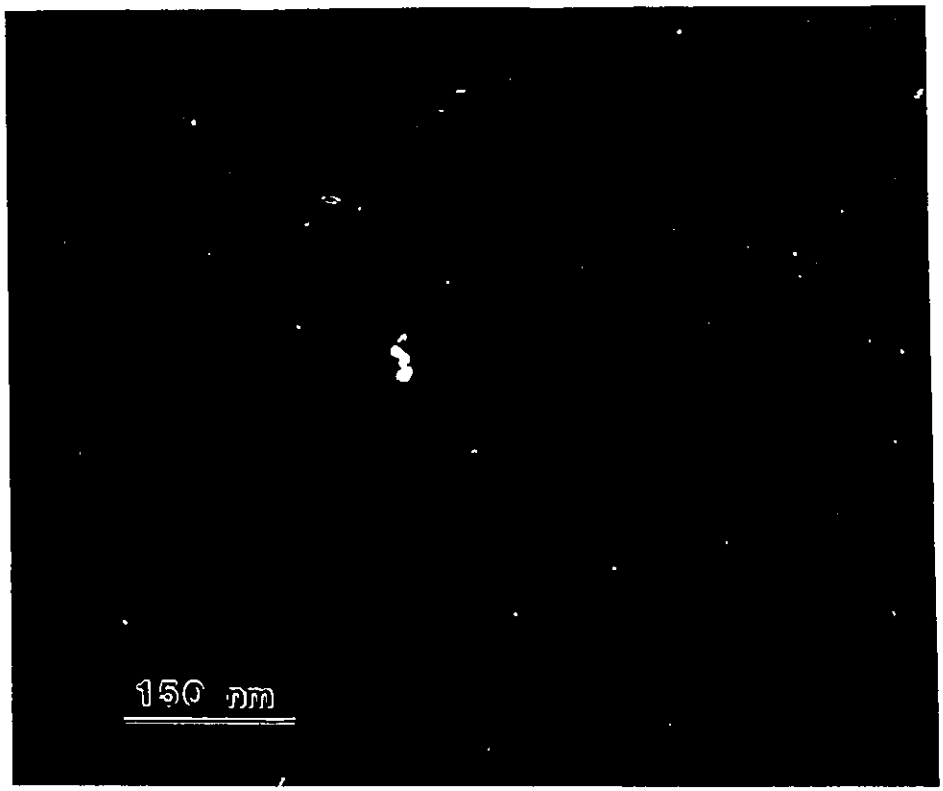

Figure 5.10: Plan view micrograph of an inactive dislocation source in $(Si_{6.6}Ge_{2.0})_{48}$ superlattice annealed 20 s at 500° C. A 60° dislocation relieving misfit is visible above the inactive source. g = 022 dark field, s>>0.

homogeneous objects. Others, usually larger than the homogeneous sources, have a highly strained region in their centre. Both types of defect were present in the as–grown material. In contrast to the behaviour of the two short period superlattices, neither of the homogeneous epilayers showed any sign of dislocation activity on annealing for 20 s at 500°C. Even 20 s at 600°C was insufficient to produce any visible dislocations in the TEM specimens. Higher temperatures are required in order to nucleate a large number of dislocations in these structures during a 20 s anneal.

In comparing the relaxation kinetics in various strained epitaxial layers, it is useful to consider the effective stress acting to drive dislocations through an epitaxial structure. This serves as a reference point in analyzing relaxation in different strained layers – if two structures have the same effective stress but different overall relaxation kinetics, then the variation is attributable to a difference in nucleation rate. Equation (2.2.10) may be used in calculating the effective stress, with $\varphi = 54.736°$, $\beta = 60°$, $\lambda = 45°$, $\nu = 0.218$, $\mu = 6.81\times10^{10}$ N/m^2, b = 3.84 Å, and $\alpha = 6.49$. The results for the two superlattices (where an average value of f has been used in calculating the effective stress) and for the two homogeneous epilayers used in this study are shown in table 5.1. It may be seen that the effective stresses in $(Si_{6.6}Ge_{2.0})_{48}$ and $(Si_{9.3}Ge_{3.7})_{24}$ superlattices are similar. However, as has been seen, the rate of relaxation observed experimentally is significantly higher in the $(Si_{9.3}Ge_{3.7})_{24}$ superlattice. This is due to differences in the nature of the sources in the two superlattices.

In both superlattices, the origin of the sources may be traced back to

Strained Layer Structure	Effective Stress (Nm^{-2})
$(Si_{6.6}Ge_{2.0})_{48}$	4.97×10^{8}
$(Si_{9.3}Ge_{3.7})_{24}$	6.16×10^{8}
$Si_{0.8}Ge_{0.2}\vert_{1000}$	5.40×10^{8}
$Si_{0.7}Ge_{0.3}\vert_{500}$	7.62×10^{8}

Table 5.1: Effective stresses in $(Si_mGe_n)_p$ short period superlattices and in homogeneous epilayers.

the development of non–planar layers during growth. This non–planar character is more pronounced in the $(Si_{9.3}Ge_{3.7})_{24}$ superlattice as it has germanium layers which are of greater thickness than those in the $(Si_{6.6}Ge_{2.0})_{48}$ superlattice. It is interesting that the $(Si_{6.6}Ge_{2.0})_{48}$ superlattice, grown with germanium layers 2.0 monolayers thick, eventually develops non–planar layers. Previous studies (Mo *et al.* 1990; Williams *et al.* 1991) have indicated that a single layer of germanium 2.0 monolayers thick deposited on germanium remains two–dimensional. Studies of Si–Ge superlattices grown on Si(100) carried out using X–ray reflection, Raman scattering spectroscopy, and EXAFS have suggested that two–dimensional growth is maintained as long as Ge layers are less than 5 monolayers thick, but that at the same time some interfacial mixing is present (Baribeau *et al.* 1991). The results obtained in this study indicate that the deviation from ideal two–dimensional growth is in fact greater than a minor degree of interfacial mixing. The sense of the white/black asymmetry associated with the dislocation sources in the 48–period superlattice is that corresponding to point sources of expansion. These are likely to be clusters of germanium atoms. Evidence of Ge clustering has been found in Si–Ge superlattices grown on Si(100) with a Ge layer thickness of 12 monolayers (Baribeau *et al.* 1991); the present results suggest that such clustering can occur even at Ge layer thicknesses of 2.0 monolayers.

It is worth considering the means by which a cluster of germanium atoms may act as a dislocation source. Such a cluster sitting near a free surface can punch out a dislocation half–loop which relieves the stress concentration near the cluster. As shown in fig. 5.11, there are two possible

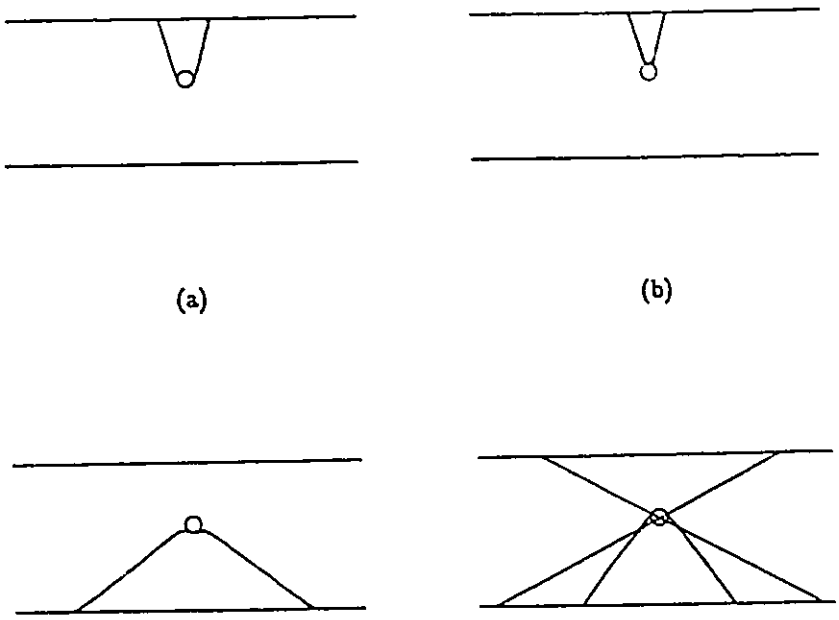

Figure 5.11: Dislocation configurations relieving stress concentration near a germanium cluster: (a) configuration relieving misfit both at the cluster and in the epilayer, (b) configuration relieving misfit only at the cluster.

ways in which the half–loop may be attached to a cluster. Only one of these configurations has the potential to expand and relieve misfit in the epilayer; this is also shown in fig. 5.11. The other configuration cannot simultaneously relieve misfit at the cluster and the substrate/epilayer interface.

When activated, the sources in both superlattices are single–ended. Only one of the threading arms of the half–loop glides freely; the other is pinned at the site of the localized stress concentration. It has been pointed out (Capano 1992) that of the two threading arms of a half–loop lying on {111} planes in a Si(100) growth system, one is 60° in character and the other is a screw segment. The arm which serves to better relieve the stresses at the superlattice inhomogeneity is the one that remains pinned. This is probably the segment having the edge component, for it can serve to relieve dilatational misfit.

Transmission electron microscopy indicates that the number of points of localized stress concentration per unit area giving rise under two–beam conditions with the deviation parameter $s \cong 0$ to strong contrast relative to the background intensity is of the same order of magnitude in both superlattices, that is, approximately 10^9 per square centimeter. If each of these points were equivalent dislocation sources, the relaxation behaviour of the two superlattices would be roughly identical. However, the points of stress concentration in fact represent potential dislocation sources having a spectrum of activation energies, with the number having activation energies low enough to generate dislocations at 450°C being significantly greater in the $(Si_{9.3}Ge_{3.7})_{24}$ superlattice than in the $(Si_{6.6}Ge_{2.0})_{48}$ superlattice. Thus

numerous activated sources were visible in TEM specimens of the 24–period superlattice which had been annealed for 20 s at 450°C, while none were visible in TEM specimens of the other superlattice given an identical annealing treatment.

In contrast to the behaviour of the two superlattices, the two homogeneous epilayers displayed no signs of dislocation activity even on annealing for 20 s at 600°C. The rate of relaxation in the superlattices was much greater than in the corresponding homogeneous epilayers, in spite of the slightly greater effective stress in the homogeneous epilayers. If the superlattices were grown at the temperature used for the homogeneous structures, they would have been fully relaxed in the as–grown state, provided that the same sort of interfacial perturbation developed at the higher temperature. The difference in the relaxation behaviour of the two types of strained layer structure may be inferred to be due to the vastly greater number of low activation energy sources in the superlattices. Since the homogeneous epilayers are made up of an essentially uniform deposit, there is no possibility of the formation of points of such a high stress concentration as in the case of the superlattices, and therefore dislocation sources which can be activated in the temperature range 450 – 500°C are absent.

CHAPTER 6

Relaxation Via Twinning in Si–Ge Compressively Strained Layers

It is well known that the relaxation of strain in Si–Ge layers deposited on a Si(100) substrate is typically achieved via the nucleation and propagation of 60° $\frac{a}{2}\langle 110\rangle$ misfit dislocations. The relief of compressive strain in the deposit by means of partial dislocations and associated stacking faults or by means of twinning has been considered to be unlikely because this would require the independent activity of 30° $\frac{a}{6}\langle 211\rangle$ dislocations (Marée *et al.* 1987). Indeed, although stacking faults and twins have been reported in Si–Ge layers deposited on Ge(100) (Wegscheider *et al.* 1989; Wegscheider *et al.* 1990; Wegscheider *et al.* 1991), there has to date been no report of these types of defects in the case of similar deposits on Si(100) except in relief of high stress concentrations in the vicinity of growth defects (LeGoues, Copel, and Tromp 1990). In the present work it is shown that under certain circumstances the relaxation of Si–Ge superlattices deposited on Si(100) may in fact proceed by means of twinning, accompanied by the growth of a diamond–hexagonal phase.

An 8–period strained layer superlattice consisting of 7.0 monolayers of Ge alternating with 17.5 monolayers of Si was grown in a Vacuum Generators V80 MBE system as described in the experimental procedure. A

cross–sectional micrograph of the as–grown material is shown in fig. 6.1. It may be seen that the growth surface has become non–planar even after the deposit of the first 7 monolayers of Ge. This is a result of the transition from Volmer–Weber to Stranski–Krastonov growth, which for Ge deposited on Si(100) has been found to take place after 3–4 monolayers (Asai, Ueba, and Tatsuyama 1985; Mo *et al.* 1990; Williams *et al.* 1991). The subsequent growth of the superlattice is accompanied by the development of gross perturbations at the surface, so that any resemblance to an ideal two–dimensional structure is very quickly lost, and a complicated stress field is set up within the epilayer. This accounts for the uneven contrast in fig. 6.2, which shows a plan view of the as–grown state imaged using $\mathbf{g} = 022$ and the deviation parameter $s \cong 0$.

Selected area diffraction patterns provide further information concerning the nature of the superlattice. A [100] diffraction pattern of the as–grown material is shown in fig. 6.3. In addition to the expected diamond cubic matrix reflections, there is a fairly intense set of rings which are due to the presence of amorphous material, as well as four faint spots lying on the {111} amorphous silicon ring. These result from the presence of two variants of the diamond hexagonal phase, one of which is imaged in fig. 6.4 using the $(0002)_{dh}$ reflection. This phase has $a = 3.86$ Å and $c = 6.31$ Å, giving $d_{0002} = 3.16$ Å (Pirouz *et al.* 1990a). The phase exists as randomly placed clusters of atoms approximately 50 Å in diameter. Tilting along the $02\bar{2}$ Kikuchi band to the [411] zone axis produced the diffraction pattern shown in fig. 6.5. Besides the matrix reflections, the rings, and the faint spots arising from the diamond hexagonal phase, there is a set of spots which

Figure 6.1: Cross–sectional micrograph of $(Si_{17.5}Ge_{7.0})_8$ superlattice in the as–grown state. g = 400 bright field, s>>0.

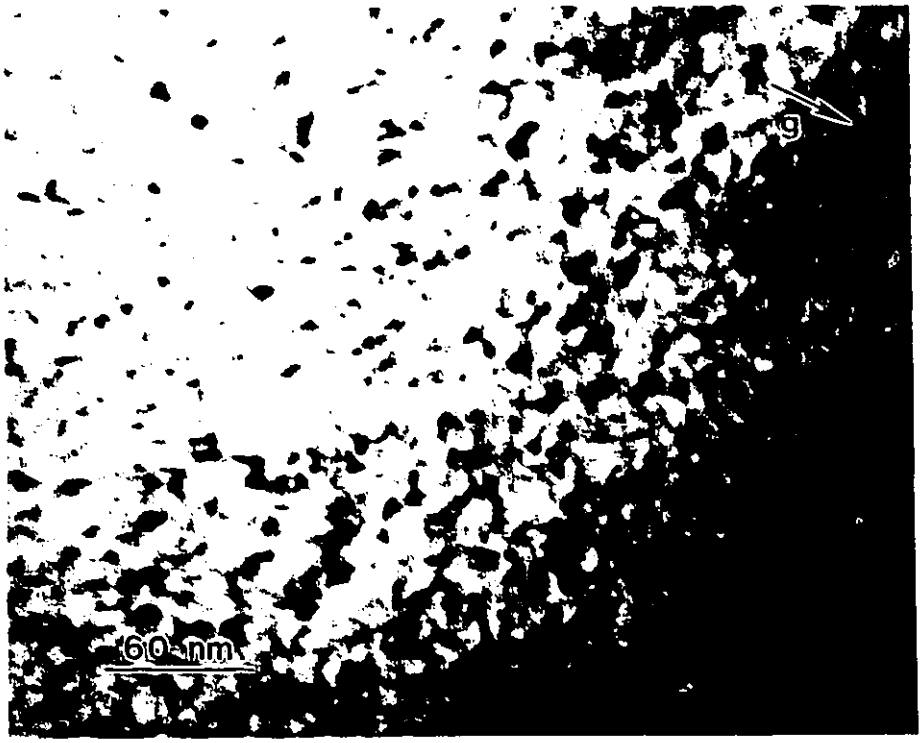

Figure 6.2: Plan view micrograph of $(Si_{17.5}Ge_{7.0})_8$ superlattice in the as–grown state. g = 022 bright field, s $\cong$ 0.

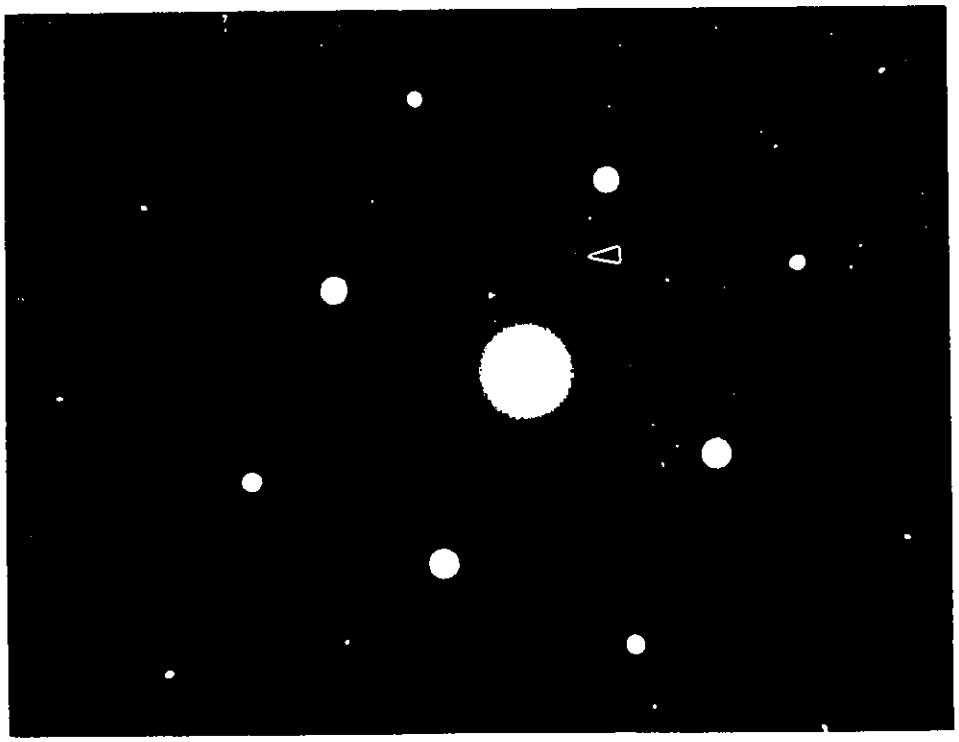

Figure 6.3: [100] diffraction pattern of as–grown $(Si_{17.5}Ge_{7.0})_8$ superlattice. A $(0002)_{dh}$ reflection is marked by an arrow.

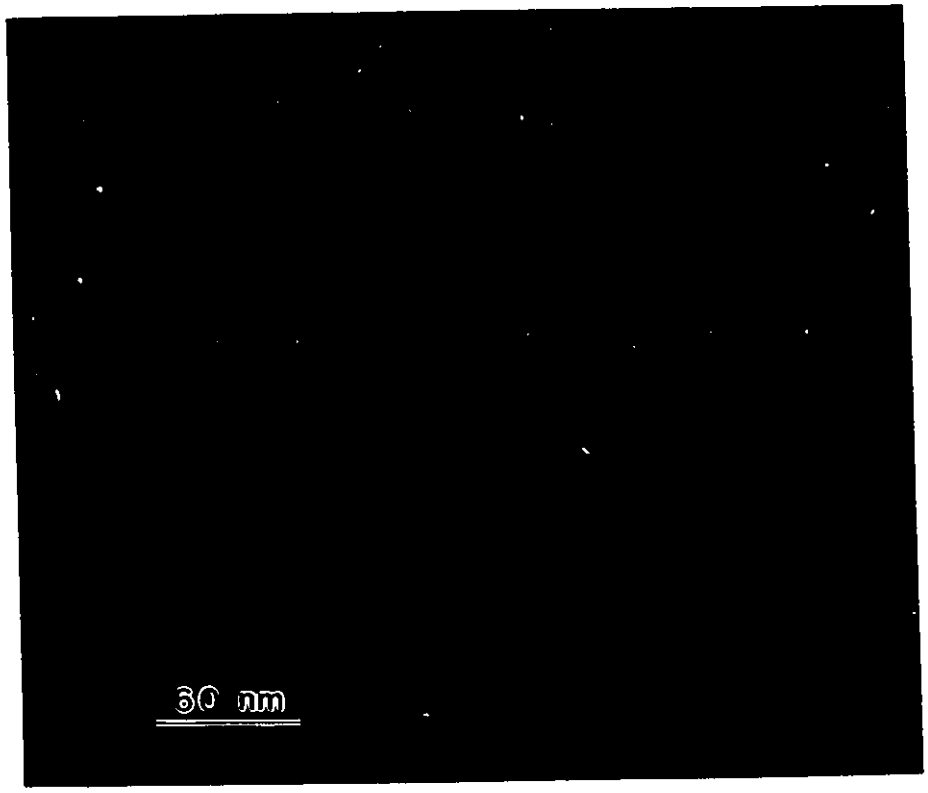

Figure 6.4: Diamond hexagonal phase in as–grown $(Si_{17.5}Ge_{7.0})_8$ superlattice. $\mathbf{g} = 0002_{dh}$.

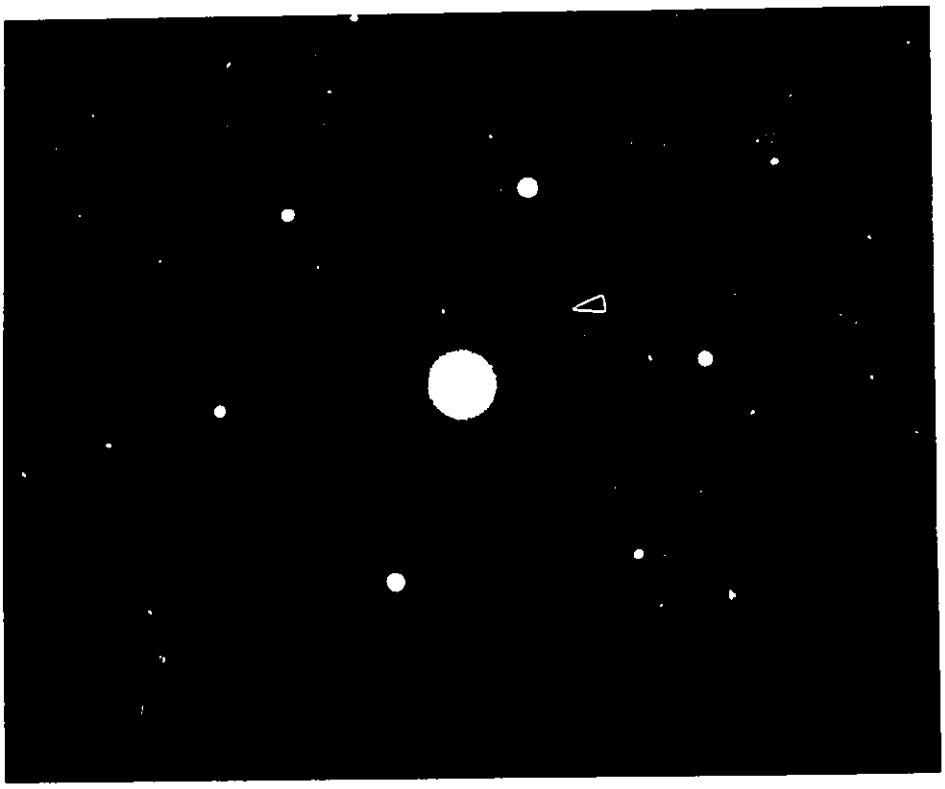

Figure 6.5: [411] diffraction pattern of as–grown $(Si_{17.5}Ge_{7.0})_8$ superlattice. A twin reflection is arrowed.

are due to the presence of one of four twin variants which exist in this sample. This is the variant lying on the (111) plane; applying the indicial transformation between matrix and twin (Hirsch *et al.* 1977) shows that the [411] matrix zone axis coincides with the [110] zone axis for (111) twins. Although the twins are very thin, having a rod–like diffracted intensity distribution in reciprocal space, they are oriented in such a way that this distribution intersects the Ewald sphere to give essentially a spot in the diffraction pattern. An image of the twins using one of the twin reflections from the [411] matrix zone axis is shown in fig. 6.6. As with the diamond hexagonal phase, the twins are very small, but they are more numerous than the diamond hexagonal clusters, and appear in a range of sizes.

Annealing at 700° C brought about a rapid increase in the size of both the twins and the diamond hexagonal phase. This may be seen for the twins in figs. 6.7–6.9 and for the diamond hexagonal phase in figs. 6.10 and 6.11. The micrographs in figs. 6.7–6.9 actually show the presence of two twin variants, for these images were taken by placing the objective aperture around two closely spaced $\frac{1}{3}\{115\}$ reflections on the 040 Kikuchi band approximately 11° away from the [100] zone axis. At this orientation these twin reciprocal lattice points are in contact with the Ewald sphere. Thus twins lying on orthogonal $\{111\}$ planes may be seen. Variations in the thickness of the twins gives rise to a range of intensity in their images. At 700° C, the greatest amount of growth occurred between 0 and 20 seconds. After this period, both the twins and the diamond hexagonal phase continued to grow, but at a slower rate. Cross–sectional TEM images of a specimen annealed for 2000 s at 700° C showing the presence of twins appear in fig. 6.12. The

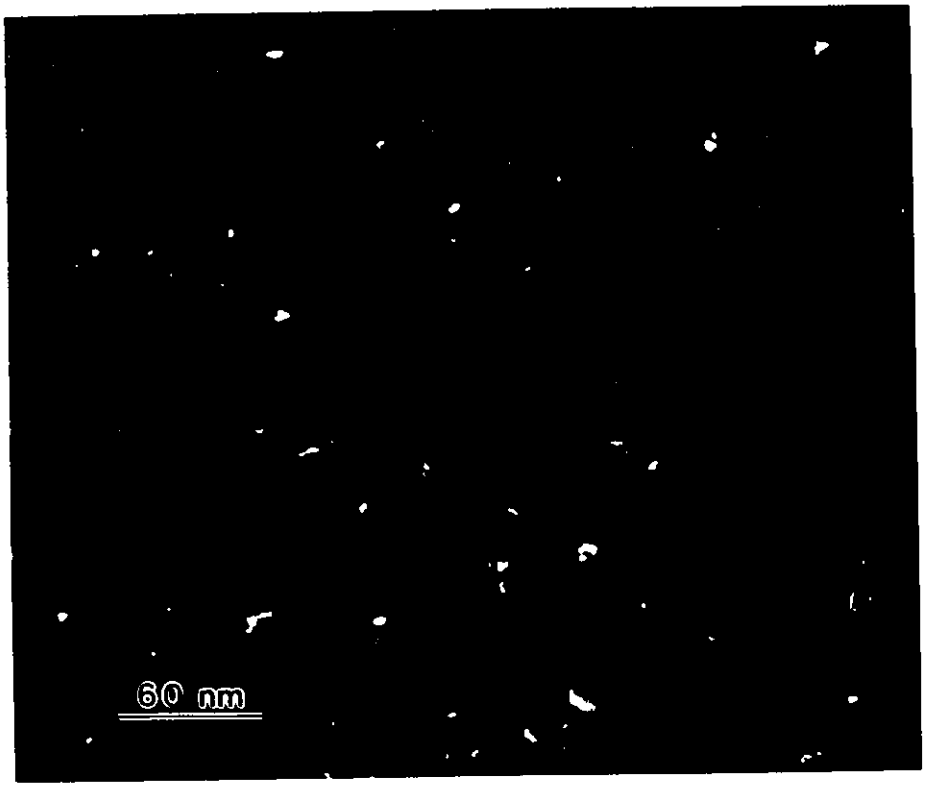

Figure 6.6: {111} twins in as–grown $(Si_{17.5}Ge_{7.0})_8$ superlattice.

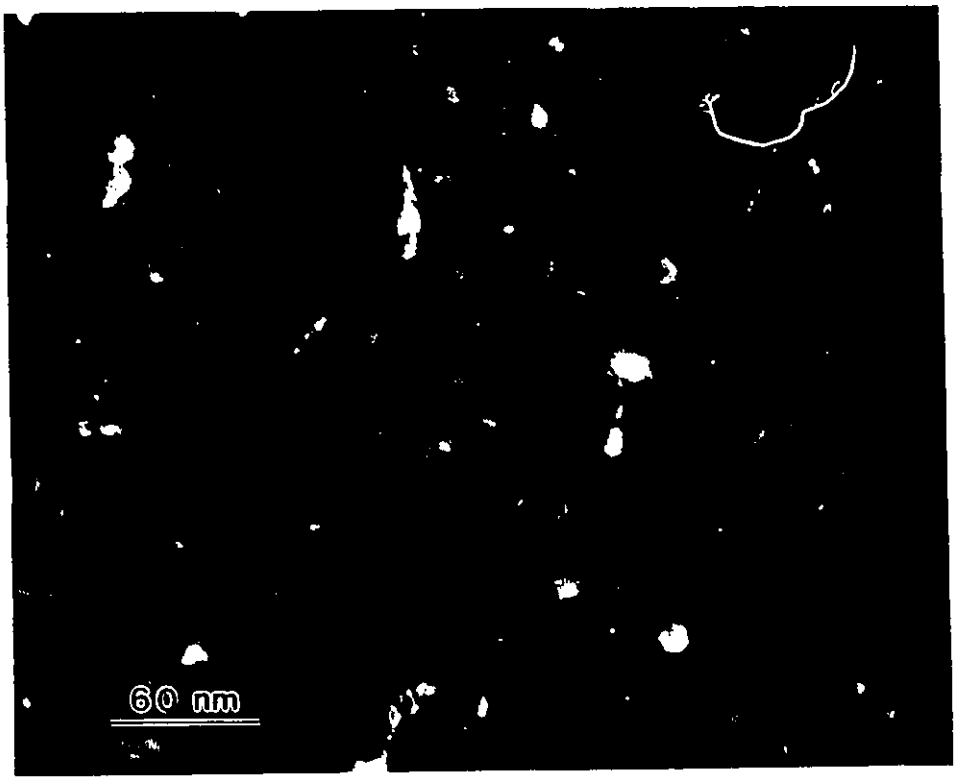

Figure 6.7: {111} twins in $(Si_{17.5}Ge_{7.0})_8$ superlattice annealed 20 s at 700° C.

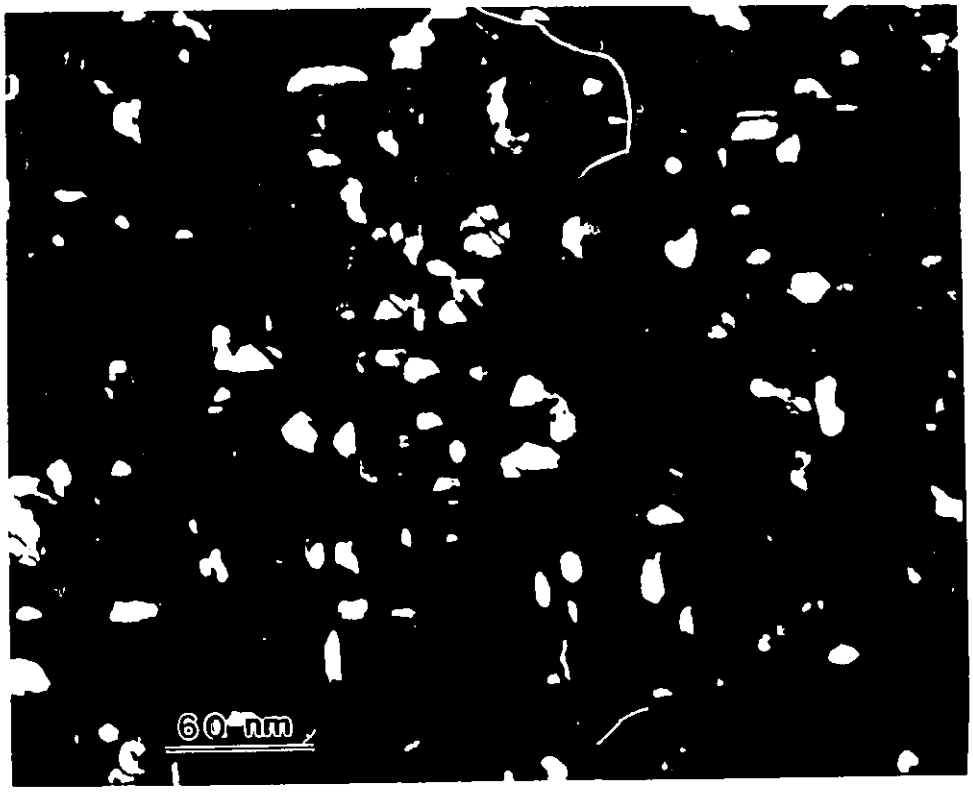

Figure 6.8: {111} twins in $(Si_{17.5}Ge_{7.0})_8$ superlattice annealed 2000 s at 700° C.

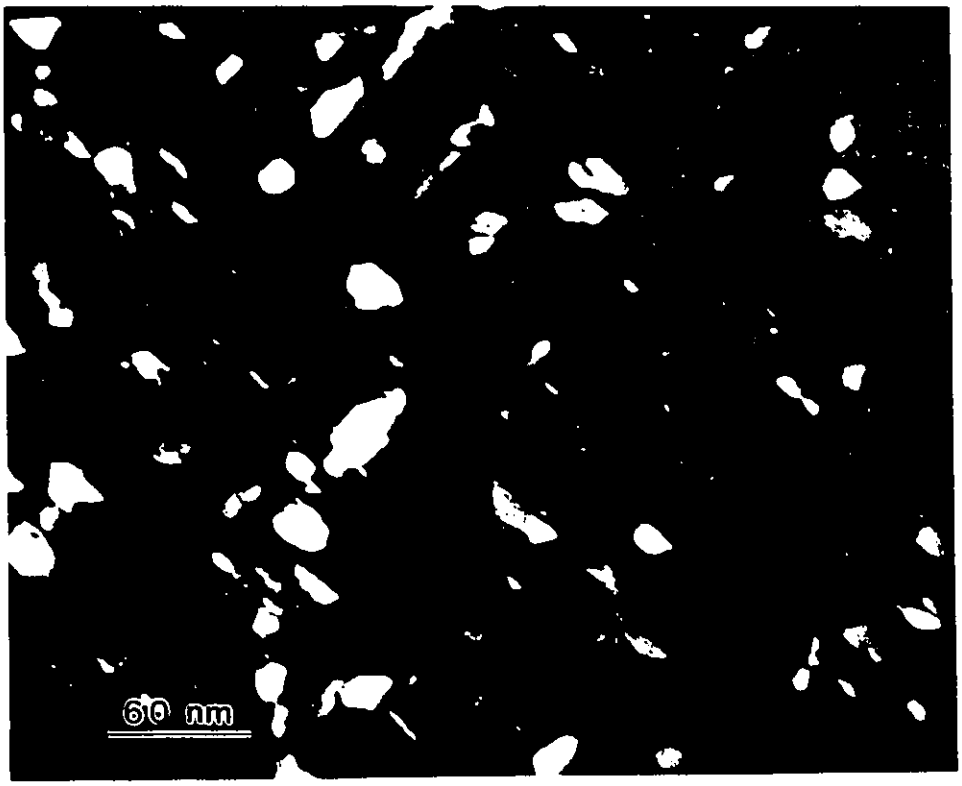

Figure 6.9: {111} twins in $(Si_{17.5}Ge_{7.0})_8$ superlattice annealed 300 s at 800° C.

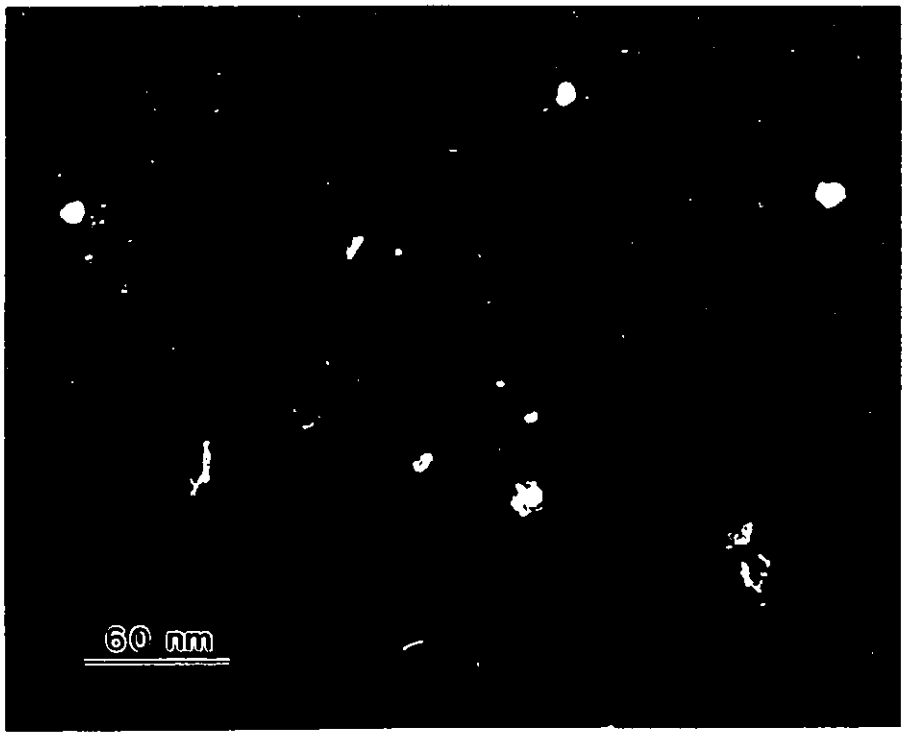

Figure 6.10: Diamond hexagonal phase in $(Si_{17.5}Ge_{7.0})_8$ superlattice annealed 200 s at 700° C. $\mathbf{g} = 0002_{dh}$.

Figure 6.11: Diamond hexagonal phase in $(Si_{17.5}Ge_{7.0})_8$ superlattice annealed 300 s at 800° C. $\mathbf{g} = 0002_{dh}$.

Figure 6.12: Cross-sectional micrograph of {111} twins in $(Si_{17.5}Ge_{7.0})_8$ superlattice annealed 2000 s at 700° C. g = 400 bright field, s>>0.

Figure 6.13: Plan view micrograph showing Moiré fringes from $(Si_{17.5}Ge_{7.0})_8$ superlattice annealed 20 s at 700° C. g = 022 bright field, $s \cong 0$.

formation of twins is accompanied by the relaxation of the epilayer, as may be seen by the Moiré fringes imaged using $g = 022$ and $s \cong 0$ in fig. 6.13, which is a plan view of material annealed for 20 s at 700°C. Since the strain in the epilayer is not homogeneous, the fringes take on a rippled appearance.

Diffraction patterns also reflect the microstructural evolution of the superlattice. These are shown in figs. 6.14–6.17. While the as–grown material produces only faint $(0002)_{dh}$ reflections, the $(0002)_{dh}$ reflections present in the [100] diffraction patterns in figs. 6.14 and 6.15 are quite pronounced. Twinning reflections streaked in ⟨110⟩ directions may also be observed in figs. 6.14 and 6.15. The reciprocal lattice points associated with the twin reflections do not actually lie in the zero order Laue zone; their appearance is due to the local buckling of the foil (Hirsch *et al.* 1977). Diamond hexagonal reflections are also present in figs. 6.16 and 6.17, which show [411] diffraction patterns of annealed material. The pattern of fig. 6.17 is quite intricate because of streaking and double diffraction effects.

The growth of a superlattice in which 7 monolayers of pure Ge is periodically deposited on Si leads quickly to the development of a non–planar growth front. This creates interpenetrating layers of Si and Ge in which local values of the stress can be very high. According to linear elasticity theory, a planar deposit of Ge on Si(100) gives rise to a biaxial compressive stress of 6.8 GPa, or approximately $\mu/10$, where μ is the shear modulus of silicon. If the deposit becomes non–planar then stress concentration effects can raise this to even greater levels. These large stresses are sufficient to nucleate and

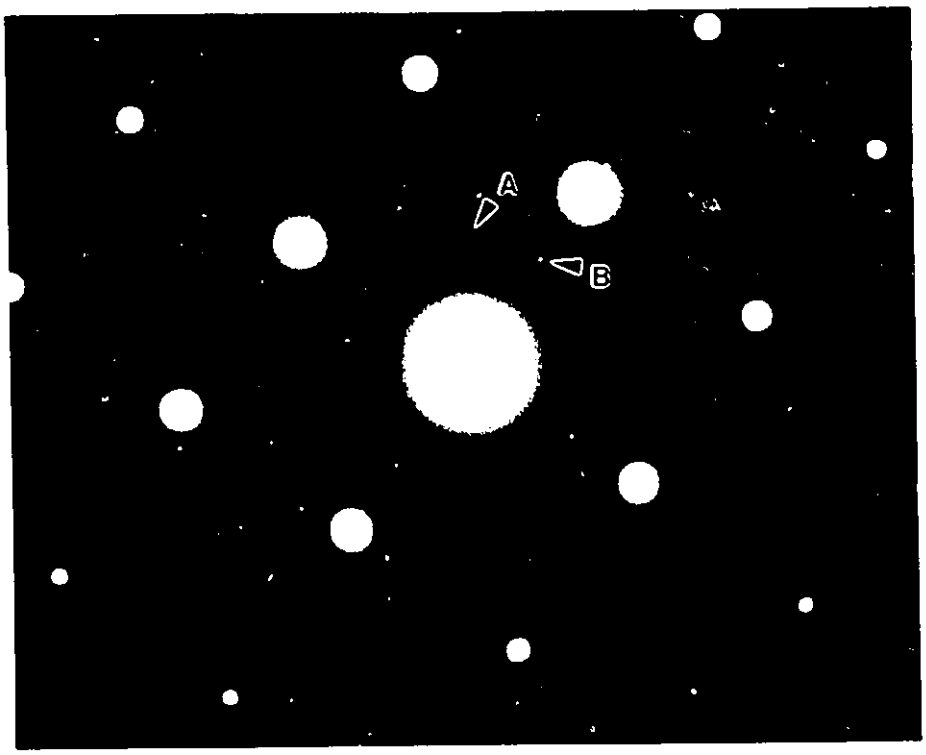

Figure 6.14: [100] diffraction pattern of $(Si_{17.5}Ge_{7.0})_8$ superlattice annealed 300 s at 800° C. A twin reflection is marked by arrow A and a $(0002)_{dh}$ reflection is marked by arrow B.

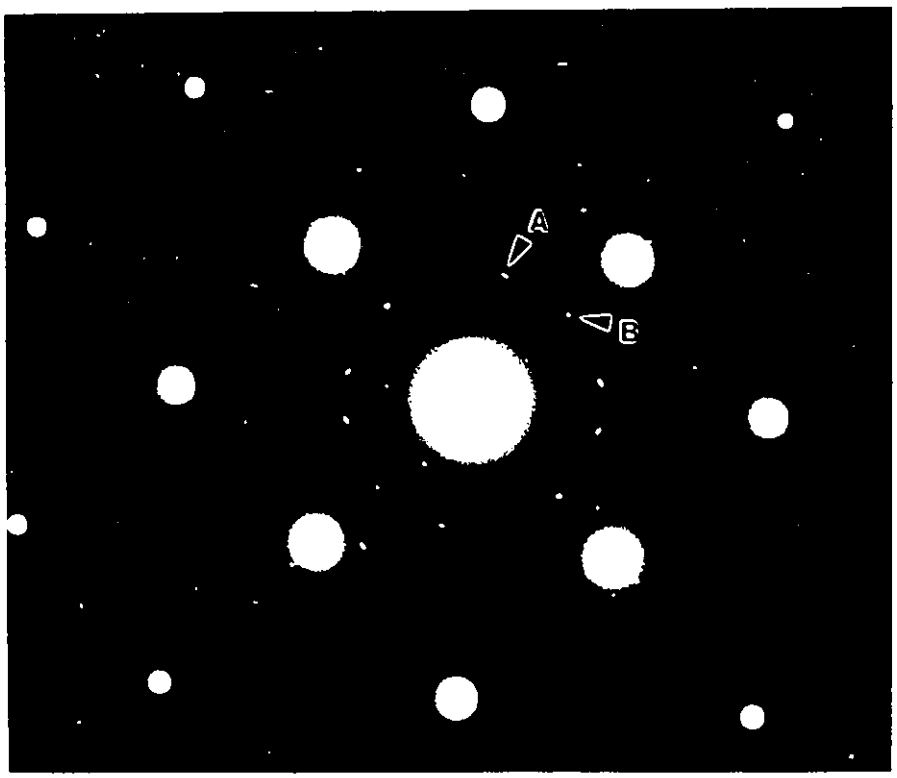

Figure 6.15: [100] diffraction pattern of $(Si_{17.5}Ge_{7.0})_8$ superlattice annealed 200 s at 700° C. A twin reflection is marked by arrow A and a $(0002)_{dh}$ reflection is marked by arrow B.

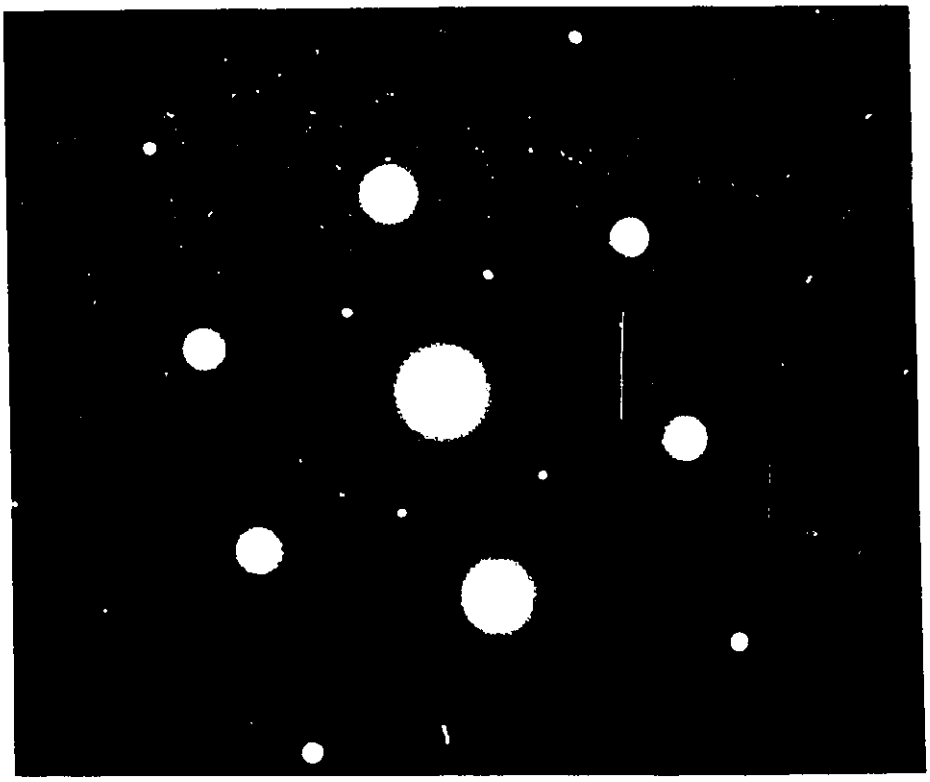

Figure 6.16: [411] diffraction pattern of $(Si_{17.5}Ge_{7.0})_8$ superlattice annealed 20 s at 700° C.

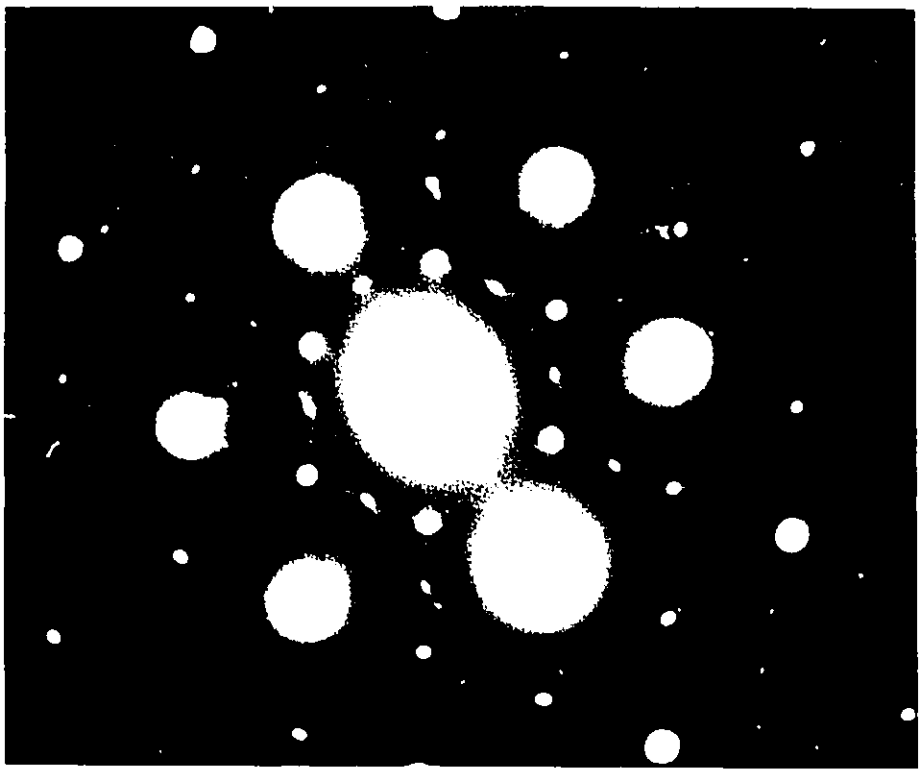

Figure 6.17: [411] diffraction pattern of $(Si_{17.5}Ge_{7.0})_8$ superlattice annealed at 2000 s at 700° C.

stablize very small twins on {111} planes. The twins act to relieve stress concentrations and lower the elastic energy of the as–grown material.

It is possible to generate twins through the motion of either 90° or 30° $\frac{a}{6}\langle 211\rangle$ partial dislocations on successive {111} planes. However, the motion of 90° partials can only relieve an epilayer which is under a net tensile strain, for their motion towards the substrate in an epilayer which is in compression gives rise to a high energy stacking sequence (Marée *et al.* 1987). Thus the twins in this material are bounded by 30° partials, although this is not as efficient a means of relieving the net compressive strain in the superlattice as 90° partials would be. Annealing the sample at 700°C results in interdiffusion accompanied by a growth of the twins which is initially rapid, and then slows. Once an appreciable amount of interdiffusion has taken place, the twins no longer act to relieve local stress concentrations, and serve only to relieve strain in the epilayer. The extent of this strain relief by the twins is sufficient to prevent the introduction of 60° $\frac{a}{2}\langle 110\rangle$ misfit dislocations to the substrate/epilayer interface. It is interesting that 4 twin variants were found to relieve misfit strain in this superlattice even though only 2 orthogonal variants are geometrically necessary in order to achieve the full relief of biaxial strain. This is analogous to the case of the relief of biaxial strain via 60° $\frac{a}{2}\langle 110\rangle$ dislocations, which may take place with dislocations having either a similar or an alternating orientation. Here the array of 30° partials bounding the twins has essentially an alternating orientation.

The existence of the diamond hexagonal phase in silicon having

$(011)_{dc} \parallel (0001)_{dh}$ is now well documented (Eremenko and Nikitenko 1972; Pirouz *et al.* 1990a; Dahmen *et al.* 1990; Pirouz *et al.* 1990b; Cerva 1991). A similar phase has also been found in germanium (Xiao and Pirouz 1992). Two mechanisms for the formation of this phase have been proposed. The first is the creation of the hexagonal phase at twin intersections. Such intersections result (Pirouz *et al.* 1990a; Xiao and Pirouz 1992) in a highly strained region which can undergo a martensitic transformation to the hexagonal phase in which the habit plane between the hexagonal and cubic phases is $\{511\}_{dc}$ and $(011)_{dc} \parallel (0001)_{dh}$, $[011]_{dc} \parallel [\bar{1}2\bar{1}0]_{dh}$. The second, also giving rise to the same habit plane and orientation relationship (Pirouz *et al.* 1990a; Xiao and Pirouz 1992), is the propagation of secondary twins into the diamond cubic matrix.

In the present case it seems probable that the diamond hexagonal phase observed is a result of the intersection of twin platelets. It is clear that the intersection of twins is a likely occurrence, while the generation of secondary twins is not so obvious a prospect. Rather than disappear on annealing, the diamond hexagonal phase increases in quantity. This can be explained as a byproduct of the relaxation of the superlattice via the formation of twins – as the extent of twinning increases, so does the number of intersecting twins and therefore the volume fraction of the hexagonal phase.

CHAPTER 7

The Pagoda Defect

The goal of crystal growth techniques such as MBE in the strained layer epitaxy of $Si_{1-x}Ge_x/Si$ films is to produce strained layers of the Ge–rich phase free of defects with abrupt, step–free interfaces separating the layers. In practice this has proven to be a difficult task. Here the role of the substrate in controlling the perfection of the growing layers in MBE grown Si–Ge structures and the introduction of a growth defect known as the "pagoda defect" (Perovic, Weatherly, Baribeau, and Houghton 1989) is examined.

Two $Si_{1-x}Ge_x/Si$ strained layer superlattices were grown by MBE and prepared for TEM examination as described in the experimental procedure. Pagoda defects in these samples were imaged under a number of diffracting conditions. Typical pagodas in the material having the lower Ge concentration in the alloy layer are shown in fig. 7.1. This image was recorded using $g = 400$ with the deviation parameter $s \cong 0$; a number of pagodas appear, each being a line of small lobes protruding from the $Si_{0.76}Ge_{0.24}/Si$ interfaces pointing back to the substrate. They all lie parallel to one another, running in a direction somewhat off [100]. The pagodas had an identical appearance when imaged using $g = \bar{4}00$, that is, the nature of the image was unchanged on reversing the sign of g. When the sample was tilted so that s took on a

Figure 7.1: Contrast from pagodas in a 20–period $Si_{0.76}Ge_{0.24}/Si$ superlattice, $\mathbf{g} = 400$, $s \cong 0$.

value appreciably different from zero, the pagodas very quickly disappeared – images of these defects in this sample were present only when $s \cong 0$. On imaging the pagodas using $g = 022$, again with $s \cong 0$, the image of the defects took the form of lines of arrows (chevrons) pointing toward the substrate as shown in fig. 7.2. Again, if the sign of g was reversed, the appearance of the defects remained unchanged.

The effective line direction of the pagoda defects was determined by a standard trace analysis technique. In this foil they were found to follow the [520] direction, which is about 22° from the [100] substrate normal.

Pagodas from material having an alloy layer composition of $Si_{0.65}Ge_{0.35}$ gave rise to contrast behaviour which differed from that of the $Si_{0.76}Ge_{0.24}$ material in several respects. Images of pagoda defects in $Si_{0.65}Ge_{0.35}$/Si were always present no matter what the diffracting conditions: two–beam with $s \cong 0$, two–beam with large values of s, or many–beam diffraction. On imaging with $g = 400$, pagodas took the appearance shown in figs. 7.3 and 7.4. In fig. 7.3, taken using $g = 400$ and $s \cong 0$, the defects again appear as bulges at $Si_{0.65}Ge_{0.35}$/Si interfaces which extend about 300 Å into the Si layers. Also visible are strain contrast effects, associated with the presence of the defects, in the Si layers themselves. In fig. 7.4 the diffracting condition was $g = 400$, with s taking on a relatively large positive value. Pagoda defects are again visible, but the associated strain contrast in the Si layers is no longer present. As before, if the sign of g was reversed for a given s, the image of the pagoda defects remained unchanged. The pagodas took on a completely different appearance on tilting to a beam direction

Figure 7.2: Chevron contrast from a 20–period $Si_{0.76}Ge_{0.24}/Si$ superlattice, $\mathbf{g} = 022$, $s \cong 0$.

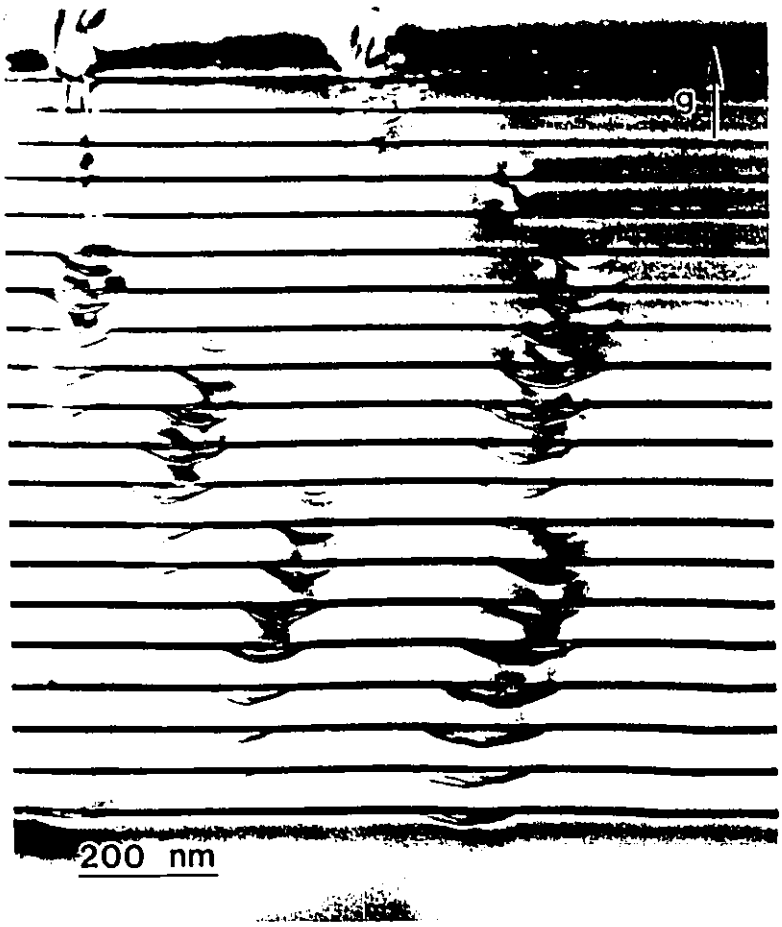

Figure 7.3: Contrast from pagodas in a 20–period $Si_{0.65}Ge_{0.35}$ superlattice. $g = 400$, $s \cong 0$ – both structure factor and strain field contrast are visible.

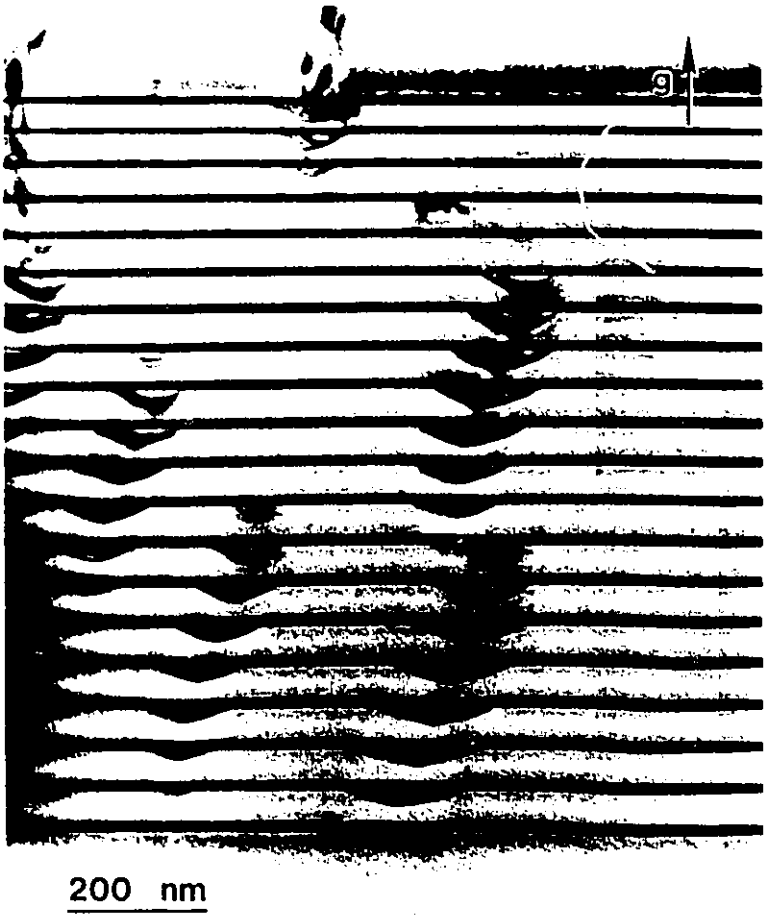

Figure 7.4: Contrast from pagodas in a 20–period $Si_{0.65}Ge_{0.35}$ superlattice. g = 400, s>>0 – only structure factor contrast contributes to the image.

approximately 10° away from the [0$\bar{1}$1] zone axis. Figure 7.5 shows pagoda images with the 133 Kikuchi band symmetrically disposed about the transmitted beam at a tilt angle of 10°. In effect this is a many–beam image. There is a marked change in the contrast features of a pagoda on moving from one end of an array to the other; this change is common to all of the pagodas in the micrograph. The sense of this contrast may be changed by tilting 10° away from the [0$\bar{1}$1] zone axis in the opposite direction while keeping the 133 Kikuchi band symmetrically disposed about the transmitted beam, as shown in fig. 7.6. Pagoda defects imaged using g = 400 (or g = $\bar{4}$00) in regions of the foil which were very thin took the form of a bend in the $Si_{0.65}Ge_{0.35}$/Si interface (see fig. 7.7).

Pagodas in this foil were found to follow the direction [13 5 2], about 22.5° from the [100] surface normal. In this particular sample the substrate was rotated during the growth of the buffer layer (including the B–doped delta layer), but there was no rotation during the alloy layer growth. Both the B–doped layer (visible as a faint rippled line midway between the substrate/buffer layer interface and the first alloy layer) and the alloy layers act as markers of the growth front morphology. The perturbations or "ripples" in the B–doped layer lie directly above particles at the substrate/buffer layer interface (fig. 7.8). Once growth of the alloy layers commenced (without substrate rotation) the defects grew in a direction determined by the Si source flux (see below).

The pagodas are visible through structure factor and strain field contrast effects, both of which depend on the Ge content in the alloy layers.

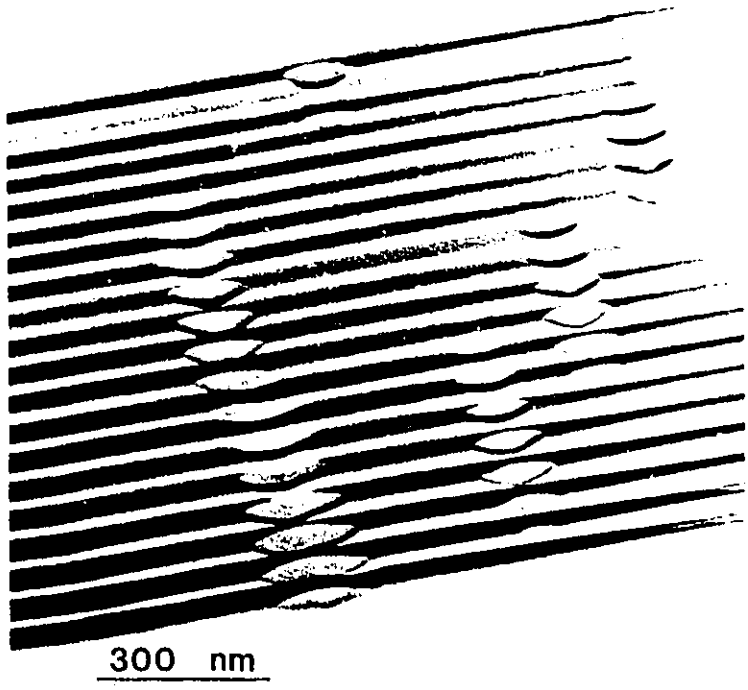

Figure 7.5: Contrast from pagodas in a 20–period $Si_{0.65}Ge_{0.35}$ superlattice with $\mathbf{g} = 133$ and $\overline{133}$ equally excited.

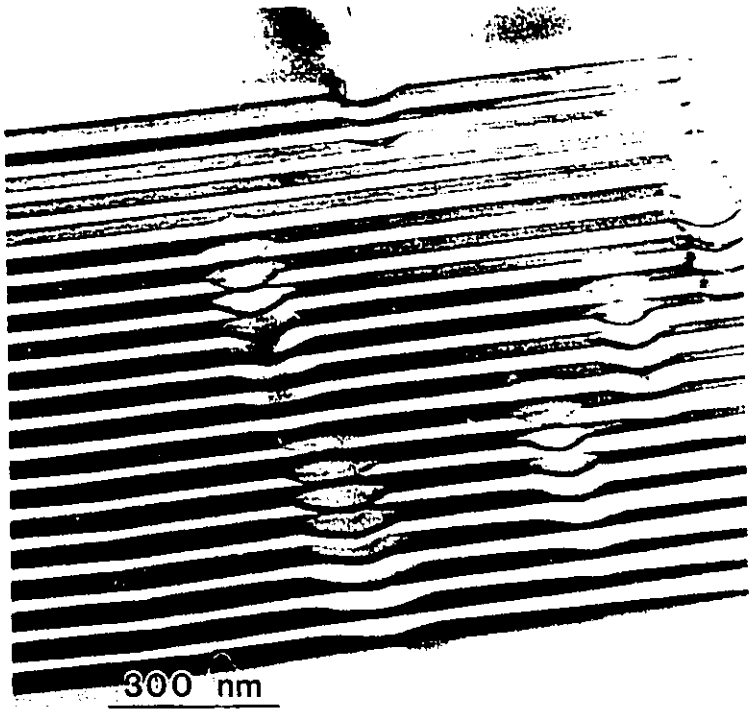

Figure 7.6: Contrast from pagodas in a 20–period $Si_{0.65}Ge_{0.35}$ superlattice with $\mathbf{g} = 133$ and $\overline{133}$ equally excited. Complement of figure 7.5.

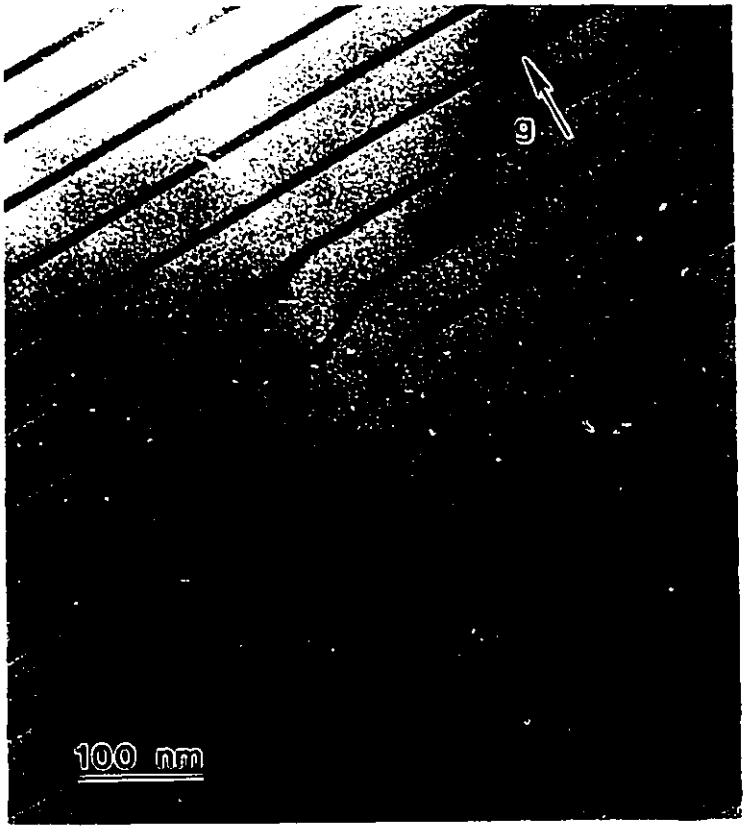

Figure 7.7: Thin region of a 20–period $Si_{0.65}Ge_{0.35}/Si$ superlattice; g = 400, showing bending of strained layers.

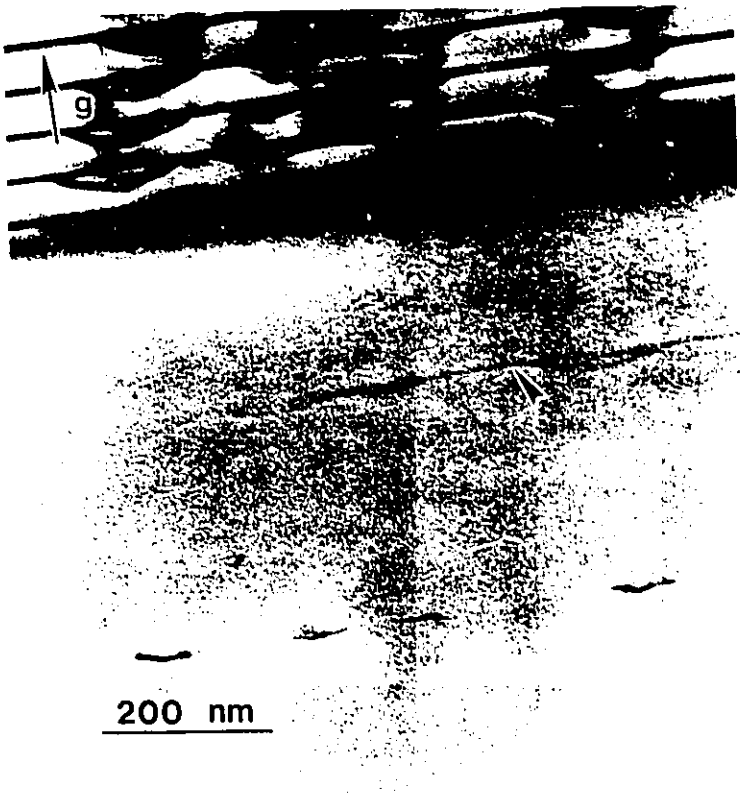

Figure 7.8: $Si_{0.65}Ge_{0.35}/Si$ superlattice; g = 400, showing the correlation between the position of thin SiC particles at the original substrate, the B–doped layer (arrowed), and the pagodas in the first few strained layers.

The factors which control the contrast in cross–sectional samples of perfect, planar strained layers in this system have been discussed in a recent paper by Perovic, Weatherly and Houghton (1991). Strain–field contrast arises from surface relaxation of the built–in strains of the bulk sample, while structure factor contrast is associated with the difference in scattering factors of Ge and Si and local displacements of Si atoms (in the strained layer).

In the cross–sectional samples the contrast from the pagodas arises both from structure factor and strain effects. Images of defects in the sample having the higher Ge concentration in the strained layers provide sufficient information to determine clearly the structural characteristics of pagodas. A consideration of the images presented in figs. 7.3–7.7 reveals their true morphology. They consist of a series of rounded conical perturbations in successive $Si_{1-x}Ge_x$/Si interlayers – these are the lobes which are seen in all the images. The perturbation involves a shift of both the Si and $Si_{1-x}Ge_x$ interfaces toward the substrate in which, as shown in fig. 7.8, the thickness of both layers remains essentially constant. The shift is greatest at the centre of a cone and tapers off until the surrounding flat regions of the layers are reached. When a cross–sectional foil is viewed with g = 400, one sees either a section taken through an individual cone (e.g. fig. 7.7, which comes from a very thin region) or a section that includes all or part of a cone together with the surrounding planar layer (in thicker foils, see e.g. fig. 7.3). When a cross–sectional foil of the material having the higher Ge content in the alloy layers is viewed under weakly diffracting conditions such as in figs. 7.5 and 7.6, the image is free of strain effects. The contrast observed is due to structure factor differences throughout the material, which in this case gives

rise to images of layers distorted in the form of solid conical bulges. The change in the contrast features on moving from one end of the pagoda to the other may be explained by the fact that the electron beam samples different columns of material depending on whether a lobe of a pagoda sits near the top or the bottom of the foil. The contrast inversion found on tilting along the 133 Kikuchi band in opposite directions from the $[0\bar{1}1]$ zone axis is due to an inversion in the nature of the column of material associated with a lobe of a pagoda traversed by the electron, as shown in fig. 7.9. In effect this is a manifestation of the reciprocity theorem for electron diffraction (Pogany and Turner 1968). Since in unrotated samples the direction followed by a pagoda defect has a significant component perpendicular to the plane of the foil, the sectioning of the thin TEM foil causes the apparent size of the defect to wax or wane, giving the characteristic pagoda–like image seen in several of the micrographs. In the cross–sectional samples having the lower Ge content, pagodas are visible only when $s \cong 0$ because the strain effect and variations in the structure factor are too small for pagodas to be visible under weakly diffracting conditions. Simple lobes are present in fig. 7.1 ($g = 400$), while chevron–type contrast is observed in fig. 7.2 ($g = 022$). The differences in the two images are due to the shorter extinction distance of the 022 reflection and the fact that (400) and (022) planes undergo different deformations in the presence of pagoda defects. The contrast in both images also shows the effect of surface relaxation – individual lobes of the pagoda which lie closer to the surface (but not so close that part of the lobe is missing from the foil) give rise to wider images than lobes which lie in the centre of the foil.

Pagodas always point back to the substrate, and in samples with a

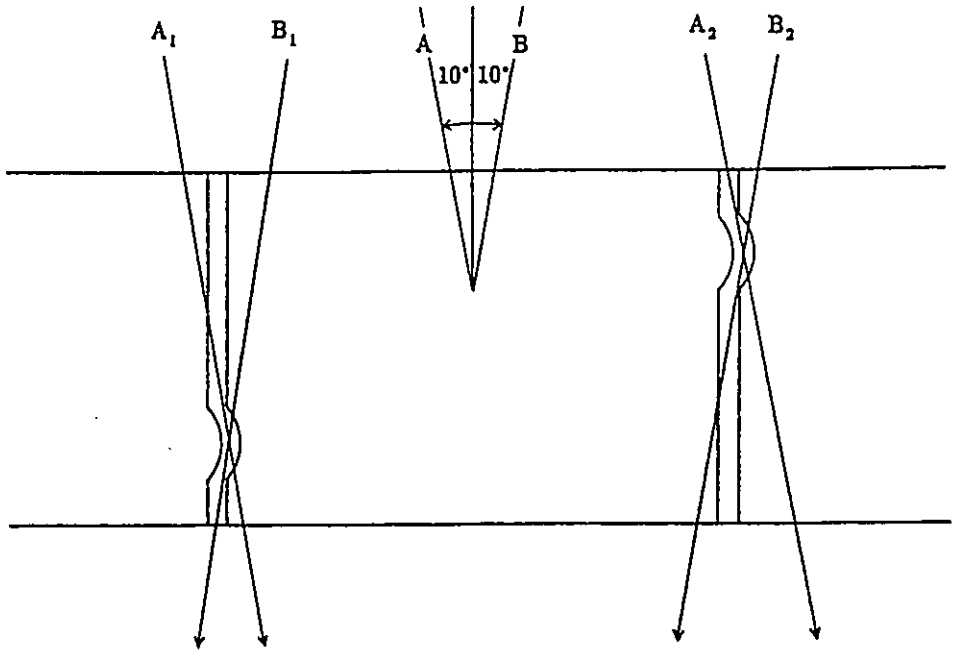

Figure 7.9: Diagram illustrating the origin of the contrast inversion found in a pagoda on tilting along the 133 Kikuchi band in opposite directions from the $[0\bar{1}1]$ zone axis. Directions A and B correspond to opposite senses of a 10° tilt.

very thin buffer layer between the substrate and the first strained layer, the origin of the cones can be correlated with particles left at the substrate after cleaning. These are probably β–SiC particles (Perovic *et al.* 1989). The formation of the cones at SiC particles is related to a low sticking coefficient for Si on SiC and a pinning effect of the particles on step or two–dimensional island growth. When silicon is first deposited on the substrate, it must be repelled by the SiC particles, so that the surface of a particle remains free of silicon (fig. 7.10(a)). As growth proceeds, silicon continues to be repelled by the surface of a particle, and a pit is formed in the region above a particle, as shown in fig. 7.10(b). Silicon finally covers the surface of the SiC precipitate (fig. 7.10(c)), leaving a pronounced conical depression there. A number of studies (Cullis and Booker 1971; Henderson, Marcus, and Polito 1971; Robbins *et al.* 1987; Pidduck *et al.* 1989) have shown that SiC particles can impede the flow of steps both during the growth and dissolution of Si(100) or Si(111) in vapour transport processes. At high temperatures (e.g. at 850°C using silane as the Si source), the formation of surface pits is observed to be a transient process, and after about 200 nm deposition at this temperature the pits are overgrown, leaving a smooth surface (Pidduck *et al.* 1989). In this study, conducted at much lower growth temperatures, this healing process is negligibly slow and the cone or pit structure can propagate with an essentially fixed morphology for several microns of deposition.

In a given area of a thin foil the pagodas always run in the same direction, although this varies from sample to sample or from different areas of the same substrate. In unrotated samples, the direction of the pagoda

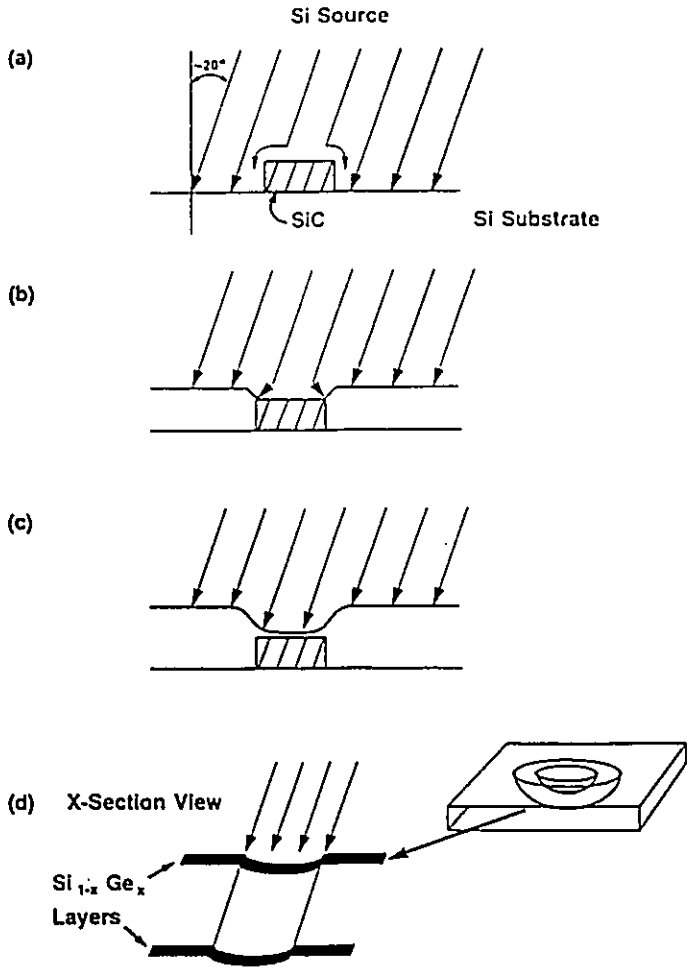

Figure 7.10: Diagram illustrating the stages involved in the formation of a depression at the location of a SiC particle in a growing surface.

appears to line up approximately with the angle made by the Si source with the substrate normal. It is assumed that as the Si source is always operating during growth, it is this source and not the Ge source which determines the overall direction of pit or cone growth. The Ge source acts principally as a marker which periodically decorates the surface morphology during growth. A very simple model can be used to describe the growth process. The overall (100) growth front is maintained by the familiar step or two–dimensional island growth process over the majority of the flat surface area, as documented in a number of recent scanning tunneling microscopy studies (Hamers, Tromp, and Demuth 1987; Hoeven *et al.* 1990; Legally *et al.* 1990). The pits or cones see the same flux as the rest of the surface, but grow in a direction which is determined by the line of sight to the Si source. The pit morphology and growth direction is governed by the condition that each point on the face of the pit grows at a rate determined by the flux at that point.

This is illustrated in fig. 7.10(d). If each element on the surface moves towards the source at a rate equal to the product of the volume of each particle and the flux impinging on each surface element, the surface as a whole moves upward uniformly and its shape is preserved (fig. 7.10). At first sight this is a surprising result, since scanning tunneling microscopy provides strong support for a step or two–dimensional island growth mode on Si(100) in this temperature range. If the shape of the pit was controlled by step migration, the morphology would change during growth (Frank 1958). However, we also know from other studies (Jorke, Herzog, and Kibbel 1989; Eaglesham, Gossman, and Cerullo 1990; Perovic *et al.* 1991) that at the relatively fast growth rates of MBE (approximately one monolayer per

second), the (100) step or island growth process is only marginally stable at these temperatures (400–500°C). Dropping the temperature significantly below 400°C leads to a morphological breakdown and the eventual formation of an amorphous film. The temperature range of 400–500°C clearly lies in a growth regime where (at least in MBE) a step or island growth process can coexist with one where there is no crystallographic influence imposed by the substrate. Thus flat regions of (100) oriented growth can be found adjacent to smoothly curved pits with no observed faceting. This is possible only if diffusion over the surface is very limited in extent.

CHAPTER 8

Summary and Conclusions

It has been found that the dislocation self energy and the dislocation–dislocation interaction energy as well as the dislocation–epilayer interaction energy in a strained epitaxial layer may all be obtained from the stress field of a single dislocation in a half–space. A knowledge of the slip system and the core energy of the dislocation allow for a precise determination of the core parameter α. Calculations indicate that the equilibrium dislocation spacing in two–dimensional orthogonal arrays in Si–Ge systems decreases very rapidly at thicknesses just greater than the critical thickness. Sixty degree dislocations lying on {111} planes on a Si(100) substrate approach the equilibrium spacing $\frac{b}{2|f|}$ (as the film thickness $h \rightarrow \infty$) most rapidly when they are arranged such that their screw components can form a twist boundary. This array of dislocations also has a lower energy (at its equilibrium spacing) than the corresponding array of alternating dislocations. The same method used to determine the energetics of dislocations in strained epitaxial layers can be used to find the energies of various low angle grain boundaries lying parallel to the free surface in a semi–infinite solid.

The growth of short period superlattices by MBE at 400°C is marked

by the development of non–planar layers even at Ge thicknesses as low as 2.0 monolayers. Non–planar growth leads to points of localized stress concentration which act as dislocation sources. These sources lead to considerable dislocation activity on annealing for short times in the temperature range 450–500°C. Homogeneous epilayers having effective stresses similar to those in short period superlattices relax much more slowly due to the absence of large numbers of low activation energy dislocation sources.

An 8–period superlattice consisting of 7.0 monolayers of Ge alternating with 17.5 monolayers of Si grown by MBE was found to relax through twinning on {111} planes, accompanied by the formation of a diamond hexagonal phase in which $(110)_{dc} \parallel (0001)_{dh}$. No 60° $\frac{a}{2}\langle 110\rangle$ dislocations were introduced to the strained layer structure during annealing. This behaviour was caused by the non–planar nature of the as–grown layers.

Perturbation of the (100) growth front during Si–Ge MBE growth leads to the formation of the pagoda defect at the strained layers. The defect is associated with the role of SiC particles at the original substrate surface, which disrupt the step or two–dimensional island growth process and introduce pits at the growth front. In unrotated samples these pits propagate toward the Si source, so the pagodas line up at a shallow angle (approximately 20°) to the [100] normal. The pagodas are visible in TEM images both by structure factor and strain contrast, but for most experimental situations structure factor contrast makes the major contribution to the image.

Appendix

A) Self Energy Integral – Burgers Vector Parallel to the Free Surface

$$U_{disl} = \frac{\mu b^2}{4\pi(1-\nu)}\left[\int_{r_0}^{\infty} \frac{1}{x_2}\, dx_2 + \int_{r_0}^{\infty} \frac{4h^2x_2 - x_2^3}{(x_2^2 + 4h^2)^2}\, dx_2\right.$$

$$\left. - \int_{r_0}^{\infty} \frac{48h^4x_2 - 4h^2x_2^3}{(x_2^2+4h^2)^3}\, dx_2\right] + U_{core}, \quad h>r_0,$$

where partial fraction decomposition gives

$$\int \frac{4h^2x_2 - x_2^3}{(x_2^2 + 4h^2)^2}\, dx_2 = \int \frac{8h^2x_2}{(x_2^2 + 4h^2)^2}\, dx_2 - \int \frac{x_2}{(x_2^2 + 4h^2)}\, dx_2$$

and

$$\int \frac{4h^2x_2^3 - 48h^4x_2}{(x_2^2 + 4h^2)^3}\, dx_2 = \int \frac{4h^2x_2}{(x_2^2 + 4h^2)^2}\, dx_2 - \int \frac{64h^4x_2}{(x_2^2 + 4h^2)^3}\, dx_2.$$

The integrals in decomposed form may be found from standard tables (Beyer 1978), giving

$$U_{disl} = \frac{\mu b^2}{4\pi(1-\nu)}\left[\tfrac{1}{2}\ln\left(\frac{r_0^2+4h^2}{r_0^2}\right) + \frac{6h^2}{(r_0^2+4h^2)} - \frac{16h^4}{(r_0^2+4h^2)^2}\right] + U_{core}, \quad h>r_0.$$

B) Dislocation – Epilayer Interaction Energy Integrals

The integrals $\int_{-\infty}^{\infty} \sigma_{11} dx_2$ and $\int_{-\infty}^{\infty} \sigma_{22} dx_2$ determine the dislocation–epilayer interaction energy for a dislocation lying parallel to the x_3 axis.

i) Burgers Vector Parallel to the Free Surface

a) $\int_{-\infty}^{\infty} \sigma_{11} dx_2$

Each of the three terms which make up σ_{11} is integrated separately. By partial fraction decomposition,

$$\int_{-\infty}^{\infty} \frac{(x_1-h)((x_1-h)^2 - x_2^2)}{((x_1-h)^2 + x_2^2)^2} dx_2 = \int_{-\infty}^{\infty} \frac{-(x_1-h)}{x_2^2 + (x_1-h)^2} dx_2$$

$$+ \int_{-\infty}^{\infty} \frac{2(x_1-h)^3}{(x_2^2 + (x_1-h)^2)^2} dx_2$$

with

$$\int \frac{1}{x_2^2 + (x_1-h)^2} dx_2 = \frac{1}{(x_1-h)} \tan^{-1}\left(\frac{x_2}{x_1-h}\right) + C$$

$$\int \frac{1}{(x_2^2 + (x_1-h)^2)^2}\, dx_2 = \frac{x_2}{2(x_1-h)^2(x_2^2 + (x_1-h)^2)}$$

$$+ \frac{1}{2(x_1-h)^3} \tan^{-1}\left(\frac{x_2}{x_1-h}\right) + C.$$

Therefore

$$\int_{-\infty}^{\infty} \frac{(x_1-h)((x_1-h)^2 - x_2^2)}{((x_1-h)^2 + x_2^2)^2}\, dx_2 = \left[\frac{(x_1-h)^3 x_2}{(x_1-h)^2(x_2^2 + (x_1-h)^2)}\right]_{-\infty}^{\infty} = 0,$$

because the $\tan^{-1}\left(\frac{x_2}{x_1-h}\right)$ terms cancel.

By partial fraction decomposition,

$$\int_{-\infty}^{\infty} \frac{(x_1+h)((x_1+h)^2 - x_2^2)}{((x_1+h)^2 + x_2^2)^3}\, dx_2 = \int_{-\infty}^{\infty} \frac{-(x_1+h)}{x_2^2 + (x_1+h)^2}\, dx_2$$

$$+ \int_{-\infty}^{\infty} \frac{2(x_1+h)^3}{(x_2^2 + (x_1+h)^2)^2}\, dx_2$$

with

$$\int \frac{1}{x_2^2 + (x_1+h)^2}\, dx_2 = \frac{1}{(x_1+h)} \tan^{-1}\left(\frac{x_2}{x_1+h}\right) + C$$

$$\int \frac{1}{(x_2^2 + (x_1+h)^2)^2}\, dx_2 = \frac{x_2}{2(x_1+h)^2(x_2^2 + (x_1+h)^2)}$$

$$+ \frac{1}{2(x_1+h)^3} \tan^{-1}\left(\frac{x_2}{x_1+h}\right) + C.$$

Therefore

$$\int_{-\infty}^{\infty} \frac{(x_1+h)((x_1+h)^2 - x_2^2)}{((x_1+h)^2 + x_2^2)^3}\, dx_2 = \left[\frac{(x_1+h)^3 x_2}{(x_1+h)^2(x_2^2 + (x_1+h)^2)}\right]_{-\infty}^{\infty} = 0,$$

because the $\tan^{-1}\left(\frac{x_2}{x_1+h}\right)$ terms cancel.

By partial fraction decomposition,

$$2h\int \frac{-x_2^4 - 6x_1(x_1+h)x_1^2 + (3x_1+h)(x_1+h)^3}{(x_2^2 + (x_1+h)^2)^3}\, dx_2$$

$$= 2h\int \frac{-1}{x_2^2 + (x_1+h)^2}\, dx_2 + 2h\int \frac{-4x_1^2 - 2hx_1 + 2h^2}{(x_2^2 + (x_1+h)^2)^2}\, dx_2$$

$$+2h\int \frac{8x_1^4 + 24hx_1^3 + 24h^2x_1^2 + 8h^3x_1}{(x_2^2 + (x_1+h)^2)^3}\, dx_2,$$

with

$$\int \frac{1}{x_2^2 + (x_1+h)^2}\, dx_2 = \frac{1}{(x_1+h)} \tan^{-1}\left(\frac{x_2}{x_1+h}\right) + C$$

$$\int \frac{1}{(x_2^2 + (x_1+h)^2)^2}\, dx_2 = \frac{x_2}{2(x_1+h)^2(x_2^2 + (x_1+h)^2)}$$

$$+ \frac{1}{2(x_1+h)^3} \tan^{-1}\left(\frac{x_2}{x_1+h}\right) + C$$

$$\int \frac{1}{(x_2^2 + (x_1+h)^2)^3}\, dx_2 = \frac{1}{4(x_1+h)^2(x_2^2 + (x_1+h)^2)^2}$$

$$+ \frac{3x_2}{8(x_1+h)^4(x_2^2 + (x_1+h)^2)} + \frac{3}{8(x_1+h)^5} \tan^{-1}\left(\frac{x_2}{x_1+h}\right) + C.$$

Therefore

$$2h\int_{-\infty}^{\infty} \frac{-x_2^4 - 6x_1(x_1+h)x_2^2 + (3x_1+h)(x_1+h)^3}{(x_2^2 + (x_1+h)^2)^3}\, dx_2$$

$$= 2h(-4x_1^2 - 2hx_1 + 2h^2)\left[\frac{hx_2}{(x_1+h)^2(x_2^2 + (x_1+h)^2)}\right]_{-\infty}^{\infty}$$

$$+ 2h(8x_1^4 + 24hx_1^3 + 24h^2x_1^2 + 8h^3x_1)$$

$$\cdot\left[\frac{h}{2(x_1+h)^2(x_2^2 + (x_1+h)^2)^2} + \frac{3hx_2}{4(x_1+h)^4(x_2^2 + (x_1+h)^2)}\right]_{-\infty}^{\infty}$$

(all $\tan^{-1}\left(\frac{x_2}{x_1+h}\right)$ terms cancel)

$$= 0.$$

Thus $\int_{-\infty}^{\infty} \sigma_{11} dx_2 = 0$, so that $\overline{\sigma_{11}} = 0$, as was stated in section 3.1.5.

b) $\int_{-\infty}^{\infty} \sigma_{22} dx_2$

Each of the terms making up σ_{22} is integrated separately. By partial fraction decomposition,

$$\int_{-\infty}^{\infty} \frac{(x_1-h)((x_1-h)^2 + 3x_2^2)}{((x_1-h)^2 + x_2^2)^2} dx_2 = \int_{-\infty}^{\infty} \frac{3(x_1-h)}{x_2^2 + (x_1-h)^2} dx_2$$

$$- \int_{-\infty}^{\infty} \frac{2(x_1-h)^3}{(x_2^2 + (x_1-h)^2)^2} dx_2$$

$$= \left[\frac{-2(x_1-h)^3 x_2}{2(x_1-h)^2(x_2^2 + (x_1-h)^2)}\right]_{-\infty}^{\infty} + \left[2\tan^{-1}\left(\frac{x_2}{x_1-h}\right)\right]_{-\infty}^{\infty}$$

$$= -2\pi,\ x_1<h;\ 2\pi,\ x_1>h.$$

By partial fraction decomposition,

$$\int_{-\infty}^{\infty} \frac{(x_1+h)((x_1+h)^2 + 3x_2^2)}{((x_1+h)^2 + x_2^2)} dx_2 = \int_{-\infty}^{\infty} \frac{3(x_1+h)}{x_2^2 + (x_1+h)^2} dx_2$$

$$- \int_{-\infty}^{\infty} \frac{2(x_1+h)^3}{(x_2^2 + (x_1+h)^2)^2} dx_2$$

$$= \left[\frac{-2(x_1+h)^3 x_2}{2(x_1+h)^2(x_2^2 + (x_1+h)^2)}\right]_{-\infty}^{\infty} + \left[2\tan^{-1}\left(\frac{x_2}{x_1+h}\right)\right]_{-\infty}^{\infty}$$

$$= 2\pi \text{ for all } x_1>0.$$

By partial fraction decomposition,

$$2h\int_{-\infty}^{\infty} \frac{x_2^4 - 6x_1(x_1+h)x_2^2 + (x_1-h)(x_1+h)^3}{(x_2^2 + (x_1+h)^2)^3}\, dx_2$$

$$= 2h\int \frac{1}{x_2^2 + (x_1+h)^2}\, dx_2 - 2h\int \frac{8x_1^2 + 10hx_1 + 2h^2}{(x_2^2 + (x_1+h)^2)^2}\, dx_2$$

$$+2h\int \frac{8x_1^4 + 24hx_1^3 + 24h^2x_1^2 + 8h^3x_1}{(x_2^2 + (x_1+h)^2)^3}\, dx_2.$$

Therefore

$$2h\int_{-\infty}^{\infty} \frac{x_2^4 - 6x_1(x_1+h)x_2^2 + (x_1-h)(x_1+h)^3}{(x_2^2 + (x_1+h)^2)^3}\, dx_2$$

$$= -2h(8x_1^2 + 10hx_1 + 2h^2)\left[\frac{hx_2}{(x_1+h)^2(x_2^2 + (x_1+h)^2)}\right]_{-\infty}^{\infty}$$

$$+ 2h(8x_1^4 + 24hx_1^3 + 24h^2x_1^2 + 8h^3x_1)$$

$$\cdot\left[\frac{h}{2(x_1+h)^2(x_2^2+(x_1+h)^2)^2}+\frac{3hx_2}{4(x_1+h)^4(x_2^2+(x_1+h)^2)}\right]_{-\infty}^{\infty}$$

(all $\tan^{-1}(\frac{x_2}{x_1+h})$ terms cancel)

$$= 0.$$

Thus $\int_{-\infty}^{\infty} \sigma_{22}dx_2 = -\frac{2\mu b}{(1-\nu)}$, $0<x_1<h$; 0, $x_1>h$.

ii) Burgers vector perpendicular to the free surface

a) $\int_{-\infty}^{\infty} \sigma_{11}dx_2$

Since $\sigma_{11}(-x_2) = -\sigma_{11}(x_2)$, $\int_{-\infty}^{\infty} \sigma_{11}dx_2 = 0.$

b) $\int_{-\infty}^{\infty} \sigma_{22}dx_2$

Again, since $\sigma_{22}(-x_2) = -\sigma_{22}(x_2)$, $\int_{-\infty}^{\infty} \sigma_{22}dx_2 = 0.$

C) Dislocation–Dislocation Interaction Energy Integrals

i) Burgers Vector Parallel to the Free Surface

$$U_d = \frac{\mu b^2}{2\pi(1-\nu)}\int_d^\infty \left[\frac{1}{x_2} + \frac{4h^2x_2 - x_2^3}{(x_2^2+4h^2)^2} - \frac{48h^4x_2 - 4h^2x_2^3}{(x_2^2+4h^2)^3} \right] dx_2, \quad d>2r_0$$

$$= \frac{\mu b^2}{2\pi(1-\nu)}\left[\left[\ln(x_2)\right]_d^\infty - \left[\tfrac{1}{2}\ln(x_2^2+4h^2)\right]_d^\infty + \left[\frac{-6h^2}{x_2^2+4h^2} + \frac{16h^4}{(x_2^2+4h^2)^2}\right]_d^\infty \right]$$

$$= \frac{\mu b^2}{4\pi(1-\nu)}\left[\ln\left(\frac{d^2+4h^2}{d^2}\right) + \frac{12h^2d^2+16h^4}{(d^2+4h^2)^2} \right], \quad d>2r_0.$$

ii) Burgers Vector Perpendicular to the Free Surface

$$U_d = \frac{\mu b^2}{2\pi(1-\nu)}\int_h^\infty \left[\frac{(x_1-h)^3 - (x_1-h)d^2}{((x_1-h)^2 + d^2)^2} - \frac{(x_1+h)^3 - (x_1+h)d^2}{((x_1+h)^2 + d^2)^2} \right.$$

$$\left. + \frac{2h((h-x_1)(x_1+h)^3 + (6x_1^2+6hx_1)d^2 - d^4}{((x_1+h)^2 + d^2)^3} \right] dx_1, \quad d>2r_0$$

or

$$U_d = \frac{\mu b^2}{2\pi(1-\nu)}\int_h^\infty \frac{x_1^3 - 3hx_1^2 + (3h^2-d^2)x_1 - h(h^2-d^2)}{((x_1-h)^2 + d^2)^2}\, dx_1$$

$$- \frac{\mu b^2}{2\pi(1-\nu)} \int_h^\infty \frac{x_1^3 - 3hx_1^2 + (3h^2-d^2)x_1 + h(h^2-d^2)}{((x_1+h)^2 + d^2)^2}\, dx_1$$

$$+ \frac{\mu b^2}{2\pi(1-\nu)} \int_h^\infty \frac{2h(-x_1^4 - 2hx_1^3 + 6d^2x_1^2 + (2h^3+6hd^2)x_1 + (h^4-d^4))}{((x_1+h)^2 + d^2)^3}\, dx_1,$$

where by partial fraction decomposition

$$\int \frac{x_1^3 - 3hx_1^2 + (3h^2-d^2)x_1 - h(h^2-d^2)}{(x_1^2 - 2hx_1 + (h^2+d^2))^2}\, dx_1$$

$$= \int \frac{x_1}{(x_1^2 - 2hx_1 + (h^2+d^2))}\, dx_1 - \int \frac{h}{(x_1^2 - 2hx_1 + (h^2+d^2))}\, dx_1$$

$$- \int \frac{2d^2x_1}{(x_1^2 - 2hx_1 + (h^2+d^2))^2}\, dx_1 + \int \frac{2hd^2}{(x_1^2 - 2hx_1 + (h^2+d^2))^2}\, dx_1,$$

and

$$\int \frac{x_1^3 + 3hx_1^2 + (3h^2-d^2)x_1 + h(h^2-d^2)}{(x_1^2 + 2hx_1 + (h^2+d^2))^2}\, dx_1$$

$$= \int \frac{x_1}{(x_1^2 + 2hx_1 + (h^2+d^2))}\, dx_1 + \int \frac{h}{(x_1^2 + 2hx_1 + (h^2+d^2))}\, dx_1$$

$$- \int \frac{2d^2x_1}{(x_1^2 + 2hx_1 + (h^2+d^2))^2}\, dx_1 + \int \frac{2hd^2}{(x_1^2 + 2hx_1 + (h^2+d^2))^2}\, dx_1,$$

and

$$\int \frac{2h(-x_1^4 - 2hx_1^3 + 6d^2x_1^2 + (2h^3+6hd^2) + (h^4-d^4))}{(x_1^2 + 2hx_1 + (h^2+d^2))^3}\, dx_1$$

$$= \int \frac{-2h}{(x_1^2 + 2hx_1 + (h^2+d^2))}\, dx_1$$

$$+ \int \frac{4h^2x_1}{(x_1^2 + 2hx_1 + (h^2+d^2))^2}\, dx_1 + \int \frac{4h^3 + 16hd^2}{(x_1^2 + 2hx_1 + (h^2+d^2))^2}\, dx_1$$

$$- \int \frac{16h^2d^2x_1}{(x_1^2 + 2hx_1 + (h^2+d^2))^3}\, dx_1 - \int \frac{16hd^2(h^2+d^2)}{(x_1^2 + 2hx_1 + (h^2+d^2))^3}\, dx_1.$$

Now

$$\int \frac{1}{(x_1^2 - 2hx_1 + (h^2+d^2))}\, dx_1 = \frac{1}{d}\tan^{-1}\left(\frac{x_1-h}{d}\right) + C$$

$$\int \frac{x_1}{(x_1^2 - 2hx_1 + (h^2+d^2))}\, dx_1 = \tfrac{1}{2}\ln(x_1^2 - 2hx_1 + (h^2+d^2))$$

$$+ \frac{h}{d}\tan^{-1}\left(\frac{x_1-h}{d}\right) + C$$

$$\int \frac{1}{(x_1^2 - 2hx_1 + (h^2+d^2))^2}\, dx_1 = \frac{x_1 - h}{2d^2(x_1^2 - 2hx_1 + (h^2+d^2))}$$

$$+ \frac{1}{2d^3}\tan^{-1}\left(\frac{x_1-h}{d}\right) + C$$

$$\int \frac{x_1}{(x_1^2 - 2hx_1 + (h^2+d^2))^2}\, dx_1 = \frac{-(-hx_1 + (h^2+d^2))}{2d^2(x_1^2 - 2hx_1 + (h^2+d^2))}$$

$$+ \frac{h}{2d^3}\tan^{-1}\left(\frac{x_1-h}{d}\right) + C$$

$$\int \frac{1}{(x_1^2 + 2hx_1 + (h^2+d^2))}\, dx_1 = \frac{1}{d}\tan^{-1}\left(\frac{x_1+h}{d}\right) + C$$

$$\int \frac{x_1}{(x_1^2 + 2hx_1 + (h^2+d^2))}\, dx_1 = \frac{1}{2}\ln(x_1^2 + 2hx_1 + (h^2+d^2))$$

$$- \frac{h}{d}\tan^{-1}\left(\frac{x_1+h}{d}\right) + C$$

$$\int \frac{1}{(x_1^2 + 2hx_1 + (h^2+d^2))^2}\, dx_1 = \frac{x_1 + h}{2d^2(x_1^2 + 2hx_1 + (h^2+d^2))}$$

$$+ \frac{1}{2d^3}\tan^{-1}\left(\frac{x_1+h}{d}\right) + C$$

$$\int \frac{x_1}{(x_1^2 + 2hx_1 + (h^2+d^2))^2}\, dx_1 = \frac{-(hx_1 + (h^2+d^2))}{2d^2(x_1^2 + 2hx_1 + (h^2+d^2))}$$

$$- \frac{h}{2d^3}\tan^{-1}\left(\frac{x_1+h}{d}\right) + C$$

$$\int \frac{1}{(x_1^2 + 2hx_1 + (h^2+d^2))^3}\, dx_1 = \frac{x_1+h}{2d^2}\left[\frac{1}{2(x_1^2 + 2hx_1 + (h^2+d^2))^2}\right.$$

$$\left. + \frac{3}{4d^2(x_1^2 + 2hx_1 + (h^2+d^2))}\right] + \frac{3}{8d^5}\tan^{-1}\left(\frac{x_1+h}{d}\right) + C$$

$$\int \frac{x_1}{(x_1^2 + 2hx_1 + (h^2+d^2))^3}\, dx_1 = \frac{-(hx_1 + (h^2+d^2))}{4d^2(x_1^2 + 2hx_1 + (h^2+d^2))^2}$$

$$-\frac{3h}{4d^2}\left[\frac{x_1+h}{2d^2(x_1^2+2hx_1+(h^2+d^2))}+\frac{1}{2d^3}\tan^{-1}\left(\frac{x_1+h}{d}\right)\right]+C.$$

Making use of these integrals gives, after some algebra,

$$U_d=\frac{\mu b^2}{4\pi(1-\nu)}\left[\ln\left(\frac{d^2+4h^2}{d^2}\right)-\frac{4h^2d^2+48h^4}{(d^2+4h^2)^2}\right],\quad d>2r_0.$$

D) Infinite Series and Products

Use is made of the following infinite series and products (Hansen 1975) in arriving at closed form expressions for dislocation–dislocation interaction energies:

$$\prod_{k=1}^{\infty}\left(1+\frac{z^2}{k^2}\right)=\frac{1}{\pi z}\sinh(\pi z)$$

$$\prod_{k=0}^{\infty}\left(1+\frac{z^2}{(2k+1)^2}\right)=\cosh\left(\frac{\pi z}{2}\right)$$

$$\sum_{k=0}^{\infty}\frac{1}{(k^2x^2+y^2)^2}=\tfrac{1}{2}y^{-4}+\frac{\pi}{4}x^{-2}y^{-3}\left(x\coth\left(\frac{\pi y}{x}\right)+\pi y\operatorname{csch}^2\left(\frac{\pi y}{x}\right)\right)$$

$$\sum_{k=0}^{\infty}\frac{1}{((2k+1)^2x^2+y^2)^2}=\frac{\pi}{16}x^{-2}y^{-3}\left(2x\tanh\left(\frac{\pi y}{2x}\right)-\pi y\operatorname{sech}^2\left(\frac{\pi y}{2x}\right)\right)$$

$$\sum_{k=0}^{\infty}\frac{k^2}{(k^2x^2+y^2)^2}=\frac{\pi}{4}x^{-4}y^{-1}\left(x\coth\left(\frac{\pi y}{x}\right)-\pi y\operatorname{csch}^2\left(\frac{\pi y}{x}\right)\right)$$

$$\sum_{k=0}^{\infty}\frac{(2k+1)^2}{((2k+1)^2x^2+y^2)^2}=\frac{\pi}{16}x^{-4}y^{-1}\left(2x\tanh\left(\frac{\pi y}{2x}\right)+\pi y\operatorname{sech}^2\left(\frac{\pi y}{2x}\right)\right).$$

References

Alexender, H., 1986, *Dislocations in Solids, Vol. 7*, edited by F.R.N. Nabarro (Elsevier).

Asai, M., Ueba, H., and Tatsuyama, C., 1985, *J. Appl. Phys.*, 58, 2577.

Ashby, M.F., and Brown, L.M., 1963, *Phil. Mag.*, 8, 1083.

Atkinson, A., and Jain, S.C., 1992, *J. Appl. Phys.*, 72, 2242.

Bacon, D.J., and Crocker, A.G., 1965, *Phil Mag.*, 12, 195.

Baribeau, J.–M., Lockwood, D.J., Jackman, T.E., Aebi, P., Tyliszczak, T., and Hitchcock, A.P., 1991, *Can. J. Phys.*, 69, 246.

Bauer, E., 1958, *Z. Krist.*, 110, 372.

Bauer, E., and van der Merwe, J.H., 1986, *Phys Rev.* B, **33**, 3657.

Beyer, W.H., 1978, *CRC Standard Mathematical Tables* 25^{th} *Edition* (CRC Press).

Capano, M.A., 1992, *Phys. Rev.* B, **45**, 11 768.

Cerva, H., 1991, *J. Mater. Res.*, 6, 2324.

Cowley, J.M., 1984, *Diffraction Physics* (North–Holland).

Cullis, A.G., and Booker, G.R., 1971, *J. Cryst. Growth*, **9**, 132.

Dahmen, U., Westmacott, K.H., Pirouz, P., and Chaim, R., 1990, *Acta Metall. Mater.*, 38, 323.

De Cooman, B.C., and Carter, C.B., 1989, *Acta Metall.*, **37**, 2765.

Dismukes, J.P., Ekstrom, L., and Paff, R.J., 1964, *J. Phys Chem.*, **68**, 3021.

Dodson, B.W., and Tsao, T.Y., 1987, *Appl. Phys. Lett.*, **51**, 1325.

Eaglesham, D.J., Kvam, E.P., Maher, D.M., Humphreys, C.J., and Bean, J.C., 1989, *Phil. Mag.* A, 59, 1059.

Eaglesham, D.J., Gossman, H.J., and Cerullo, M., 1990, *Phys. Rev. Lett.*, 65, 1227.

Eremenko, V.G., and Nikitenko, V.I., 1972, *Physica Status Solidi* (a), 14, 317.

Frank, F.C., 1958, *Growth and Perfection of Crystals*, edited by R.H. Doremus, B.W. Roberts, and D. Turnbull (Wiley).

Freund, L.B., 1990, *J. Mech. Phys. Solids*, 38, 657.

Hagen, W. and Strunk, H. J., 1978, *J. Appl. Phys.*, 17, 85.

Hamers, R.J., Tromp, R.M., and Demuth, J.E., 1987, *Phys. Rev.* B, 34, 5343.

Hansen, E., 1975, *A Table of Series and Products* (Prentice–Hall).

Head, A.K., 1953, *Proc. Phys. Soc.*, 66B, 793.

Henderson, R.C., Marcus, R.B., and Polito, W.J., 1971, *J. Appl. Phys.*, 42, 1208.

Hirsch, P., Howie, A., Nicholson, R., Pashley, D W., and Whelan, M.J., 1977, *Electron Microscopy of Thin Crystals* (Kreiger).

Hirth, J.P., and Lothe, J., 1982, *Theory of Dislocations* (McGraw–Hill).

Hoeven, A.J., Dijkkamp, D., van Loenen, E.J., Lenssinck, J.M., and Dieleman, J., 1990, *J. Vac. Sci. Technol.* A, 8 207.

Houghton, D.C., 1990, *Appl. Phys. Lett.*, 57, 2124.

Houghton, D.C., 1991, *J. Appl. Phys.*, 70, 2136.

Houghton, D.C., Perovic, D.D., Baribeau, J.–M., and Weatherly, G.C., 1990, *J. Appl. Phys.*, 67, 1850.

Howie, A., and Whelan, M.J., 1962, *Proc. Roy. Soc.*, A267, 206.

Howie, A., and Basinski, Z.S., 1968, *Phil. Mag.*, 17, 1039.

Hull, R., and Bean, J.C., 1989, *J. Vac. Sci. Technol.* A, 7, 2580.

Jain, S.C., Gosling, T.J., Willis, J.R., Totterdell, D.H.J., and Bullough, R., 1992, *Phil Mag* A, 65, 1151.

Jain, U., Jain, S.C., Atkinson, A., Nijs, J., Mertens, R.P., and Van Overstraeten, R. J. *Appl. Phys.*, 73, 1773.

Jorke, H., Herzog, H.J., and Kibbel, H., 1989, *Phys. Rev.* B, 40, 2005.

Kovacic, S.J., Simmons, J.G., Noel, J.–P., and Houghton, D.C., 1991, *IEEE Electron. Device Lett.*, 12, 439.

Kvam, E.P., Eaglesham, D.J., Humphreys. C.J., Maher, D.M., Bean, J.C., and Fraser, H.L., 1987, *Microscopy of Semiconducting Materials 1987*, Inst. Phys. Conf. Ser. No. 87, 165.

Lang. D.V., People, R. Bean, J.C., and Sergent, A.M., 1985, *Appl. Phys. Lett.*, **47**, 1333.

LeGoues, F.K., Copel, M., and Tromp, R.M., 1990, *Phys. Rev.* B, **42**, 11 690.

Matthews, J.W., 1966, *Phil. Mag.*, **13**, 1207.

Matthews, J.W., 1971, *Phil. Mag.*, **23**, 1405.

Matthews, J.W., 1975, *J. Vac. Sci. Technol.*, **12**, 126.

Matthews, J.W., and Blakeslee, A.E., 1974, *J. Cryst. Growth*, **27**, 118.

Matthews, J.W., Blakeslee, A.E., and Mader, S., 1976, *Thin Solid Films*, **33**, 253.

Mo, Y.–W., Swartzentruber, B.S., Kariotis, R., Webb, M.B., and Legally, M.G., 1989, *Phys. Rev. Lett.*, **63**, 2393.

Mo, Y–W., Savage, D.E., Swartzentruber, B.S., and Legally, M.G., 1990, *Phys. Rev. Lett.*, **65**, 1020.

Mo, Y.–W., and Legally, M.G., 1991, *J. Cryst. Growth*, **111**, 876.

Nabarro, F.R.N., 1967, *Theory of Crystal Dislocations* (Clarendon).

Nandedkar, A.S., and Narayan, J., 1987, *Phil. Mag.* A, **56**, 625.

Nandedkar, A.S., and Narayan, J., 1989, *Mater. Sci. and Eng.*, **A113**, 51.

Nandedkar, A.S., and Narayan, J., 1990, *Phil. Mag.* A, **61**, 873.

Nix, W.D., Noble, D.B., and Turlo, J.F., 1990, MRS Spring Meeting, San Franciso, Cal.

Patton, G.L., Comfort, J.H., Meyerson, B.S., Crabbe, E.F., Scilla, G.J., de Fresart, E., Stork, J.C., Sun, J.Y.C., Harame, D.L., and Burghartz, J.N., 1990, *IEEE Electron. Device Lett.*, **11**, 171.

Pearson, W.B., 1967, *A Handbook of Lattice Spacings and Structures of Metals and Alloys Vol. 2* (Pergamon Press).

Perovic, D.D., Weatherly, G.C., Baribeau, J.–M., and Houghton, D.C., 1989, *Thin Solid Films*, **183**, 141.

Perovic, D.D., Weatherly, G.C., and Houghton, D.C., 1990, *Mat. Res. Soc. Symp. Proc.*, **160**, 65.

Perovic, D.D., Weatherly, G.C., and Houghton, D.C., 1991, *Phil. Mag.* A, **64**, 1.

Pidduck, A.J., Robbins, D.J., Young, I.M., Cullis, A.G., and Martin, A.S.R., 1989, *Mater. Sci. and Eng.*, B4, 417.

Pirouz, P., Chaim, R., Dahmen, U., and Westmacott, K.H., 1990a, *Acta Metall. Mater.*, 38, 313.

Pirouz, P., Dahmen, U., Westmacott, K.H., and Chaim, R., 1990b, *Acta Matall. Mater.*, 38, 329.

Pogany, A.P., and Turner, P.S., 1968, *Acta Cryst.*, **A24**, 103.

Read, W.T., and Shockley, W., 1950, *Phys. Rev.*, **78**, 275.

Robbins, D.J., Pidduck, A.J., Cullis, A.G., Chew, N.G., Hardeman, R.W., Gasson, D.B., Pickering, C., Daw, A.C., Johnson, M., and Jones, R., 1987, *J. Cryst. Growth*, 81, 421.

Stranski, J.N., and Krastanov, L., 1938, *Ber. Akad. Wiss. Wien*, **146**, 797.

Tromp, R.M., Smeenk, R.G., and Saris, F.W., 1981, *Phys. Rev. Lett.*, **46**, 939.

Tuppen, C.G., Gibbings, C.J., Hockley, M., and Roberts, S.G., 1990, *Appl. Phys. Lett.*, 56, 54.

Volmer, M., and Weber, A., 1926, Z. *Phys. Chem.*, **119**, 277.

Wegscheider, W., Eberl, K., Cerva, H., and Oppolzer, H., 1989, *Appl. Phys. Lett.*, **55**, 448.

Wegscheider, W., Eberl, K., Abstreiter, G., Cerva, H., and Oppolzer, H., 1990, *Appl. Phys. Lett.*, **57**, 1496.

Wegscheider, W., Eberl, K., Abstreiter, G., Cerva, H., and Oppolzer, H., 1991, *Microscopy of Semiconducting Materials 1991*, Inst. Phys. Conf. Ser. No. **117** , 21.

Williams, A.A., Thornton, J.M.C., Macdonald, J.E., van Silfhout, R.G., van der Veen, J.F., Finney, M.S., Johnson, A.D., and Norris, C., 1991, *Phys. Rev.* B, **43**, 5001.

Willis, J.R., Jain, S.C., and Bullough, R., 1990, *Phil. Mag.* A, 62, 115.

Xiao, S.–Q., and Pirouz, P., 1992, *J. Mater. Res.*, 7, 1406.